

Dissertation for Doctor of Philosophy

Compressed Sensing and its Applications:
Computational Compound Eyes and Compressive
Spectrometers

Woong-Bi Lee

School of Electrical Engineering and Computer Science

Gwangju Institute of Science and Technology

2018

Compressed Sensing and its Applications:
Computational Compound Eyes and Compressive
Spectrometers

압축센싱 및 응용: 계산적 곤충눈 시스템 및
압축 분광 시스템

Compressed Sensing and its Applications:
Computational Compound Eyes and Compressive
Spectrometers

Advisor : Professor Heung-No Lee

by

Woong-Bi Lee


School of Electrical Engineering and Computer Science
Gwangju Institute of Science and Technology

A dissertation submitted to the faculty of the Gwangju Institute of Science and Technology in partial fulfillment of the requirements for the degree of Doctor of Philosophy in the School of Electrical Engineering and Computer Science

Gwangju, Republic of Korea

2018. 05. 16.

Approved by



Professor Heung-No Lee

Committee Chair

Compressed Sensing and its Applications:
Computational Compound Eyes and Compressive
Spectrometers

Woong-Bi Lee

Accepted in partial fulfillment of the requirements for the degree of Doctor
of Philosophy

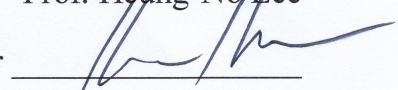
May 16 2018

Committee Chair



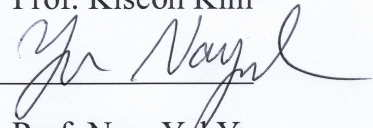
Prof. Heung-No Lee

Committee Member



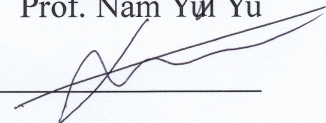
Prof. Kiseon Kim

Committee Member



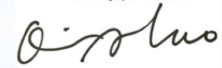
Prof. Nam Yul Yu

Committee Member



Prof. Young Min Song

Committee Member



Prof. Qing Zhao

Ph.D/EC
20112014

Woong-Bi Lee. Compressed sensing and its applications: computational compound eyes and compressive spectrometers. School of Electrical Engineering and Computer Science. 2018. 127p. Advisor: Prof. Heung-No Lee.

ABSTRACT

Compressed sensing (CS) has attracted a lot of interest and established as a new paradigm of signal acquisition that allows sampling and reconstructing signals below the Nyquist rate. CS theory states that if a signal is sparsely represented in a certain domain, the signal can be compressively sampled via linear projection, and reliably reconstructed from fewer measurements than required by the Nyquist rate. Therefore, CS enables simultaneous signal acquisition and compression that are efficient in terms of fast acquisition time, data reduction, and energy savings. In the early years, CS as its name indicates mainly focuses on a compression point of view, i.e., how small number of measurements can compressively acquire the signals and reconstruct them correctly. In a different viewpoint, however, when the system has inherently limited measurements, CS can be considered to improve system resolution by exploiting high dimensional signal reconstruction from the fixed low dimensional measurements.

This dissertation focuses on two applications of compressed sensing for resolution improvements, i.e., 1) *compound eye imaging systems* and 2) *filter-based miniature spectrometers*. In order to improve resolutions, conventional method is simply to increase the number of sampling (or imaging) units. However, in the compound eye imaging system, an ommatidium, a basic imaging unit is diffraction-limited and thus the size of ommatidium cannot be reduced unlimitedly. As a result, the number of ommatidia to be accommodated in a static volume of compound eye is limited. In the filter-based miniature spectrometers, the resolution is limited with respect to the number of optical

filters and their filtering performances. Miniaturizing the optical filters with maintaining the required filtering performance is very difficult and cost-inefficient. Instead of just increasing the number of ommatidia in the compound eye imaging systems and the number of filters in the miniature spectrometers, we propose entirely new designs of ommatidia and filters that aid in resolution improvements when combined with a digital signal processing (DSP) algorithm.

Traditional systems are designed to minimize the distortions or interferences because the interferences are considered unwanted noise. Thus, in the compound eye imaging system, the acceptance angles of ommatidia are designed small to prevent overlapping field of views of ommatidia. In spectrometers, the optical filters are designed to transmit the designated wavelengths and filter out the rest. In this work, we propose a *COMPUtational compound Eye* (COMPU-EYE) that has ommatidia with large acceptance angles and a *compressive spectrometer* equipped with filters having random transmittances. In both systems, each measurement is compressively spatially and spectrally encoded in the spatial domain in COMPU-EYE and in the spectral domain in the compressive spectrometer, respectively. We use DSP techniques for high-resolution signal reconstruction from the encoded low-dimensional measurements. We demonstrate that the resolution improvements are achieved in both systems. Furthermore, depth estimation in COMPU-EYE and incident angle estimation in compressive spectrometers are realized by exploiting uniqueness of measurement matrices and sparse representation-based classifications.

©2018

Woong-Bi Lee

ALL RIGHTS RESERVED

Ph.D/EC
20112014

이 용 비. 압축센싱과 그 응용: 계산적 곤충눈 시스템과 압축 분광 시스템. 전기전자컴퓨터공학부. 2018. 127p. 지도 교수: 이 흥 노.

국문요약

압축센싱은 전통적인 Nyquist sampling rate 보다 적은 수의 샘플로 압축하여 취득하여도, 다시 정교하게 복원 가능하다는 새로운 신호 취득 및 복원 방법이다. 압축센싱 이론에 의하면, 희소한 특징을 갖는 신호, 즉, 적은 수의 non-zero 값을 갖고, 대부분이 0의 값을 갖는 신호는 적은 수의 선형측정으로 원래의 신호를 정확히 복원할 수 있다. 압축센싱은 그 이름처럼 주로 신호를 얼마나 압축해서 취득을 하면 신호를 정확하게 복원할 수 있는지에 대해 연구가 되어왔다. 하지만, 시스템의 크기 성능, 또는 제작 비용 등의 이유로 제한된 선형측정의 수를 가지고 있는 시스템에서는, 정해진 선형측정의 수로부터 얼마나 많은 신호를 복원할 수 있는지 해상도 향상의 관점에서 접근할 수 있다. 본 연구에서는, 압축센싱의 신호 획득 및 고해상도 신호 복구 기술을 1) 곤충눈 시스템과 2) 소형 분광 시스템에 적용하였다. 전통적인 곤충눈 시스템에서는 각 홑눈 사이의 간섭을 최소화하기 위해서, 각각의 홑눈의 시야영역을 겹치지 않도록 수용각을 작게 설계한다. 전통적인 광학필터기반 분광 시스템에서도 각 필터 사이의 간섭을 최소화하기 위해서, 각 필터의 투과영역을 겹치지 않도록 필터를 설계한다. 반면에, 본 연구에서는, 각 홑눈 사이의 시야영역을 고의로 겹치도록 수용각을 크게 설계하고, 각 필터 사이의 투과영역을 고의로 겹치도록 필터를 설계한다. 이는 정보 취득 관점에서, 각 홑눈과 필터가 더 많은 정보를 취득한다고 볼 수 있다. 이러한 설계 방식으로 인해 왜곡된 선형측정 값들은

L_1 놈 기반의 디지털 신호 처리 방법을 통해 고해상도의 원래 신호로 높은 정확도로 복구된다. 또한, 제안하는 압축센싱 기반의 곤충눈 시스템에서 거리 추정 기법과 분광기 시스템에서 각도 추정 기법도 연구한다.

©2018

이 응 비

ALL RIGHTS RESERVED

CONTENTS

Abstract	i
Abstract(in Korean).....	iii
Contents	v
List of Tables	viii
List of Figures.....	ix
Abbreviations	xii
1 Introduction	1
1.1 Outline of the dissertation	2
2 Resolution improvements in compressed sensing.....	4
2.1 Compressed sensing	4
2.1.1 Sparsity	5
2.1.2 Incoherence	7
2.2 Compressed sensing for resolution improvement	8
2.3 Research motivation.....	8
3 COMPU-EYE: Computational compound eyes	13
3.1 Compound Eyes	14
3.1.1 Resolution limit in compound eyes.....	16
3.1.2 Depth estimation in compound eyes	19
3.1.3 Contributions of this chapter.....	22
3.2 System model of compound eye imaging	23
3.3 COMPU-EYE for image acquisition and reconstruction with high resolution	28
3.3.1 Overview and comparison of compound eyes	28
3.3.2 Effects of large acceptance angles and resolution improvements	32

3.4	Depth-estimation-enabled compound eyes.....	37
3.4.1	Depth estimation model	37
3.4.2	Depth estimation method	43
3.5	Simulation results.....	48
3.5.1	Simulation setups	48
3.5.2	Simulation results on resolution improvements	49
3.5.3	Simulation results on depth estimation	55
3.6	Summary	63
4	Compressive spectrometers	67
4.1	Introduction.....	68
4.1.1	Resolution limits of the filter-based miniature spectrometers.....	69
4.1.2	Incident angle mismatch	72
4.1.3	Related works.....	73
4.1.4	Contributions of this chapter.....	74
4.2	System model of filter-based spectrometers.....	75
4.3	Compressive spectrometers.....	79
4.3.1	Nonnegative l_1 norm minimization (NNLM) algorithm	79
4.3.2	Design of TFs of filter-array	83
4.3.3	Implementation of thin-film filters.....	91
4.4	Incident angle estimation of filter-based spectrometers	96
4.4.1	System model for incident angle estimation	96
4.4.2	Incident angle estimation method	98
4.5	Results and discussions	100
4.5.1	Measure transmittance functions.....	100
4.5.2	Results of resolution improvements.....	102
4.5.3	Results of incident angle estimation	104
4.6	Summary	107
5	Conclusions	109
	Bibliography	111

Acknowledgement	119
Curriculum Vitae	122

LIST OF TABLES

Table 1 SRC-based depth estimation algorithm	45
Table 2. Iterative depth estimation algorithm.....	48
Table 3. Nonnegative l_1 norm minimization (NNLM) algorithm.....	83
Table 4. Transmittance of multi-layer thin film	89
Table 5. Thicknesses of dielectric filters	93
Table 6 SRC-based incident angle estimation algorithm.....	99

LIST OF FIGURES

Figure 3.1 Artificial compound eyes (a) [37], (b) [35], (c) [25], (d) [38].....	16
Figure 3.2 (a) Illustration of the hemispherical compound eye. (b) Structure of conventional compound eye with key parameters: the acceptance angle ($\Delta\phi$) and focal length (f) for each ommatidium, the interommatidial angle ($\Delta\phi$), the diameter of a photodiode (p) and the radius of curvature of the compound eye (R) and of an individual microlens (r). (c) Compound eye imaging system.	23
Figure 3.3 Imaging systems of a conventional compound eye and the proposed COMPU-EYE. (a) The conventional compound eye consists of 8×8 ommatidia with $\Delta\phi = 1.5^\circ$ and $\Delta\phi = 1.5^\circ$. (b) COMPU-EYE consists of 8×8 ommatidia with $\Delta\phi = 1.5^\circ$ and $\Delta\phi = 8^\circ$ as well as a DSP algorithm.	29
Figure 3.4 Effects of acceptance angles for the conventional compound eye (top row) and COMPU-EYE (bottom row) (a)(d) Ommatidial receptive fields overlapped with the object image. (b)(e) Number of observing ommatidia corresponding to pixels in the 8 th row. (c)(f) Graphical representations of the measurement matrices.....	32
Figure 3.5 NMSE against acceptance angle where $M = 8 \times 8$ ommatidia with $\Delta\phi = 1.5^\circ$ and $N = 16 \times 16$ pixels.	35
Figure 3.6 Structures and fields of view of (a) conventional compound eye with $\Delta\phi_1 \leq \Delta\phi$ and (b) proposed COMPU-EYE system with $\Delta\phi_2 \gg \Delta\phi$	39
Figure 3.7 (a) Measurement matrices and (b) their number of nonzero elements per column for $d_1 = 2$ mm, $d_2 = 20$ mm, and $d_3 = 40$ mm, where $M = 5 \times 5$, $N = 12 \times 12$, $\Delta\phi = 12^\circ$, and $\Delta\phi = 30^\circ$	40
Figure 3.8 For $M = 80 \times 80$ and $\Delta\phi = 2.25^\circ$, (a) Output image of the conventional compound eye with $\Delta\phi = 2.25^\circ$ (b) Image recovered by COMPU-EYE with $\Delta\phi = 60^\circ$. For $M = 120 \times 120$ and $\Delta\phi = 1.5^\circ$.	

(c) Output image of the conventional compound eye with $\Delta\phi = 1.5^\circ$ (d) Image recovered by COMPU-EYE with $\Delta\phi = 60^\circ$	50
Figure 3.9 For the compound eyes, $M = 120 \times 120$ and $\Delta\phi = 1.5^\circ$. (a) Object image of 8-bit grayscale image with 160×160 pixels (b) Output image of the conventional compound eye with $\Delta\phi = 1.5^\circ$ and. (c) Image recovered by COMPU-EYE with $\Delta\phi = 60^\circ$	52
Figure 3.10 Resolution test: (a) Conventional compound eye consisting of 80×80 ommatidia with $\Delta\phi = \Delta\phi = 2.25^\circ$. (b) COMPU-EYE consisting of 80×80 ommatidia with $\Delta\phi = 60^\circ$ and $\Delta\phi = 2.25^\circ$...	53
Figure 3.11 Depth test: Image recovered by COMPU-EYE consisting of 100×100 ommatidia with $\Delta\phi = 60^\circ$ and $\Delta\phi = 1.8^\circ$, where the dimension of the final object image is (a) 30×30 mm at 5 mm, (b) 60×60 mm at 10 mm, (c) 90×90 mm at 15 mm. The actual tiger picture is 30×30 mm.	54
Figure 3.12 Depth estimation accuracy (%) with respect to depth interval.....	56
Figure 3.13 Proposed COMPU-EYE imaging system: (a) three-dimensional, (b) top, and (c) front views....	57
Figure 3.14 (a) Reconstruction of $\hat{\mathbf{v}}$, (b) reconstruction of $\hat{\mathbf{u}}$, (c) normalized regularized residuals, and (d) ommatidial observations and reconstructed images with respect to estimated distances.	59
Figure 3.15 An example of the iterative depth estimation method.....	61
Figure 3.16 Depth estimation and object reconstruction for a slanted object.....	62
Figure 4.1 (a) Grating-based spectrometer, (b) filter-array-based spectrometer.	69
Figure 4.2 Transmittance functions of (a) ideal filters and (b) non-ideal filters.....	70
Figure 4.3 TFs with various incident angles, (b) the amount of wavelength-shift with respect to the incident angle.	72
Figure 4.4 Schematic of the filter-array based spectrometer with DSP.....	75
Figure 4.5 (a) A Gaussian kernel with FWHM of 40 nm and center location of 800 nm (b) an example of sparse representation of object spectrum with $K = 3$	78
Figure 4.6 (a) Design structures of dielectric filters, (b) transmission spectra of filter 5 and 24.....	93
Figure 4.7 Implemented a 4×16 filter array.....	93

Figure 4.8 Design structures of dielectric filters.....	94
Figure 4.9 (a) Filter-array fabrication procedure, (b) a fabricated thin-film filter-array, (c) Monochrome image of the thin-film filter-array at a wavelength of 700 nm.	95
Figure 4.10 Setup for measuring the TFs	100
Figure 4.11 Measured transmittance functions.....	101
Figure 4.12 Spectral reconstructions of monochromatic light sources.....	102
Figure 4.13 Spectral reconstructions of (a) green LED and (b) red LED sources.	103
Figure 4.14 Residuals at different incident angles.....	104
Figure 4.15 Reconstruction performance when (a) incident angle is 10 degree and (b) 30 degree.	105

ABBREVIATIONS

2D	two dimensional
ADM	alternating direction method
CCD	charge coupled device
CS	compressed sensing
DMD	digital micromirror device
DOF	depth of field
DSP	digital signal processing
FOV	field of view
FWHM	full width half maximum
HSI	hyperspectral imaging
i.i.d.	independently and identically distributed
KKT	Karush-Kuhn-Tucker
LDPC	low density parity check
NMSE	normalized mean squared error
TF	transmittance function
SLM	spatial light modulator
SR	sparse representation
SRC	sparse representation-based classification

1 INTRODUCTION

The recent trend in optics is to merge an optical system hardware with digital signal processing (DSP) algorithms. These algorithms process the output of the system to remove hardware artifacts and thereby improve resolution. Single pixel cameras, lens-free cameras and compressive sensing microscopes are such innovative imaging through computation systems. They are recognized as prominent emerging technologies (e.g. MIT Tech. Reviews 2007, 2013) enabled by super-resolution algorithms evolved from the compressed sensing (CS) and sparse representation (SR) framework.

The use of CS and SR estimation algorithms are already proven to revolutionize imaging systems in many applications including compressive imaging architectures, medical imaging, remote surveillance, and spectroscopy [1]. For example, in single pixel cameras it has been shown that high resolution imaging is possible with the use of a single photo sensor [2]. There the researchers have utilized digital micro-mirror device (DMD) or spatial light modulators (SLM) to transform a scene in to compressed digital samples [3]. These digital samples are used for high resolution imaging through computation. However, DMD or SLM is expensive optical equipment and requires additional space.

In this dissertation, we study the resolution improvements in CS and apply the CS framework into two applications: 1) *Compound eye imaging systems* and 2) *Filter-based miniature spectrometers*. For reliable signal reconstruction with high resolution, we propose

- to design new analog hardware (ommatidia / optical filters) with holistic sampling capability
- to use DSP algorithms to reconstruct the desired input signal from the compressed measurements.

1.1 Outline of the dissertation

This dissertation is organized as follows: the compressed sensing theory is introduced in Chapter 2. In Chapter 3, we propose a computational compound eye (COMPU-EYE), which were published in [4, 5].

- [4] **W.-B. Lee**, H. Jang, S. Park, Y. M. Song, and H.-N. Lee, "COMPU-EYE: a high resolution computational compound eye," *Optics Express*, vol. 24, no. 3, pp. 2013-2026, 2016/02/08 2016.
- [5] **W.-B. Lee** and H.-N. Lee, *Depth-estimation-enabled compound eyes*. 2018, pp. 178-185.

In Chapter 4, we propose a compressive spectrometer in the CS framework, some part of which were published in [6-10] .

- [6] J. Oliver, **W. Lee**, S. Park, and H.-N. Lee, "Improving resolution of miniature spectrometers by exploiting sparse nature of signals," *Optics Express*, vol. 20, no. 3, pp. 2613-2625, 2012/01/30 2012.
- [7] J. Oliver, **W.-B. Lee**, and H.-N. Lee, "Filters with random transmittance for improving resolution in filter-array-based spectrometers," *Optics Express*, vol. 21, no. 4, pp. 3969-3989, 2013/02/25 2013.
- [8] **W.-B. Lee**, O. James, S.-C. Kim, and H.-N. Lee, "Random optical scatter filters for spectrometers: Implementation and Estimation," in *Imaging and Applied Optics*, Arlington, Virginia, 2013, p. JTU4A.33: Optical Society of America.
- [9] **W.-B. Lee**, C. Kim, G. W. Ju, Y. T. Lee, and H.-N. Lee, "Design of thin-film filters for resolution improvements in filter-array based spectrometers using DSP," in *SPIE Commercial + Scientific Sensing and Imaging*, 2016, vol. 9855, p. 6: SPIE.
- [10] C. Kim, **W.-B. Lee**, *et al.*, "A method of incident angle estimation for high resolution spectral recovery in filter-array-based spectrometers," in *SPIE OPTO*, 2017, vol. 10117, p. 6: SPIE.

In Chapter 5, we conclude this work.

2 RESOLUTION IMPROVEMENTS IN COMPRESSED SENSING

Compressed sensing (CS) is a data acquisition framework which has received great interests in electrical engineering, signal processing, and computer science [1]. Since its initial advent in 2006, a lot of studies and developments have been established as a successful paradigm of signal acquisition to date. In this chapter, we introduce the basic CS theory, its resolution improvement perspective, and two applications of the CS framework for resolution improvements.

2.1 Compressed sensing

Compressed sensing (a.k.a. compressive sensing or compressive sampling) is a new signal acquisition framework that requires far fewer measurements than traditionally assumed Nyquist sampling rate [1]. Since the seminal work of D. Donoho [11] and E. J. Candès [12] in 2006, CS has attracted considerable attention in the areas of applied mathematics, computer science, and electrical engineering [1].

In the traditional signal acquisition (or sampling) system, the signal is measured by uniformly acquiring (or sampling) the signal. In contrast, in the CS framework, the sampling and

compression is integrated into one step, by measuring few samples. In CS, each measurement (\mathbf{y}) is modeled as a linear projection of the input signal (\mathbf{x}) via measurement matrix (Φ) that contains the encoding coefficients. In mathematical expression, M linear measurements $\mathbf{y} \in \mathbb{R}^M$ can be obtained by

$$\mathbf{y} = \Phi \mathbf{x} + \mathbf{n} \quad (1)$$

where $\mathbf{x} \in \mathbb{R}^N$ is an input signal, $\Phi \in \mathbb{R}^{M \times N}$ is an $M \times N$ measurement matrix and $\mathbf{n} \in \mathbb{R}^M$ is a noise vector. The number of measurements M is smaller than N , i.e., $M < N$.

The CS theory asserts that if the signal \mathbf{x} is sparse, or compressible, and the signal acquisition protocol (Φ) is well-designed, it is possible to reconstruct \mathbf{x} from far fewer measurements \mathbf{y} by convex programming [13].

2.1.1 Sparsity

Any natural signal or a vector \mathbf{x} in (1) can be directly sparse or represented as sparse in a certain basis, i.e., $\mathbf{x} = \Psi \mathbf{s}$. The basis Ψ is an $N \times N$ matrix called sparsifying basis and the signal \mathbf{s} is K -sparse, i.e., only K components of \mathbf{s} are non-zero and the remaining $N - K$ components are zero. Therefore, the natural signal is a linear combination of only K columns of

the matrix Ψ . We note that when $\Psi = I$, the identity matrix, $\mathbf{x} = \mathbf{s}$; such a signal \mathbf{x} is called a directly sparse signal, i.e., it is inherently sparse [14].

Now, using the sparse representation of $\mathbf{x} = \Psi\mathbf{s}$, (1) can be rewritten as

$$\mathbf{y} = \Phi\mathbf{x} = \Phi\Psi\mathbf{s} = \Theta\mathbf{s} \quad (2)$$

where $\Theta = \Phi\Psi$ is an $M \times N$ matrix. We note that the dimension of \mathbf{y} is $M \times 1$, Φ is $M \times N$ and \mathbf{s} is $N \times 1$.

In an underdetermined system, the solution can be found by solving the l_0 minimization problem

$$\hat{\mathbf{s}} = \arg \min_{\mathbf{s}} \|\mathbf{s}\|_0 \quad \text{subject to } \|\Theta\mathbf{s} - \mathbf{y}\|_2 \leq \varepsilon. \quad (3)$$

where $\|\mathbf{s}\|_0$ denotes the number of non-zero components in \mathbf{s} and ε is a small positive constant.

However, the optimization problem in (3) is combinatorial and computationally intractable [14].

Alternatively, the l_1 norm minimization provides unique and sparse solutions for underdetermined systems by solving [15]

$$\hat{\mathbf{s}} = \arg \min_{\mathbf{s}} \|\mathbf{s}\|_1 \quad \text{subject to } \|\Theta\mathbf{s} - \mathbf{y}\|_2 \leq \varepsilon., \quad (4)$$

where Ψ is the sparsifying basis in which the signal \mathbf{x} can be approximated with just a small number of nonzero elements, $(\cdot)^*$ denotes the conjugate transpose of a matrix, and $\|\cdot\|_1$ denotes the l_1 norm, that is, the sum of the absolute values of the vector elements.

2.1.2 Incoherence

In CS, the measurement matrix Φ is chosen such that it captures enough information for the unique identification of the signal s with as few samples $y = \Phi\Psi s$ (the compressed measurements) as possible. In order to quantify the ability of the measurement matrix to acquire enough information about the signal in a minimum number of raw samples, the mutual coherence metric, μ , is used [1]. The mutual coherence of the matrix $\Theta = \Phi\Psi$ is defined as follows:

$$\mu = \max_{i \neq j} \frac{|\langle \alpha_i, \alpha_j \rangle|}{\|\alpha_i\|_2 \|\alpha_j\|_2}, \quad i, j = 1, \dots, N \quad (5)$$

where α_i is the i^{th} column of Θ . The μ is a measure of the maximum possible correlation among pairs of columns of Θ . The smaller μ is, the smaller the correlation among the columns of Θ is. Thus, in CS, it is desirable to design the measurement matrix Φ , such that the matrix $\Theta = \Phi\Psi$ has low coherence.

It is well known in CS that sensing matrices Θ , the entries of which are drawn from i.i.d. samples of a random variable, exhibit low coherence. Such matrices are called random measurement matrices. These matrices are capable of capturing enough information about the signals s to perform reconstruction from a small number of samples of y [15, 16]. In the literature, it is shown that the number of measurement is $M = O(K \log(N/K))$ to successfully recover K -

spars signal with the masurement matrix with Gaussian entries [14]. According to the CS-based applications, structured measurement matrices are constructed in a deterministic manner with well-known Fourier, Hadamard, noiselet, and Toeplitz matrices [17, 18] .

2.2 Compressed sensing for resolution improvement

As we have mentioned briefly, CS also exploits the sparse nature of signals by means of sparse representation. The purpose of CS as the name indicates is to compress a given signal of a fixed ambient dimension. The quality of the signal degrades with aggressive compression. In [2, 19], compressive sensing examples are introduced in optical systems. Reversely, however, the quality (resolution) of the recovered signal can be improved given a fixed number of observations of the signal by utilizing the prior information about the signal. The signal dimension is increased (by increasing N) purposely.

2.3 Research motivation

In this work, we apply the CS framework to the *compound eye imaging systems* and *filter-based miniature spectrometers* in order to improve resolutions. Both systems have a similar structure of signal acquisition. That is, the compound eye imaging system consists of a set of ommatidia, each of which is a basic sampling unit in the spatial domain and is conventionally designed to have independent receptive field of view of object with each other. In the filter-based miniature spectrometer, each filter plays a role as the basic sampling unit in the spectral domain and is conventionally designed to have independent transmittance function with each other. Resolutions in both systems are determined by the number of ommatidia and the number of filters, respectively, when they have ideal sampling capabilities, i.e., perfect isolation in the ommatidial receptive fields and filters' transmittance functions. To improve the resolutions, more number of ideal ommatidia or filters are needed. But, practically, the number of ommatidia or filters with ideal sampling capabilities is limited by up to date on the latest developments of fabricating the ommatidia or optical filters.

When the number of sampling units is limited in such cases of the *compound eye imaging systems* and *filter-based miniature spectrometers*, we exploit the CS framework for the resolution improvements beyond the conventional limit that ideal sampling units can achieve. For applying CS framework, two conditions need to be satisfied: sparse representation of the signal and incoherent measurement matrix. For sparse representation, image signals in the compound eye

imaging systems are sparsely represented in the wavelet transform domain and spectral signals in the spectrometers are sparsely represented with Gaussian basis. For incoherent measurement matrix, we propose to design measurement matrices customized for both systems in the context of CS. The motivations behind designing custom measurement matrices are based on the following observations:

- 1) ***Holistic sampling.*** In the traditional signal acquisition (or sampling) system, when no DSP is used, unintentional capturing of information from out of assigned range is considered as distortions or interferences to be avoided and thus the sampling units are designed to have the ideal sampling capabilities. However, in a completely different point of view, the unwanted interferences in the non-ideal sampling can be regarded as an additional source from which useful information can be extracted. In the CS framework, fewer number of samples contain enough information for reconstruction. Namely, because of compressive sampling (encoding and compression), each sample contains extra information about the entire signal rather than the only about a particular part of the signal as an ideal sampling does. That is, each measurement collects information from the entire signal and encodes it into a single sample. Since the encoding pattern of one measurement is different from that of all other measurements, we can obtain many such independent holistic information of

the entire signal. Thus, it is natural to determine the pattern of linear projection for more holistic and independent information about the input signal.

- 2) ***Designable measurement matrix.*** The l_1 -norm minimization-based DSP algorithms reconstruct the input signal reliably from fewer measurements. For the signal reconstruction, the sparsifying matrix Ψ is determined with respect to the signal that is dealt with. However, the measurement matrix Φ can be determined from the design and implementation of the system such as acceptance angles in compound eye imaging system and optical filters in spectrometers. Hence, we conclude that a good design for the measurement matrix is important in order for the DSP algorithm to reconstruct the input signal from fewer measurements.
- 3) ***Analog device.*** The measurement matrix is usually designed in the digital domain by digital micro-mirror-device (DMD) or spatial light modulators (SLM) with encoding coefficients of Fourier, Walsh-Hadamard, or noiselet transform matrix [2]. But, such devices require additional space and cost. Instead of using such devices, we propose to modify the existing system just adjusting for CS sampling.

In summary, we present to design the measurement matrices of the *compound eye imaging systems* and *filter-based miniature spectrometers* in the context of CS for resolution improvements.

3 COMPU-EYE: COMPUTATIONAL COMPOUND EYES

In nature, compound eyes of arthropods have been evolved towards a wide field of view (FOV), an infinite depth of field (DOF) and fast motion detection. However, the compound eyes have inferior resolution compared to single-lens eyes of vertebrates owing to inherent structural constraints such as optical performance of ommatidia and interommatidial angles. Here, for resolution improvement of the compound eye, we propose a COMPUtational compound EYE (COMPU-EYE). COMPU-EYE contains a new design concept which is to increase the angle of acceptance of ommatidia and a modern digital signal processing technique. The increase in the angle of acceptance enables a single ommatidium to observe multiple pieces of information all at once. Since the multiple information is superposed at a single photodetector in the ommatidium, each ommatidium is unable to resolve them and the observed image is highly distorted. Contrarily, the increased acceptance angle enables each piece of information to be observed multiple times with different perspectives by multiple ommatidia. By exploiting this, when we use a modern DSP technique for resolving the unfavorable interferences, we can achieve resolution improvements. Furthermore, we propose a depth estimation algorithm to enable COMPU-EYE to estimate object distances by exploiting disparities between the ommatidial receptive fields, and sparse representation.

3.1 Compound Eyes

There are two kinds of vision systems in nature. One is single-lens eye that is easily found in humans and another is compound eye that can be found mostly in insects. Each visual system has been evolved with respect to environments of living things. For example, the single-lens eyes are specialized in resolution and the compound eyes are specialized in motion detection. By imitating the structure of single-lens eyes of humans, cameras were developed in the past. Nowadays the compound eyes of arthropods such as ants, flies and bugs have attracted extensive research interest due to their unique features such as wide field-of-view (FOV), high sensitivity to motion and infinite depth of field [20-22]. Compound eye consists of integrated optical units called ommatidia, each of which, called ommatidium, includes a light diffracting facet lens, crystalline cone, wave guiding rhabdom and photoreceptor cell [23-25]. Each ommatidium arranged along a spherical surface senses incident light within a small range of angular acceptance. Implementations of optical devices inspired by natural compound eyes exhibit great potential in various fields such as surveillance cameras on micro aerial vehicles, high-speed motion detection, endoscopic medical tools, and image guided surgery [26, 27].

For years, there have been many attempts to develop artificial compound eyes based on microlenses and photodetectors to imitate imaging organs of a natural ommatidium. Because most optoelectronics technologies developed earlier were intrinsically based on a planar substrate, both microlenses and photodetectors were implemented on a plane [28-30]. Planar compound eyes had low design and fabrication complexity, but they incurred a limited FOV. Later, curved microlens arrays were developed and interfaced with conventional planar sensors [31-36], but these suffered from off-axis aberrations, crosstalk between adjacent ommatidia, or restricted FOV [37]. They also required optical relay devices for beam-steering, which are complicated to fabricate [34-36]. In recent years, with the advance of flexible optoelectronics [38], curvilinear structured compound eyes, which provide larger FOVs, have been developed [27, 37, 39, 40]. A hemispherical omnidirectional optical sensor was implemented by a circular central board and multiple modular sensor boards [39]. A cylindrical compound eye was introduced by bending the planar ommatidial array along a concave substrate [37]. In [40], a set of pinhole cameras are implemented on the hemisphere. Song. *et al.* implemented a hemispherical compound eye by reformulating stretchable planar ommatidia into hemispherical ommatidia [27]. We note that the hemispherically structured compound eye developed in [27], which is most comparable to a natural compound eye is mainly considered in this work.

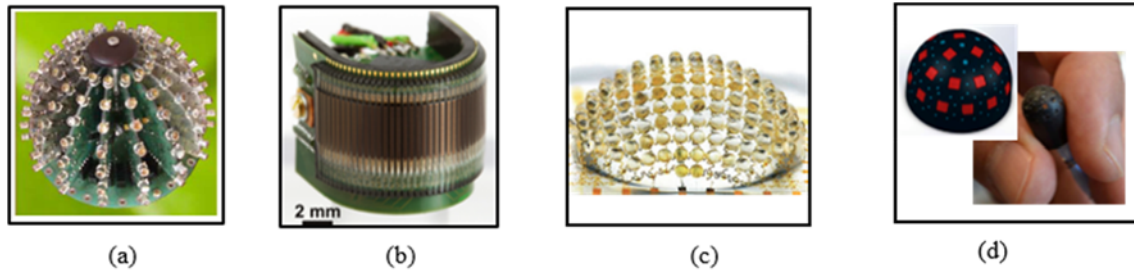


Figure 3.1 Artificial compound eyes (a) [37], (b) [35], (c) [25], (d) [38]

3.1.1 Resolution limit in compound eyes

It is well known that the vision of insects is far inferior to that of humans because of inherent structural constraints [41-43]. Generally, the resolution of any eye depends not only on its optical resolution but also on the number of the receptors. First, if the optics are free of defects, the resolution of any optical imaging system is determined by its diffraction limit. The resolution of a diffraction-limited imaging system is proportional to the size of its lens and inversely proportional to the wavelength of the observed light. Second, in apposition-type compound eyes, the basic sampling units are ommatidia rather than photoreceptors. In a diffraction-limited compound eye, in order to accommodate many separate ommatidia without crosstalk, the number of ommatidia is much smaller than that of photoreceptors in the retina of a human eye. In nature, the density of the photoreceptors in the human eye is about 25 times higher than the ommatidial density of the compound eye [44]. For a compound eye to achieve a resolution similar to that of

a human eye, it requires a radius of about 6 m and millions of ommatidia with facet lenses as large as a pupil, which is impractical [41].

Artificial compound eyes that mimic the structure of natural compound eyes are also limited on their image resolutions. In the design of the compound eyes, the spatial resolution that the compound eye can resolve depends on the relation between the acceptance angle ($\Delta\phi$) of the ommatidia and the interommatidial angle ($\Delta\phi$) between the optical axes of the neighboring ommatidia [41, 45]. In nature, for most light-adapted diurnal animals, the acceptance angles of ommatidia approach the interommatidial angle, i.e., $\Delta\phi \approx \Delta\phi$ [41], which achieves high spatial resolution by minimizing aliasing among neighboring ommatidia. For example, *Tenodera* has angles $\Delta\phi = 0.7^\circ$ and $\Delta\phi = 0.6^\circ$, and *Calliphora* has angles $\Delta\phi = 1.02^\circ$ and $\Delta\phi = 1.5^\circ$. Analogous to natural compound eyes, artificially developed compound eyes have been designed to have similar acceptance and interommatidial angles [27, 37]. The acceptance and interommatidial angles have been chosen to be $\Delta\phi = 9.7^\circ$ and $\Delta\phi = 11^\circ$, and $\Delta\phi = 4.2^\circ$ and $\Delta\phi = \sim 4.2^\circ$ in the literature [27, 37]. Compared to the human eye, the artificial compound eyes are fundamentally limited on the resolution and thus they are inappropriate for object recognition.

For improving the quality of the observed image, a scanning method was introduced by capturing the object image repeatedly with different angle of rotations in [27, 46]. As a result, an image of 160×160 pixels was obtained only with 16×16 ommatidia by scanning the compound-

eye camera and thus the actual resolution of the observed image was improved by 100 times [27]. However, the repeated image capturing with fine mechanical angle controls makes the scanning method inefficient. In [47], a compact imaging system called TOMBO (thin observation module by bound optics) was introduced, which consists of a multi-aperture imaging system and a post-signal processing. The TOMBO reconstructs the object image with high resolution from multiple low-resolution subimages by exploiting the relation between the object and the captured signals. Afterward, many techniques were proposed to improve the reconstruction performance of the TOMBO system [47, 48]. However, the FOVs are limited because they are planar compound eyes.

3.1.1.1 *Related works of resolution improvements*

For a classical resolution improvement technique, a microscan technique requires to capture multiple frames of a target with slightly displaced locations [48]. The sequences of frames are then integrated to form a high-resolution image. In contrast, COMPU-EYE provides a high-resolution image reconstruction with a single frame of the target with less number of samples. The high-resolution reconstruction is achieved by solving an underdetermined linear system of equations as will be introduced in (6). As a fast-emerging area in DSP, CS provides a sparse solution to the underdetermined system. Recently, there are other papers who studied CS with the

intension of improving resolution in various areas such as spectroscopy [7], optical imaging [49], and direction of arrival estimation [50]. In this paper, we propose to design a compound eye with large ommatidial acceptance angles, which is appropriate for the framework of the CS-based super-resolution, and to reconstruct the object with high resolution using the DSP technique.

3.1.2 Depth estimation in compound eyes

Visual methods for depth estimation can be grouped into two main categories based on whether they use binocular or monocular cues [51]. Binocular cues are obtained from the minor disparities between the views of two eyes when the eyes are located close to one another and have overlapping views. These slightly different images of the same scene are sent to the brain and integrated into a single image containing depth information [52]. By contrast, monocular cues are obtained from two-dimensional images captured by a single eye; these cues include interposition, motion parallax, relative size and clarity, texture gradient, linear perspective, and light and shadow [51].

Some insects, such as praying mantids, that have binocular vision systems in the fronts of their heads use binocular cues to estimate target distances [52, 53]. However, unlike humans' camera-like eyes that can focus on objects by changing the shapes or positions of their lenses, insects' compound eyes are inherently immobile and unable to focus owing to their structural limitations

[51]. Thus, the binocular cues used for depth estimation in compound eyes are much less efficient, yielding images with low spatial resolutions and limited effective depth estimation ranges [54, 55].

Insects can also estimate object distances using monocular cues. The motion parallax of objects in a visual scene that is caused by the relative motion between the observer and the objects yields information about object distances [51, 56]. Specifically, nearby objects produce more apparent motion than distant ones. Insects' visual systems can easily detect the depths of objects that move independently of their surroundings by using motion parallax. For example, grasshoppers judge depths accurately by using the motion parallax generated by peering movements, that is, by moving their head from side to side [52], and bees measure distances by monitoring the apparent motion of an object relative to its surroundings [57].

Recently, artificial compound eyes that mimic natural compound eyes have been proposed. In these eyes, each ommatidium (individual imaging unit) has a limited acceptance angle, thus avoiding optical crosstalk among neighboring ommatidia [40, 56, 58, 59]. In [56, 58], object depths were estimated using monocular cues from optic flows (i.e., pattern of apparent motion) based on the phenomenon in which a closer object appears to move faster than a farther one. However, this method requires rotation or movement of the compound eye.

3.1.2.1 *Related works of depth estimation*

Depth estimation using the disparities between multiple subimages has been studied in multicamera systems such as integral imaging [60]. Integral imaging is a three-dimensional imaging and sensing system that uses an array of optical units. Each optical unit consists of a microlens and an array of photosensors, and it produces an elemental image. From multiple elemental images, a three-dimensional image is reconstructed optically or computationally [61]. In [62], an iterative reconstruction algorithm was proposed for improving image quality given distance information. A stereo matching method that used the spatial variations of parallax shifts in elemental images was proposed for depth estimation [63, 64]. We note that multicamera setups are essentially different from our work. First, our structure can be considered a degraded integral imaging system with a single photosensor in each elemental image; this imitates the structure of apposition compound eyes found in nature. The number of sensors is thus reduced dramatically, and the sensors can be implemented in a fully hemispherical structure that provides a large FOV [59]. Some studies on integral imaging considered curved surfaces for realizing a large FOV [65]. However, with planar sensors, they require additional optical components like random phase masks; otherwise, mismatch occurs [65]. Second, three-dimensional information is highly compressed using a single photosensor per lens. Thus, more sophisticated reconstruction algorithms are required for imaging and depth estimation.

3.1.3 Contributions of this chapter

In this section, instead of enhancing the size and number of the ommatidia for improving the resolution, we propose a totally different imaging system, called COMPU-EYE, using a modern DSP technique. Conventional compound eyes are designed to have limited ommatidial acceptance angles to avoid aliasing. Thus, each ommatidium of the conventional compound eye observes an independent section of the object image. In contrast, the ommatidium of COMPU-EYE has larger acceptance angles. This increase in acceptance angle allows a single ommatidium to observe multiple pieces of information simultaneously. Because the multiple pieces of information in each observation interfere with each other, the observed image is distorted. We employ a DSP technique in COMPU-EYE to recover the object image from these observations. In the DSP, by utilizing the fact that one piece of information is observed by multiple ommatidia with different perspectives, COMPU-EYE improves the resolution of the object image.

In addition, we also propose a method for estimating object depths in a monocular compound eye imaging system based on the computational compound eye (COMPU-EYE) framework described in [66]. In COMPU-EYE, each ommatidium has a larger acceptance angle than its interommatidial angle, causing the ommatidial receptive fields to overlap significantly. As in binocular depth estimation methods, depth estimation in COMPU-EYE involves processing the

multiple and slightly differing views received by the ommatidia by using a proposed digital signal processing (DSP) technique. Depth information can be estimated by using the dependences of the disparities between the ommatidial observations on object distance. We perform a numerical experiment to verify the effectiveness of the proposed method. In our experiment, we demonstrate that the proposed depth estimation technique can not only estimate the distances of multiple objects but also reconstruct object images with high resolution.

3.2 System model of compound eye imaging

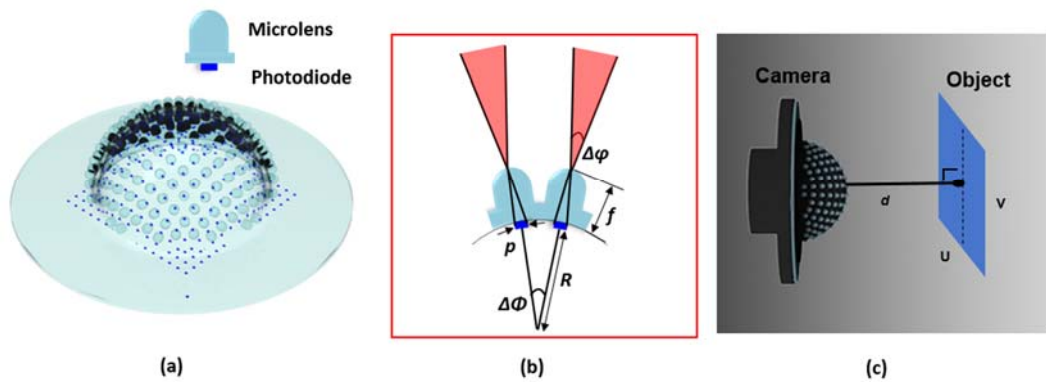


Figure 3.2 (a) Illustration of the hemispherical compound eye. (b) Structure of conventional compound eye with key parameters: the acceptance angle ($\Delta\phi$) and focal length (f) for each ommatidium, the interommatidial angle ($\Delta\phi$), the diameter of a photodiode (p) and the radius of curvature of the compound eye (R) and of an individual microlens (r). (c) Compound eye imaging system.

We consider the biologically inspired compound eyes of a hemispherical structure as seen in Figure 3.2 (a). Details of the optical design of the hemispherical compound eye is referred from [27]. Each ommatidium, a basic imaging unit can be implemented by a set of microlens, supporting posts connected to a base membrane and a photodetector. An array of microlenses and photodiodes are integrated in the planar layout and are transformed into a full hemispherical shape. Note that the ommatidium is based on a circular lattice because the microlens is hemispherical shape compared to the hexagonal lattice in compound eyes in nature [41]. Each ommatidium receives incident light within its acceptance angle defined by $\Delta\phi$ and is separated by an interommatidial angle $\Delta\phi$ from each other. We note that the optical transfer function of an ommatidium can be modeled as a Gaussian function. For simplicity, we assumed that the optical transfer function is simplified by neglecting light whose relative light intensities are smaller than a certain value. Thus, each ommatidium is modeled to collect averaged optical signal from light incident within its acceptance angle, $\Delta\phi$, as seen in Figure 3.2 (b). With the compound eye of the hemispherical structure, we now consider an imaging system with M ommatidia as seen in Figure 3.2 (c). The imaging system observes an object image on the plane size of $U \times V$ mm, which is located d mm away from the compound eye. According to the acceptance angle and object image distance, the receptive field (i.e., visible area at the object plane) of a single ommatidium is determined. Each observation contributes to a single pixel that contains the intensity of the light

collected from its corresponding receptive field. The final image is reconstructed by a set of these pixels.

Let y_i denote an output sample at the i^{th} ommatidium for $i \in \{1, 2, \dots, M\}$. We assume that the image to be reconstructed consists of N_U by N_V pixels, each having uniform light intensity. The size of each pixel is $U/N_U \times V/N_V$ mm. The object image forms an $N \times 1$ vector $\mathbf{x} = [x_1, x_2, \dots, x_N]^T$, where $N = N_U N_V$. On the basis of ray tracing analysis, the sample y_i can be obtained from $y_i = \mathbf{a}_i \mathbf{x}$, where \mathbf{a}_i is an $1 \times N$ vector whose elements represent the visibility of the i^{th} ommatidium at each of the N pixels. For the i^{th} ommatidium, if the j^{th} pixel for $j \in \{1, 2, \dots, N\}$ is outside the receptive field, which represents the j^{th} pixel is invisible to the i^{th} ommatidium, then the j^{th} component a_{ij} in \mathbf{a}_i becomes zero, i.e., $a_{ij} = 0$. If the j^{th} pixel is inside the receptive field, which represents the j^{th} pixel is fully observed by the i^{th} ommatidium, then $a_{ij} = 1$. Otherwise, if the j^{th} pixel is on the boundary of the receptive field, which represents the j^{th} pixel is partially observed by the i^{th} ommatidium, then $0 < a_{ij} < 1$, which is proportional to the intersection area of the receptive field and pixel. This process can be summarized as follows:

$$a_{ij} = \begin{cases} 0 & , j^{\text{th}} \text{ pixel is invisible to } i^{\text{th}} \text{ ommatidium} \\ 1 & , j^{\text{th}} \text{ pixel is fully observed by } i^{\text{th}} \text{ ommatidium} \\ 0 < a_{ij} < 1, & j^{\text{th}} \text{ pixel is partially observed by } i^{\text{th}} \text{ ommatidium} \end{cases} .$$

When collecting M samples, the ommatidial observations can be modeled as a system of linear

equations as follows:

$$\mathbf{y} = \mathbf{A}\mathbf{x} + \mathbf{n}. \quad (6)$$

where $\mathbf{y} = [y_1, \dots, y_M]^T$ is a set of M output samples and $\mathbf{n} \in \mathbb{R}^{M \times 1}$ contains unexpected noise.

Let $\mathbf{A} = [\mathbf{a}_1^T \ \mathbf{a}_2^T \ \dots \ \mathbf{a}_M^T]^T \in \mathbb{R}^{M \times N}$ denote a measurement matrix the i^{th} row of which is \mathbf{a}_i .

Given the measurement matrix \mathbf{A} and the observation \mathbf{y} , we aim to solve the system of linear equations in (6) for the object image reconstruction.

In this paper, since we are considering resolution improvements in the compound eye imaging system, the number of estimated pixels is set to be greater than the number of ommatidia. i.e., $N > M$. Thereby, we note that (6) becomes an underdetermined system of linear equations. This underdetermined system can be solved by a convex optimization if the object is represented as a sparse signal in the proper domain [11, 67, 68]. A sparse signal is often represented as a vector which has a small number of non-zero components. We note that any natural image can be sparsely represented in a certain domain such as wavelets, the discrete cosine transform (DCT), or the discrete Fourier transform [12, 69]. That is, $\mathbf{x} = \mathbf{W}^T \mathbf{s}$ and $\mathbf{W}\mathbf{x} = \mathbf{s}$, where \mathbf{s} is a sparse $N \times 1$ vector and \mathbf{W} is an $N \times N$ sparsifying matrix. By exploiting the sparse representation of \mathbf{x} , (6) can be expressed as

$$\mathbf{y} = \mathbf{A}\mathbf{W}^T \mathbf{s} + \mathbf{n}. \quad (7)$$

In an underdetermined system, the solution can be found by solving the l_1 minimization problem

$$\hat{\mathbf{s}} = \arg \min_{\mathbf{s}} \|\mathbf{s}\|_1 \quad \text{subject to} \quad \|\mathbf{A}\mathbf{W}^T \mathbf{s} - \mathbf{y}\|_2 \leq \varepsilon. \quad (8)$$

From $\hat{\mathbf{s}}$, the object image can be reconstructed by solving $\mathbf{x} = \mathbf{W}^T \hat{\mathbf{s}}$.

We note that the l_1 norm minimization guarantees stability, which means that it can reliably reconstruct the signal without amplifying the observation errors in the process of l_1 norm minimization [70, 71]. The l_1 norm minimization reconstructs a signal with explicit sparsity constraints while removing non-sparse random noise components from a corrupted signal. Due to its property of noise suppression, the l_1 norm minimization has been used as an image denoising tool [72]. Recently, many algorithms [73-75] have been proposed to solve (8). In this study, we use the alternating direction method [75], which is known to be fast and efficient for the problem in (8). If an object image of N pixels is reconstructed, where $N > M$, the resolution of COMPU-EYE is improved by a factor of N/M .

In the following section, we propose a COMPU-EYE imaging system, which is more appropriate to resolve (8) and thus to reconstruct the object image with high resolution.

3.3 COMPU-EYE for image acquisition and reconstruction with high resolution

In this section, we introduce COMPU-EYE. In COMPU-EYE, we propose to increase the acceptance angles of ommatidia larger than the interommatidial angle to recover the object image with computations. We first compare COMPU-EYE with the conventional compound eye imaging system in terms of resolution limit. We then explain how COMPU-EYE improves the resolution by investigating the influence of larger acceptance angles on the measurement matrix of the image capturing system.

3.3.1 Overview and comparison of compound eyes

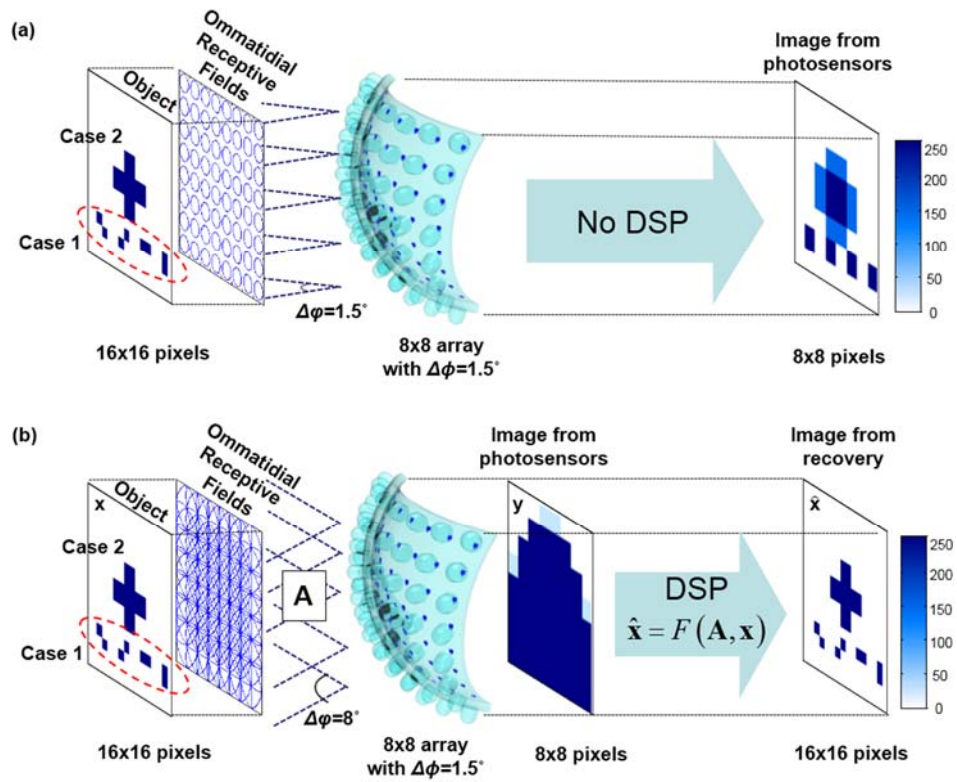


Figure 3.3 Imaging systems of a conventional compound eye and the proposed COMPU-EYE. (a) The conventional compound eye consists of 8×8 ommatidia with $\Delta\phi = 1.5^\circ$ and $\Delta\phi = 1.5^\circ$. (b) COMPU-EYE consists of 8×8 ommatidia with $\Delta\phi = 1.5^\circ$ and $\Delta\phi = 8^\circ$ as well as a DSP algorithm.

The imaging system of a conventional compound eye is depicted in Figure 3.3 (a). It has a hemispherical structure with a radius (R) of 6.9216 mm, and consists of 8×8 ommatidia, each of which has a height (f) of 1.35 mm. Because each ommatidium provides a single sample, the compound eye has $M = 64$ samples. An 8×8 mm object image is located at a distance of 30 mm from the compound eye. The receptive field of a single ommatidium is shown as an ellipse, and

a set of these receptive fields forms the ommatidial receptive fields near the left in Figure 3.3 (a).

In the conventional compound eye, the acceptance angles of the ommatidia are typically designed to be similar to the interommatidial angle (i.e., $\Delta\phi = \Delta\phi = 1.5^\circ$) in order to maximize the spatial resolution as well as to avoid overlapping ommatidial receptive fields. Accordingly, the ommatidial receptive fields are totally isolated, and each ommatidium observes an independent part of the object image. Each observation forms a single pixel in the reconstructed image. Note that no signal processing technique is needed to reconstruct the image.

To demonstrate the resolution limit of the conventional compound eye, we consider an object image comprising two parts as seen in Figure 3.3 (a): 1) four different patterns with the same light intensity, each of which is included in the receptive field of an ommatidium; and 2) a cross pattern that lies over several receptive fields.

Because every pattern in Case 1 is included within a receptive field, every observation appears to have a single image pixel with the same intensity of light. As a result, finer details within a receptive field cannot be resolved and the four different patterns in Case 1 cannot be distinguished by a conventional compound eye. Moreover, because its ommatidial receptive fields are totally isolated, the fields contain *undetectable areas*, i.e., areas that are invisible to the compound eye. The undetectable areas deteriorate the image quality by decreasing the intensity of light observations as seen in right side of Figure 3.3 (a). This example shows that the conventional

compound eye roughly recognizes object patterns but has undetectable areas. As a result, such compound eyes suffer from limited resolution and poor image quality.

In contrast, consider the proposed COMPU-EYE imaging system in Figure 3.3 (b). COMPU-EYE consists of an 8×8 hemispherical array of ommatidia with acceptance angles that are larger than the interommatidial angle, i.e., $\Delta\phi = 8^\circ > \Delta\phi = 1.5^\circ$. It is also equipped with a DSP technique. Because of the increased acceptance angles, the receptive field of each ommatidium is increased to at least 28 times that of $\Delta\phi = 1.5^\circ$. Thus, the ommatidial receptive fields widely overlap, severely distorting the observations as seen in the third frame from left in Figure 3.3 (b). We then apply DSP to recover a high-resolution object image from these highly distorted observations.

In Figure 3.3 (b), the proposed COMPU-EYE recovers an object image of 256 pixels from 64 observations. The resolution is improved by a factor of four. In recovered image \hat{x} , finer details that were perceived as a single point in Figure 3.3 (a) can be resolved, and different patterns in Case 1 are distinguished by COMPU-EYE. Moreover, COMPU-EYE compensates for undetectable areas and hence prevents the deterioration of the recovered image quality in Case 2. As a result, COMPU-EYE provides a higher-resolution image of better quality than the conventional compound eye.

3.3.2 Effects of large acceptance angles and resolution improvements

We now focus on how larger acceptance angles along with the DSP technique improve resolution with respect to measurement matrix characteristics of the conventional compound eye and COMPU-EYE.

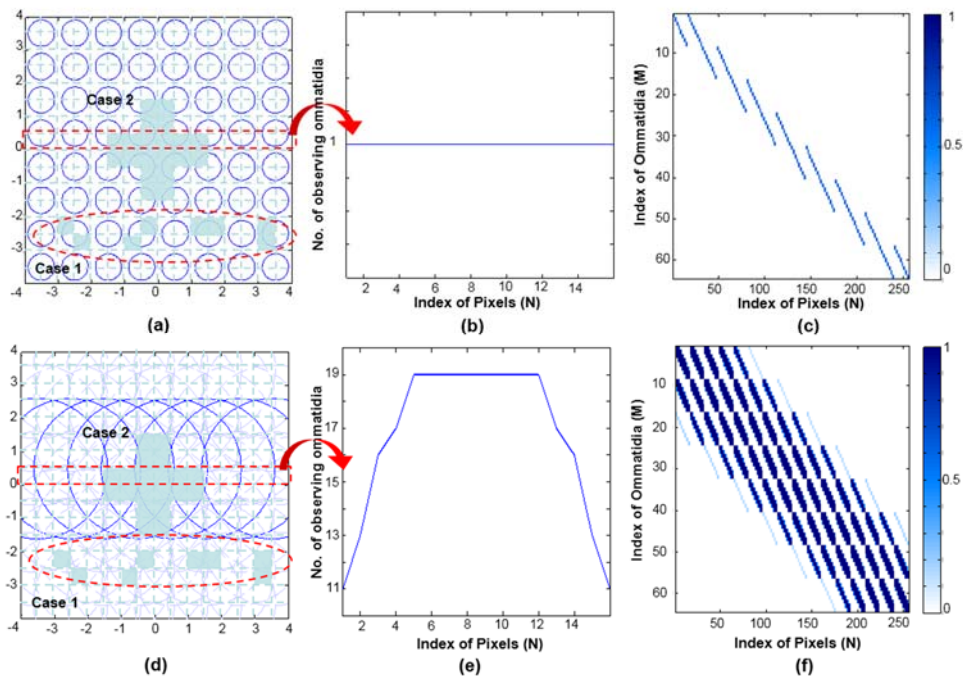


Figure 3.4 Effects of acceptance angles for the conventional compound eye (top row) and COMPU-EYE (bottom row) (a)(d) Ommatidial receptive fields overlapped with the object image. (b)(e) Number of observing ommatidia corresponding to pixels in the 8th row. (c)(f) Graphical representations of the measurement matrices.

Figure 3.4 (a) shows how the object image of a 16×16 array of pixels is projected onto the 8

$\times 8$ ommatidial receptive fields of the conventional compound eye, where $\Delta\varphi = \Delta\phi = 1.5^\circ$. The measurement matrix of the conventional compound eye $\mathbf{A} \in \mathbb{R}^{M \times N}$ in (6) can be obtained from the ommatidial receptive fields and pixels of the object image in Figure 3.4 (a). This measurement matrix is displayed graphically in Figure 3.4 (c). Every element in the measurement matrix indicates the visibility of the corresponding row of an ommatidium in the corresponding column of a pixel. Because the receptive fields of the ommatidia are small and isolated, the measurement matrix has few nonzero components. In Figure 3.4 (a), each ommatidium separately observes four corresponding pixels, and each pixel is observed by a single ommatidium. The values of the four pixels in one receptive field are considered to be of a single light intensity. Thus, each observation and its observed pixels are in a one-to-many correspondence relation. Because the information of one pixel is contained in one ommatidium as seen in Figure 3.4 (b), there is no additional information regarding that pixel in other observations. Therefore, in such relationships, finer details within the receptive field cannot be resolved and the resolution of the conventional compound eye is limited by M measurements. We note that the coefficients in Figure 3.4 (c) are smaller than one because the pixel cannot be entirely observed by ommatidia owing to the undetectable areas.

In contrast, COMPU-EYE has a larger acceptance angle of $\Delta\varphi = 8^\circ$. Figure 3.4 (d) shows how the object image is superimposed on the ommatidial receptive fields of COMPU-EYE. The size

of each receptive field is considerably larger; a single ommatidium covers up to 76 pixels, which is considerably greater than the four pixels of the conventional compound eye. Whereas each receptive field in the conventional compound eye is small and separated, each receptive field in COMPU-EYE is large and highly overlapped. Hence, undetectable areas do not exist in the receptive fields of COMPU-EYE. As a result, the number of nonzero components increases correspondingly in the measurement matrix of COMPU-EYE in Figure 3.4 (f).

The measurement matrix of COMPU-EYE is appropriate for image acquisition and reconstruction rather than that of the conventional compound eye because the object elements, \mathbf{x} in (6) is more likely to be aligned with the nonzero elements of the matrix [76]. As shown in Figure 3.4 (e), each pixel of the object image is observed multiple times with different ommatidia. In the context of information acquisition, the total quantity of information for a pixel is increased. Each observation is not redundant to the others for it has different receptive field. Accordingly, each column in the measurement matrix has multiple nonzero elements with different coefficients in Figure 3.4 (f). The observation of a pixel sufficiently differs from its other observations and this provides additional information about the pixel. In the literature, it is shown that such additional information is useful for reliable signal recovery, even if the number of measurements is smaller than the dimension of the original signal [12, 15, 49, 76, 77]. Thus, the large acceptance angle of ommatidia with the use of DSP allows COMPU-EYE to resolve finer details of the object

beyond the resolution limit of M measurements.

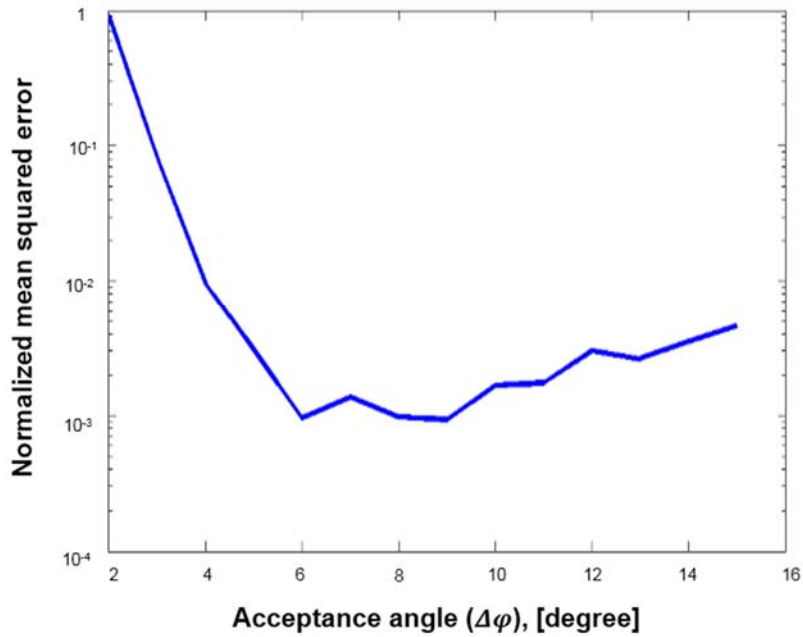


Figure 3.5 NMSE against acceptance angle where $M = 8 \times 8$ ommatidia with $\Delta\phi = 1.5^\circ$ and $N = 16 \times 16$ pixels.

We now investigate the reconstruction performance of the DSP technique in accordance with the acceptance angle in the example of Figure 3.3. A randomly located sparse signal with 10 nonzero components is generated with uniform distribution between 0 and 1. As a measure of the reconstruction performance evaluation, let us define the normalized mean squared error (NMSE) as $\text{NMSE} = \frac{\|\hat{\mathbf{x}} - \mathbf{x}\|_2^2}{\|\mathbf{x}\|_2^2}$. As seen in Figure 3.5, when the acceptance angle is small, the object is unable to be reconstructed with low errors. Specifically, when $\Delta\phi = 2^\circ$ which corresponds to

the conventional compound eye in the example of Figure 3.3 (a), the 16×16 pixels cannot be recovered from 8×8 ommatidia. Associated with the measurement matrix in Figure 3.4 (c), each observation and its corresponding observed pixels are one-to-many correspondence. Thus, each ommatidium is unable to resolve fine details of its observation. As the acceptance angle increases, each pixel is observed multiple times by different ommatidia. The DSP technique reconstructs each pixel with low errors by solving (8). As a result, the NMSE decreases. When $\Delta\phi > 8^\circ$, it is seen that the NMSE gradually increases because each observation becomes redundant with neighboring observations. We note that the acceptance angle can be easily increased in many possible ways in an artificial compound eye. The acceptance angle within an ommatidium can be represented as $\Delta\phi_o = \sqrt{(p/f)^2 + (\lambda/D)^2}$, where D is the lens diameter, λ is the light wavelength, p is the photosensor diameter, and f is the focal length of the ommatidial optics [41]. According to Snell's law, the acceptance angle $\Delta\phi$ outside the ommatidium can be obtained by $\Delta\phi = 2 \sin^{-1}((n_0/n_1) \sin(\Delta\phi_o/2))$, where the refractive indices of the lens material and air are defined as n_0 and n_1 , respectively. Thus, the acceptance angle $\Delta\phi$ can be increased by using a material of higher refractive index for the ommatidia, decreasing the focal length f , or increasing the diameter p of the photodetector. Note that increasing the diameter of the photodetector may lead to increase the size of the ommatidia and the size of the compound eye. On the other hand, decreasing the radius of the curvature of the microlens for reducing the focal length can increase

the acceptance angle without increasing the size of the ommatidia.

3.4 Depth-estimation-enabled compound eyes

Most animals that have compound eyes determine object distances by using monocular cues, especially motion parallax. In artificial compound eye imaging systems inspired by natural compound eyes, object depths are typically estimated by measuring optic flow; however, this requires mechanical movement of the compound eyes or additional acquisition time. In this paper, we propose a method for estimating object depths in a monocular compound eye imaging system based on the computational compound eye (COMPU-EYE) framework. In the COMPU-EYE system, acceptance angles are considerably larger than interommatidial angles, causing overlap between the ommatidial receptive fields. In the proposed depth estimation technique, the disparities between these receptive fields are used to determine object distances. We demonstrate that the proposed depth estimation technique can estimate the distances of multiple objects.

3.4.1 Depth estimation model

Given the structure of the compound eye, specifically, the acceptance angles, interommatidial

angles, and sizes of the compound eye and ommatidia, the receptive fields of ommatidia at a distance of d are determined. Thus, the measurement matrix in (7) can be characterized by the distance of the object. Let us denote $\mathbf{A}_d \in \mathbb{R}^{M \times N}$ as a measurement matrix corresponding to a distance of d . The data acquisition model for M ommatidial observations can be expressed as a system of linear equations as follows:

$$\mathbf{y} = \mathbf{A}_d \mathbf{x} + \mathbf{n}. \quad (9)$$

3.4.1.1 *Distance and measurement matrix*

The measurement matrix strongly depends on the object's properties, such as its distance. In previous section, the object distance was assumed to be fixed and known, and the measurement matrix corresponding to this distance was given to the DSP system. However, assuming prior knowledge about object distances is impractical in reality. The reconstruction process works well only if the measurement matrix is correct; if an inappropriate measurement matrix is used, then the reconstructed image is severely distorted.

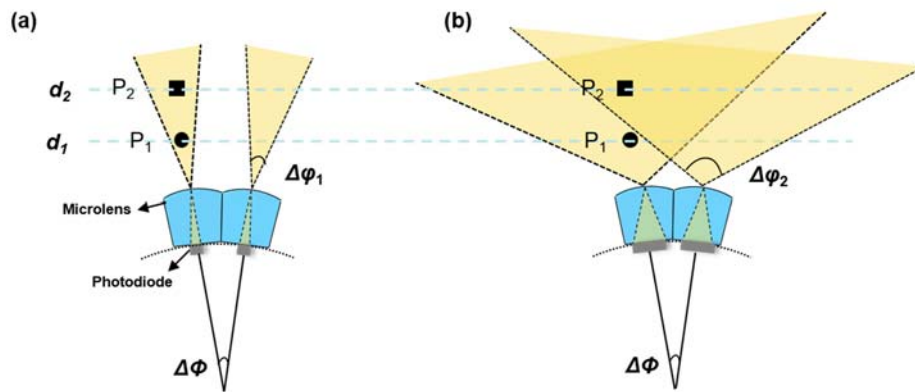


Figure 3.6 Structures and fields of view of (a) conventional compound eye with $\Delta\phi_1 \leq \Delta\phi$ and (b) proposed COMPU-EYE system with $\Delta\phi_2 \gg \Delta\phi$.

In the framework of COMPU-EYE imaging, we propose a new depth estimation method. In conventional compound eyes, $\Delta\phi$ is designed to be smaller than or equal to $\Delta\phi$ to avoid aliasing [27, 37, 40]. As shown in Figure 3.6 (a), each ommatidium observes an independent section within $\Delta\phi$. Consider two objects, P_1 and P_2 , that are located at different distances from a compound eye. If the objects are observed by a single ommatidium in Figure 3.6 (a), their distances cannot be inferred. In contrast, the COMPU-EYE system has enlarged, overlapping ommatidial receptive fields, because $\Delta\phi$ is much larger than $\Delta\phi$, as seen in Figure 3.6 (b). We note that a large acceptance angle can be realized by increasing the diameter of the photodetector, decreasing the focal length of the microlens, or using a material of higher refractive index for the microlens described in section 3.3.2. This configuration is shown in Figure 3.6 (b), in which object P_2 is observed by two ommatidia; thus, the compound eye can deduce that object P_2 is farther away

than object P_1 . When many ommatidia are present, the number of ommatidia viewing the object and the area of the object that is visible by the ommatidia depend upon the object distance. The variation of these quantities with object distance is used for depth estimation in the proposed method.

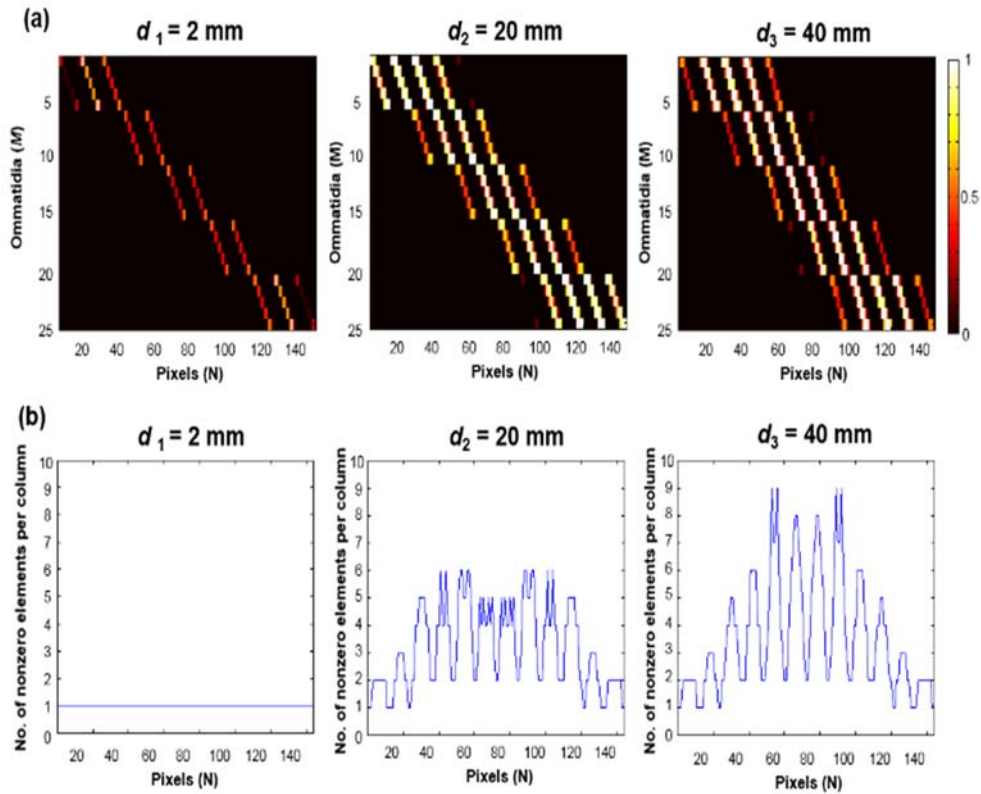


Figure 3.7 (a) Measurement matrices and (b) their number of nonzero elements per column for $d_1 = 2$ mm, $d_2 = 20$ mm, and $d_3 = 40$ mm, where $M = 5 \times 5$, $N = 12 \times 12$, $\Delta\phi = 12^\circ$, and $\Delta\varphi = 30^\circ$.

Here, we give an example of the variation for different object distances. In Figure 3.7, the

measurement matrices and corresponding number of nonzero elements per column are shown, in which a compound eye consists of 5×5 ommatidia with a radius of 6.92 mm, focal length of micro lens of 1.35 mm, $\Delta\phi = 12^\circ$, and $\Delta\varphi = 30^\circ$. Three objects are located at $d_1 = 2$ mm, $d_2 = 20$ mm, and $d_3 = 40$ mm from the compound eye. The object plane is composed of 12×12 pixels with a uniform distribution. As the object moves away from the compound eye, the areas of the ommatidial receptive fields and the overlap between them both increase. Accordingly, as shown in Figure 3.7 (a), the number of nonzero elements in the measurement matrix increases with object distance. In Figure 3.7 (b), the number of nonzero elements per column in the measurement matrices varies with respect to the object distances, implying that each pixel is uniquely observed by a different set of ommatidia with different perspectives. Thus, a unique measurement matrix is generated with respect to object distance. By using the relationship between the unique measurement matrix and the object distance, we propose the following method for estimating object distances.

3.4.1.2 System model for depth estimation

First, we set the range of interest $R = [d_{min}, d_{max}]$, where d_{min} and d_{max} are the minimum and maximum distances, respectively. The range of interest can be application-specific; for example,

it can be 10–25 mm for endoscopic applications [78]. For DSP, we assume that the object distance can be sampled as a set of discrete distances $\mathbf{d} = \{d_1, d_2, \dots, d_L\}$ within the range of interest, where L is the number of distance elements. In this paper, we consider uniform discrete distances within the range of interest. The depth resolution $\Delta d = (d_{\max} - d_{\min}) / L$ depends on the number of distance elements and depth range of interest. According to the predetermined \mathbf{d} , a measurement matrix \mathbf{A}_{d_l} for $l \in \{1, 2, \dots, L\}$ can be obtained from the structure of the compound eye and the object located a distance d_l away from the compound eye. By concatenating L measurement matrices, a dictionary matrix $\mathbf{D} \in \mathbb{R}^{M \times (L \cdot N)}$ can be formed as $\mathbf{D} = [\mathbf{A}_{d_1} \ \mathbf{A}_{d_2} \ \dots \ \mathbf{A}_{d_L}]$. Then, the linear representation of \mathbf{y} in (9) can be rewritten in terms of all possible measurement matrices as

$$\mathbf{y} = \sum_{i=1}^L \mathbf{A}_{d_i} \mathbf{x}_i = \mathbf{D} \mathbf{u}, \quad (10)$$

where $\mathbf{u} = [\mathbf{x}_1^T, \dots, \mathbf{x}_L^T]^T = [x_{1,1}, \dots, x_{1,N}, \dots, x_{L,1}, \dots, x_{L,N}]^T \in \mathbb{R}^{(L \cdot N) \times 1}$. When an object is located at a certain distance in the set \mathbf{d} , a valid observation \mathbf{y} can be sufficiently represented by a linear combination of the columns from the corresponding measurement matrix. For example, when the object distance matches the l^{th} measurement matrix, the linear equation becomes

$$\mathbf{y} = \mathbf{D} \mathbf{u}_0, \quad (11)$$

where $\mathbf{u}_0 = [0, \dots, 0, x_{l,1}, \dots, x_{l,N}, 0, \dots, 0]^T$ is a sparse coefficient vector whose entries are zero

except for those associated with the l^{th} measurement matrix. \mathbf{x} can be sparsely represented as

$\mathbf{x} = \mathbf{W}^T \mathbf{s}$. Similarly, \mathbf{u} can be sparsely represented as $\mathbf{u} = \mathbf{B}^T \mathbf{v}$. Here, \mathbf{v} is an $L \cdot N \times 1$ sparse

vector and \mathbf{B} is a block diagonal matrix containing L instances of \mathbf{W} , that is,

$\mathbf{B} = \underbrace{\text{diag}(\mathbf{W}, \dots, \mathbf{W})}_L \in \mathbb{R}^{(L \cdot N) \times (L \cdot N)}$, where $\text{diag}(\cdot)$ represents a diagonal matrix. By using \mathbf{v} , (10)

becomes

$$\mathbf{y} = \mathbf{DB}^T \mathbf{v}, \quad (12)$$

where $\mathbf{v} = [\mathbf{s}_1^T, \dots, \mathbf{s}_L^T]^T = [s_{1,1}, \dots, s_{1,N}, \dots, s_{L,1}, \dots, s_{L,N}]^T \in \mathbb{R}^{(L \cdot N) \times 1}$. As does (8), l_1 norm

minimization provides a sparse vector $\hat{\mathbf{v}}$:

$$\hat{\mathbf{v}} = \arg \min_{\mathbf{v}} \|\mathbf{v}\|_1 \quad \text{subject to} \quad \|\mathbf{y} - \mathbf{DB}^T \mathbf{v}\| \leq \eta, \quad (13)$$

where η is a small constant.

3.4.2 Depth estimation method

After $\hat{\mathbf{v}}$ has been obtained from (13), the problem of estimating object distances can be reformulated as a classification problem whose objective is to find the distances at which the object has the highest probability of being located. Because the compound eye imaging system can be sparsely represented in (12) and the measurement matrices are uniquely generated with respect to object distances, sparse-representation-based classification (SRC) can be used to

estimate object locations. SRC has been widely studied, and its accuracy has been demonstrated in many applications including face recognition [79] and brain computer interface systems [80]. SRC usually finds the most compact representation of a test sample, where the representation is expressed as a linear combination of columns in an overcomplete dictionary matrix, and then, it determines a class that contributes most to represent the test sample [81]. In this paper, we use SRC to estimate the depths of multiple objects. Unlike conventional SRC, the observed signal in this depth estimation framework is superposed with respect to the number of objects. Therefore, our problem is defined as a multiclass classification problem. We first describe an SRC-based depth estimation algorithm in the compound eye imaging system; we then propose an iterative depth estimation method that updates dictionaries in a coarse-to-fine manner.

We first specify a classification rule by using sparse signal reconstruction. As l_1 norm minimization provides a sparse solution for (7), most of the nonzero components in $\hat{\mathbf{S}}$ reside in the class in which the object exists with high probability. One of the classification rules is to use the residuals [82]. For each class, we define its characteristic function $\delta_l : \mathbb{R}^{L \cdot N} \rightarrow \mathbb{R}^{L \cdot N}$ that selects the coefficients of $\hat{\mathbf{v}}$ associated with the l^{th} class while nullifying the coefficients of other classes. Thus, for $\hat{\mathbf{v}} \in \mathbb{R}^{L \cdot N}$, $\delta(\hat{\mathbf{v}}) \in \mathbb{R}^{L \cdot N}$ is obtained by including the elements corresponding to the l^{th} class and nulling all elements of $\hat{\mathbf{v}}$ from other classes. By using the characteristic function, we denote the regularized residuals as

$$r_l := \|\mathbf{y} - \mathbf{D}\mathbf{B}^T \delta_l(\hat{\mathbf{v}})\|^2 / \|\delta_l(\hat{\mathbf{v}})\|^2. \quad (14)$$

If the object is located at d_l , the r_l value is smaller than those at other distances. We denote I_e as a set of the indices of estimated distances at which the objects are expected to be located.

With r_l for $l=1, \dots, L$, the classification rule is given by

$$I_e := \{l \mid r_l < \alpha\}, \quad (15)$$

where α is an arbitrary constant. A set of distances $\hat{\mathbf{d}}$ where the object is expected to be located can be determined by

$$\hat{\mathbf{d}} = \{d_l \mid l \in I_e\}. \quad (16)$$

Then, the images that only correspond to the estimated distances are reconstructed by solving

$\hat{\mathbf{x}}_l = \mathbf{W}^T \hat{\mathbf{s}}_l$ for $l \in I_e$. The SRC-based depth estimation algorithm is summarized in Table 1.

Table 1 SRC-based depth estimation algorithm

Initialization: $\mathbf{y}, \mathbf{d} = \{d_1, d_2, \dots, d_L\}, \mathbf{w}, \eta, \alpha$

Step 1: Set $\mathbf{D} = [\mathbf{A}_{d_1} \ \mathbf{A}_{d_2} \ \dots \ \mathbf{A}_{d_L}]$ and $\mathbf{B} = \text{diag}(\underbrace{\mathbf{W}, \dots, \mathbf{W}}_L)$.

Step 2: Solve (7) from \mathbf{y} given \mathbf{D} and \mathbf{B} , and obtain $\hat{\mathbf{v}}$.

Step 3: Calculate the regularized residuals:

$$r_l := \|\mathbf{y} - \mathbf{D}\mathbf{B}^T \delta_l(\hat{\mathbf{v}})\|^2 / \|\delta_l(\hat{\mathbf{v}})\|^2 \text{ for } l=1, \dots, L.$$

Step 4: Obtain the class of existence $I_e = \{l \mid r_l < \alpha\}$ and the estimated distance of the object $\hat{\mathbf{d}} = \{d_l \mid l \in I_e\}$.

Thus far, depth estimates have been obtained by finding locations in a dictionary, where the signals have small residuals. To improve the depth accuracy, the number of distance elements L must be increased in the form of the dictionary. However, the dictionary cannot include infinitely many possible distances owing to computational complexity and memory storage. To solve (13), $O(M \cdot N \cdot L)$ computations for every iteration and $O(M \cdot N \cdot L)$ storage are required; these are proportional to the number of distance elements [75]. We note that the l_1 norm minimization in (13) finds a sparse solution whose nonzero elements are most closely associated with the most correlated measurement matrix. By using the fact that the measurement matrices of neighboring distances are relatively more correlated than those of farther distances in dictionary matrix \mathbf{D} , we propose an iterative depth estimation method that is more efficient in terms of computational complexity and memory storage. Instead of universally searching for the object distances at once, we iteratively refine the set of distances in a coarse-to-fine manner [83]. The distances are investigated in detail only around regions where objects are expected to be present.

For iteration index i , we first choose a set of coarse distances within the range of interest $R^{(i)}$ as $\mathbf{d}_l^{(i)}$ for $l=1,2,\dots,L_i$, at which the objects can potentially be located. The depth interval is $\Delta d^{(i)} = d_{l+1}^{(i)} - d_l^{(i)}$. Accordingly, $\mathbf{D}^{(i)}$ and $\mathbf{B}^{(i)}$ can be generated from the structure of the compound eye imaging system. The sparse signal $\hat{\mathbf{v}}$ is reconstructed by solving (13), and the

estimate of distances $\hat{\mathbf{d}}^{(i)}$ can be obtained by solving (14)-(16). Then, the set of distances is updated by refining the range of interest and the depth interval. The range of interest is refined around the estimated distances, that is, $R^{(i+1)} = \left[\hat{d}_j^{(i)} - \Delta d^{(i)} / 2, \hat{d}_j^{(i)} + \Delta d^{(i)} / 2 \right]$ for $j=1, \dots, \left| \hat{\mathbf{d}}^{(i)} \right|$, where $|\cdot|$ represents the cardinality. The depth interval is refined as $\Delta d^{(i+1)} = \Delta d^{(i)} / K$ for a positive real number $K > 1$. Then, the updated set of finer distances is

$$\mathbf{d}^{(i+1)} = \left\{ \hat{d}_{j,k}^{(i+1)} \right\} \quad (17)$$

where $\hat{d}_{j,k}^{(i+1)} = \left(\hat{d}_j^{(i)} - \Delta d^{(i)} / 2 \right) + (k-1) \Delta d^{(i+1)}$ for $j=1, \dots, \left| \hat{\mathbf{d}}^{(i)} \right|$ and $k=1, \dots, \lceil K \rceil$. We repeat this process until the depth interval is sufficiently fine. The iterative coarse-to-fine depth estimation algorithm is summarized in Table 2.

Table 2. Iterative depth estimation algorithm

Initialization: $\mathbf{y}, R^{(1)}, \mathbf{d}^{(1)} = \{d_1^{(1)}, d_2^{(1)}, \dots, d_{L_1}^{(1)}\}, \mathbf{W}, \eta, \alpha, l=1$

Step 1: Set $\mathbf{D}^{(i)} = \left[\mathbf{A}_{d_1^{(i)}} \cdots \mathbf{A}_{d_{L_i}^{(i)}} \right]$ and $\mathbf{B}^{(i)} = \text{diag}(\underbrace{\mathbf{W}, \dots, \mathbf{W}}_{L_i})$.

Step 2: Solve (13) from \mathbf{y} given $\mathbf{A}^{(i)}$ and \mathbf{B} , and obtain $\hat{\mathbf{v}}$.

Step 3: Calculate the regularized residuals:

$$r_l := \|\mathbf{y} - \mathbf{D}\mathbf{B}^T \delta_l(\hat{\mathbf{v}})\|^2 / \|\delta_l(\hat{\mathbf{v}})\|^2 \quad \text{for } l=1, \dots, L_i.$$

Step 4: Obtain the set of indices of estimated distances $I_e^{(i)} = \{l \mid r_l < \alpha_l\}$.

Step 5: Update

$$R^{(i+1)} = \left[\hat{d}_j^{(i)} - \Delta d^{(i)} / 2, \hat{d}_j^{(i)} + \Delta d^{(i)} / 2 \right] \quad \text{for } j=1, \dots, \left| \hat{\mathbf{d}}^{(i)} \right|,$$

$$\Delta d^{(i+1)} = \Delta d^{(i)} / K \quad \text{for } K > 1, \quad \mathbf{d}^{(i+1)} = \left\{ \hat{d}_{j,k}^{(i+1)} \right\} \quad \text{and } L_{i+1} = \left| \mathbf{d}^{(i+1)} \right|,$$

$$\text{where } \hat{d}_{j,k}^{(i+1)} = \left(\hat{d}_j^{(i)} - \Delta d^{(i)} / 2 \right) + (k-1) \Delta d^{(i+1)}$$

$$\text{for } j=1, \dots, \left| \hat{\mathbf{d}}^{(i)} \right| \quad \text{and } k=1, \dots, \lceil K \rceil.$$

Step 6: Set $i = i+1$ and repeat from Step 1 until the depth resolution is sufficiently fine.

3.5 Simulation results

3.5.1 Simulation setups

To evaluate the performance of our design, we consider a hemispherical compound eye with a radius of $R = 6.9216$ mm, where each ommatidium has a height of $f = 1.35$ mm in Figure 3.2 (b).

The compound eye consists of a varying number M of ommatidia of uniform spacing with the interommatidial angle $\Delta\phi = 180/\sqrt{M}^\circ$. The object image to be reconstructed is composed of $N =$

160 × 160 pixels. As a sparsity measure of the image, we use the sparsity ratio defined as a ratio of the number of nonzero elements to the total length of the signal. For the sparsifying basis \mathbf{w} , we use a db2 wavelet transform and a level of two. To solve (7), we use the fast and efficient alternating direction method [84].

3.5.2 Simulation results on resolution improvements

We demonstrate the performance of COMPU-EYE with an image in the presence of noise. The object image is a line-art illustration of a tiger, which consists of 160 × 160 pixels each of which contains an 8-bit quantized light intensity. The sparsity ratio of the tiger image is $\text{SR} = 0.2335$. The conventional compound eye consists of $M = 80 \times 80$ ommatidia with $\Delta\phi = \Delta\varphi = 2.25^\circ$. On the other hand, COMPU-EYE consists of $M = 80 \times 80$ ommatidia of much larger acceptance angles, $\Delta\phi = 60^\circ$ than $\Delta\phi = 2.25^\circ$. The object image size of 60 × 60 mm is at a distance of 10mm from the compound eyes. An additive observation noise in (7) is assumed to be Gaussian with zero mean and covariance matrix $\sigma^2 \mathbf{I}_M$ where $\sigma^2 = 0.1$.

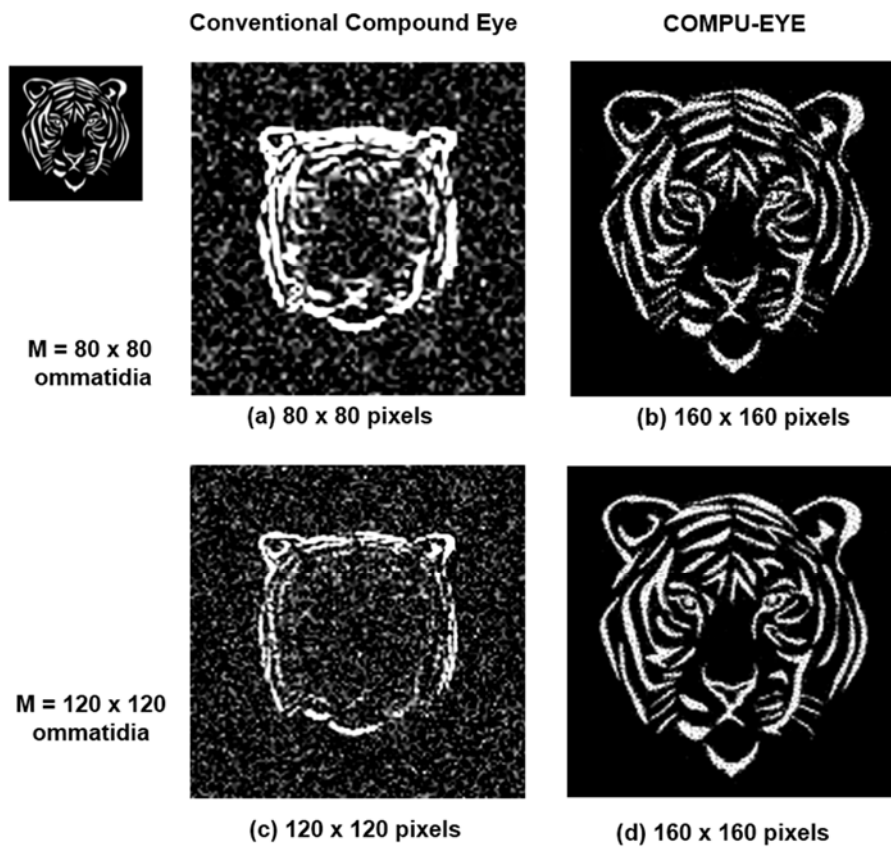


Figure 3.8 For $M = 80 \times 80$ and $\Delta\phi = 2.25^\circ$, (a) Output image of the conventional compound eye with $\Delta\phi = 2.25^\circ$ (b) Image recovered by COMPU-EYE with $\Delta\phi = 60^\circ$. For $M = 120 \times 120$ and $\Delta\phi = 1.5^\circ$. (c) Output image of the conventional compound eye with $\Delta\phi = 1.5^\circ$ (d) Image recovered by COMPU-EYE with $\Delta\phi = 60^\circ$.

Figure 3.8 (a) shows the output image of the conventional compound eye. The output image is corrupted by noise. Because of the resolution limit determined by M and undetectable areas in the ommatidial receptive fields, the observed image of the conventional compound eye is poor quality.

Figure 3.8 (b) shows the image recovered by COMPU-EYE equipped with the DSP technique.

Compared to the Figure 3.8 (a), COMPU-EYE provides a higher resolution imaging as well as denoising effects. Due to the stability of the l_1 norm minimization, the unexpected noise is efficiently removed in the reconstructed image without any denoising algorithm. When the number of ommatidia is increased to $M = 120 \times 120$ with $\Delta\phi = 1.5^\circ$, the output image of the conventional compound eye and the recovered image of COMPU-EYE are shown in Figure 3.8 (c) and (d), respectively. As we increase the number of ommatidia, the object image is more clearly seen. For a measure of the resolution improvement, we define a *pixel resolution* as the total number of pixels to be reconstructed with $\text{NMSE} < \delta$, where $\delta > 0$ is a user-defined positive number. Since the number of pixels to be recovered is increased from 80^2 to 160^2 in Figure 3.8 (b) and from 120^2 to 160^2 in Figure 3.8 (d), the gain in the pixel resolution is 4 and 1.78, respectively. We note that the size of the observed image in a conventional compound eye is smaller than that of the recovered image of the proposed eye; this is because the ommatidia on the edge of a conventional compound eye are unable to detect the object image owing to their small range of acceptance angle.

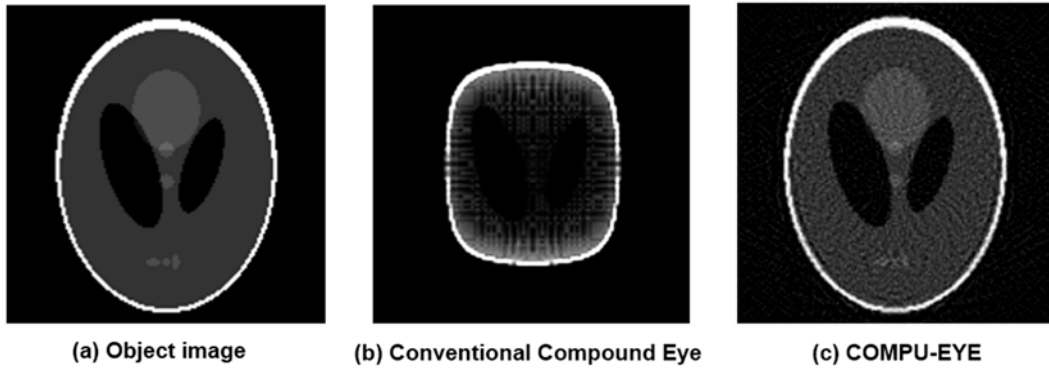


Figure 3.9 For the compound eyes, $M = 120 \times 120$ and $\Delta\phi = 1.5^\circ$. (a) Object image of 8-bit grayscale image with 160×160 pixels (b) Output image of the conventional compound eye with $\Delta\phi = 1.5^\circ$ and. (c) Image recovered by COMPU-EYE with $\Delta\phi = 60^\circ$.

We now investigate the performance of COMPU-EYE with a non-sparse phantom image which is used in image processing [85]. The phantom image in Figure 3.9 (a) consists of 160×160 pixels, each of which contains an 8-bit intensity of light. SR of the phantom image is 0.4928. The number of ommatidia is set to be 120×120 with $\Delta\phi = 1.5^\circ$ and $\Delta\phi = 1.5^\circ$ for the conventional compound eye and $\Delta\phi = 60^\circ$ and $\Delta\phi = 1.5^\circ$ for COMPU-EYE. The object image size of 60×60 mm is at a distance of 10 mm from the compound eyes. In the reconstruction of the image, DCT is used for a sparsifying basis. As seen in Figure 3.9 (b), the direct observation of the conventional compound eye provides poor resolution and the object is distorted. Figure 3.9 (c) shows the reconstructed image by COMPU-EYE. The resolution is improved by a factor of $N/M = 1.78$. We note that the distortion comes from a discrepancy in receptive fields of ommatidia, i.e., as an

ommatidium is closely located to the edge of the compound eye, its corresponding receptive field becomes larger. In contrast, the reconstructed image of COMPU-EYE in Figure 3.9 (c) is not distorted because COMPU-EYE recovers the designated pixel values \mathbf{x} in the object. As a result, COMPU-EYE can also reconstruct the non-sparse object image with a high resolution.

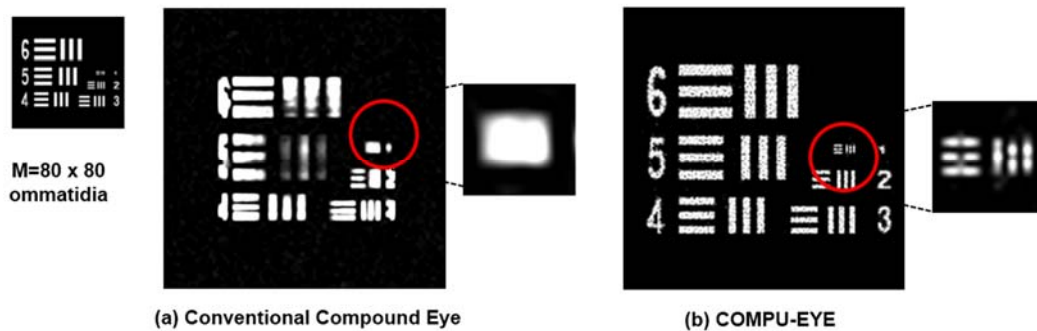


Figure 3.10 Resolution test: (a) Conventional compound eye consisting of 80×80 ommatidia with $\Delta\varphi = \Delta\phi = 2.25^\circ$. (b) COMPU-EYE consisting of 80×80 ommatidia with $\Delta\varphi = 60^\circ$ and $\Delta\phi = 2.25^\circ$.

Figure 3.10 illustrates optical resolution tests of the conventional compound eye and COMPU-EYE. The 60×60 mm object image at a distance of 10 mm is composed of 160×160 pixels. The object image is a target image similar to the US Air Force (USAF) test, where the minimum spacing of gratings is a single pixel, i.e., 0.375 mm. The lines of the row labeled “1” have single pixel spacing, those of the row labeled “2” have two-pixel spacing, and so on. Both compound

eyes are composed of 80×80 ommatidia with $\Delta\phi = 2.25^\circ$ and $\Delta\phi = 2.25^\circ$ for the conventional compound eye and with $\Delta\phi = 2.25^\circ$ and $\Delta\phi = 60^\circ$ for COMPU-EYE. Because the achievable optical resolution of the conventional 80×80 compound eye with $\Delta\phi = \Delta\phi = 2.25^\circ$ is 0.7179×0.7179 mm, which is obtained from the distance of resolvable gratings in the object plane, it cannot distinguish the smallest grating as shown in Figure 3.10 (a). However, COMPU-EYE can sharply resolve the smallest grating because the resolvable resolution is the unit of a single pixel. Thus, the achievable minimum optical resolution of COMPU-EYE is 0.375×0.375 mm, an improvement in resolution of about 3.66 times. We note that the observation at the center of the conventional compound eye in Figure 3.10 (a) suffers from lack of incoming light due to the relatively small sized receptive fields and its resulting undetectable area.

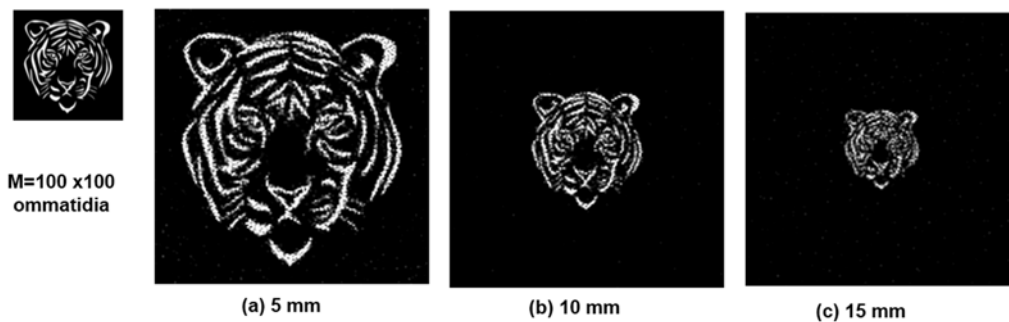


Figure 3.11 Depth test: Image recovered by COMPU-EYE consisting of 100×100 ommatidia with $\Delta\phi = 60^\circ$ and $\Delta\phi = 1.8^\circ$, where the dimension of the final object image is (a) 30×30 mm at 5 mm, (b) 60×60 mm at 10 mm, (c) 90×90 mm at 15 mm. The actual tiger picture is 30×30 mm.

Figure 3.11 shows the image recovered by the proposed COMPU-EYE at various object image distances. The size of the visible area of the compound eye is proportional to the distance of the object image, and the measurement matrices are generated according to the distances of the object image. Given the measurement matrices at distances of 5, 10, and 15 mm, the image can be reconstructed from \mathbf{y} . As seen in Figure 3.11, the recovered images are still clear and focus is maintained as the object image moves away from the compound eye.

3.5.3 Simulation results on depth estimation

First, we determine the depth estimation accuracy for the proposed compound eye. Because the measurement matrices corresponding to neighboring distances are more correlated with each other, we set a distance of 108 mm from the compound eye as the reference distance and compare with other distances by increasing the depth intervals. To evaluate the depth estimation accuracy with respect to the depth interval, we consider a sparse signal as an input, that is, $\mathbf{W} = \mathbf{I}$, where \mathbf{I} represents an identity matrix. In each assessment, a sparse signal dimension of 10000×1 with 5%, 7.5%, and 10% of randomly located nonzero elements is used. The distance of the input signal is randomly chosen between the reference distance and the comparison distance. The

tolerance α in (15) is set to be 0.1. This assessment is repeated 100 times. As seen in Figure 3.12, as the object distances increase, the accuracy of the proposed depth estimation increases. For signals with 5% sparsity, if the depth intervals are larger than 0.3 mm, the proposed depth estimation works with more than 97% accuracy. For the l_1 norm minimization in (13), the reconstruction performance depends on the sparsity of the input signal, that is, low accuracy for the input signal with large sparsity. Thus, as the sparsity increases, the performance of the proposed depth estimation deteriorates as well.

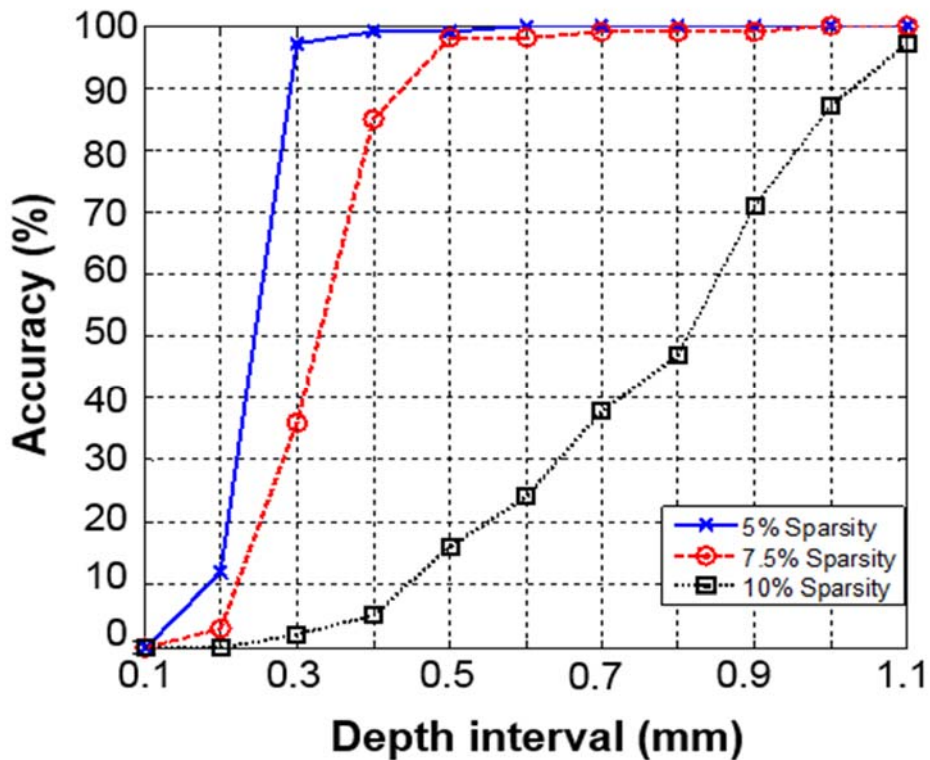


Figure 3.12 Depth estimation accuracy (%) with respect to depth interval.

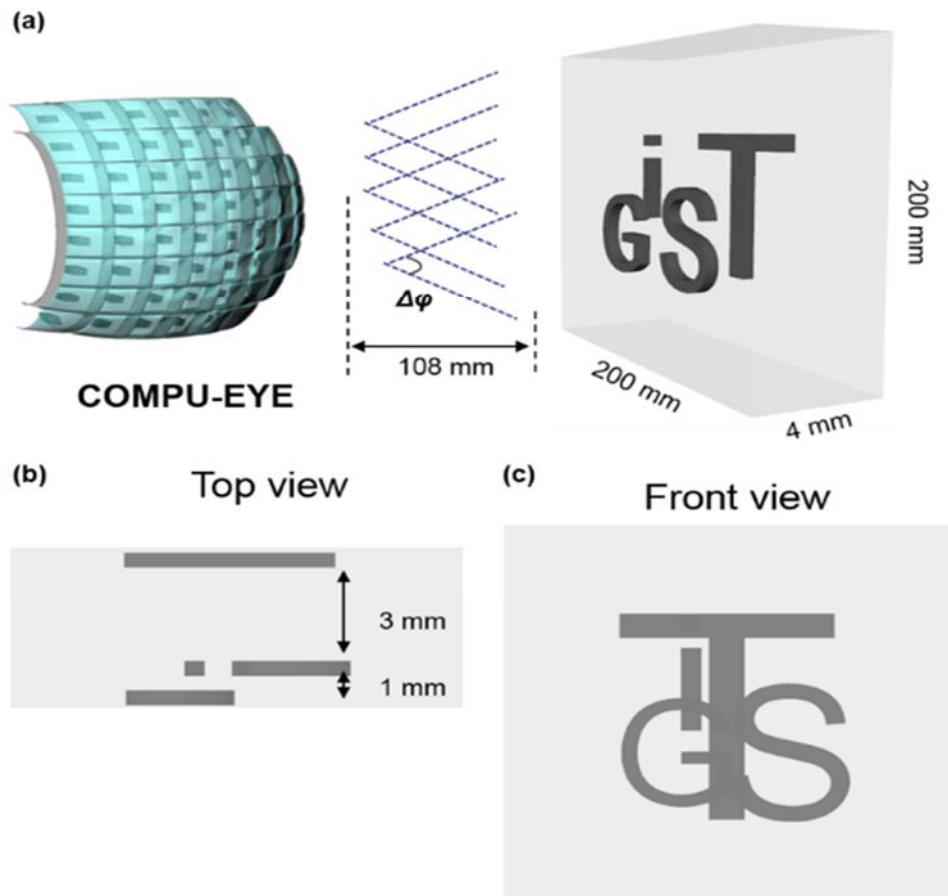


Figure 3.13 Proposed COMPU-EYE imaging system: (a) three-dimensional, (b) top, and (c) front views.

The proposed COMPU-EYE imaging system used for evaluating the image reconstruction is shown in Figure 3.13. The hemispherical compound eye observes an object consisting of four characters: G, i, S, and T. The characters are located at three different distances from the compound eye. G is 108 mm away from the compound eye, i and S are 109 mm away, and T is 112 mm away, as shown in Figure 3.13 (b). As shown in Figure 3.13 (c), the characters overlap

one another, preventing the distance information from being inferred. The DSP technique introduced in Section 3 can be used to decompose each letter given its distance.

We demonstrate the performance of the proposed depth estimation method when the object distances are included in the set of potential distances in the dictionary. We assume that the depth range of interest is from 108 mm to 112 mm and the target depth resolution is 1 mm. Within the range of interest, the distances are uniformly sampled with 1-mm resolution, that is, $\mathbf{d} = \{108, 109, 110, 111, 112\}$. For depth estimation and object reconstruction, we construct a dictionary matrix $\mathbf{D} = [\mathbf{A}_{108} \ \mathbf{A}_{109} \ \mathbf{A}_{110} \ \mathbf{A}_{111} \ \mathbf{A}_{112}]$ in accordance with the potential distances. Given \mathbf{A} , we can solve (13) to obtain $\hat{\mathbf{S}}$ from \mathbf{y} . Then, $\hat{\mathbf{u}}$ can be obtained by calculating $\hat{\mathbf{u}} = \mathbf{W}^T \hat{\mathbf{v}}$. The reconstructed $\hat{\mathbf{v}}$ and $\hat{\mathbf{u}}$ are shown in Figure 3.14 (a) and Figure 3.14 (b), respectively. Owing to the sparse signal reconstruction, most of the nonzero signals in Figure 3.14 (a) are concentrated in the set of indices corresponding to distances of 108 mm, 109 mm, and 112 mm. We note that the reconstruction errors in Figure 3.14 (a) and Figure 3.14 (b) for 110 mm and 111 mm are caused by coherence among neighboring measurement matrices. As indicated in Figure 3.14 (c), the regularized residuals of the set of indices corresponding to distances of 108 mm, 109 mm, and 112 mm are smaller than those corresponding to the other distances. As a result, the index set of the estimated distances and the estimated distances of the objects are determined as $I_e = \{1, 2, 5\}$ and $\hat{\mathbf{d}} = \{108, 109, 112\}$, respectively. In Figure 3.14 (d), the reconstructed

signals $\hat{\mathbf{x}}_l = \mathbf{W}^T \hat{\mathbf{s}}_l$ for $l \in \{1, 2, 5\}$ are represented as images. Note that the observation is highly distorted owing to the overlap among the ommatidial receptive fields. The reconstructed characters at 108, 109, and 112 mm are clearly visible. This result indicates that COMPU-EYE achieves 1-mm depth resolution. We note that the reconstruction resolution is also improved by 1.56 times because 100×100 -pixel images are reconstructed from 80×80 -pixel ommatidial observations.

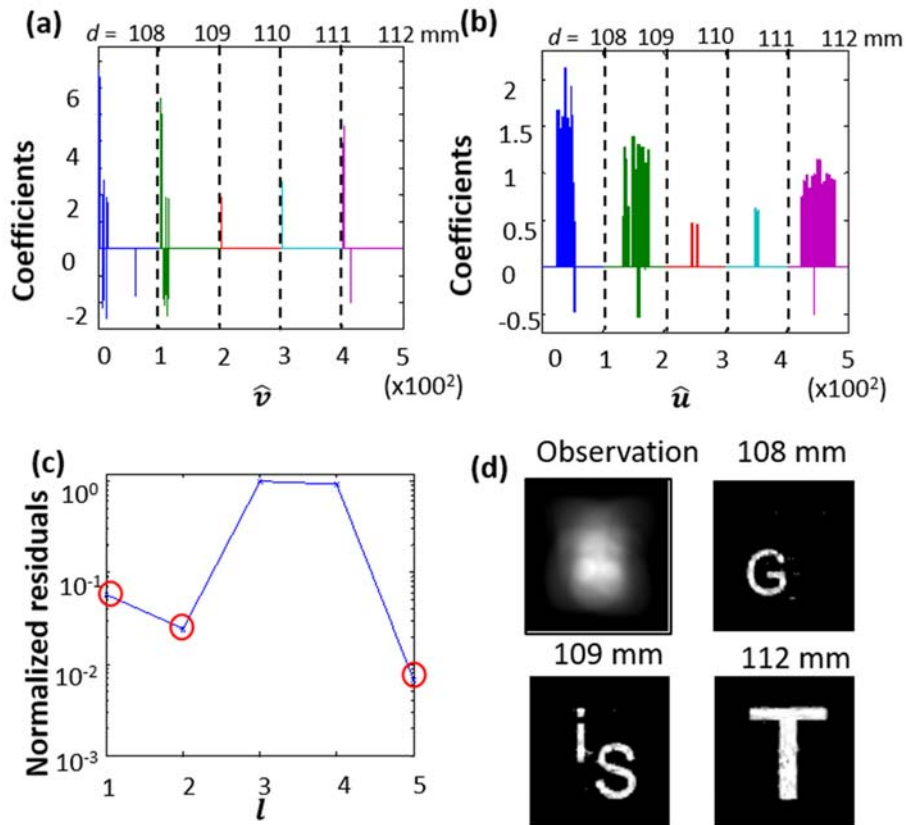


Figure 3.14 (a) Reconstruction of $\hat{\mathbf{v}}$, (b) reconstruction of $\hat{\mathbf{u}}$, (c) normalized regularized residuals, and (d) ommatidial observations and reconstructed images with respect to estimated distances.

We now investigate the performance of the iterative depth estimation for the object shown in Figure 3.15. We assume that the potential object locations are unknown and that the range of interest is from 100 mm to 120 mm, that is, $R^{(1)} = [100 \text{ mm}, 120 \text{ mm}]$. For the SRC-based depth estimation method in Table 1 to achieve a depth resolution of 1 mm, the dictionary requires 21 concatenated measurement matrices with dimensions of 6400×210000 . The computational complexity of this task necessitates the use of the iterative depth estimation method described in Table 2. We first formulate a set of coarse distances $\mathbf{d}^{(1)} = \{100, 110, 120\}$ and $\mathbf{D} = [\mathbf{A}_{100} \ \mathbf{A}_{110} \ \mathbf{A}_{120}]$ correspondingly. The result of iterative depth estimation is shown in Figure 3.15. At the 1st iteration, because the objects are located at around 110 mm, the residual value at 110 mm is the smallest. Thus, the object distance is estimated as 110 mm for $\alpha = 0.3$ at the 1st iteration. For detailed depth estimation, we further set a dictionary with finer distances at around 110 mm. The range of interest is refined as $R^{(2)} = [105, 115]$ and the depth interval, as $\Delta d^{(2)} = 3$ for $K = 3.33$. Then, the set of distances is updated as $\mathbf{d}^{(2)} = \{105, 108, 111, 114\}$. At the 2nd iteration, the residual values at distances of 108 mm and 111 mm are smaller than those at other distances. Thus, we estimate that the objects are located at around 108 mm and 111 mm for $\alpha = 0.2$. The range of interest is refined as $R^{(3)} = [107, 109] \cup [110, 112]$ and the depth interval, as $\Delta d^{(3)} = 1$ for $K = 3$. Then, the set of distances is updated as $\mathbf{d}^{(3)} = \{107, 108, 109, 110, 111, 112\}$. At the 3rd iteration, the object distances are estimated as 108 mm, 109 mm, and 112 mm from the

compound eye for $\alpha = 0.1$. As a result, the objects are efficiently reconstructed by using the proposed iterative depth estimation method.

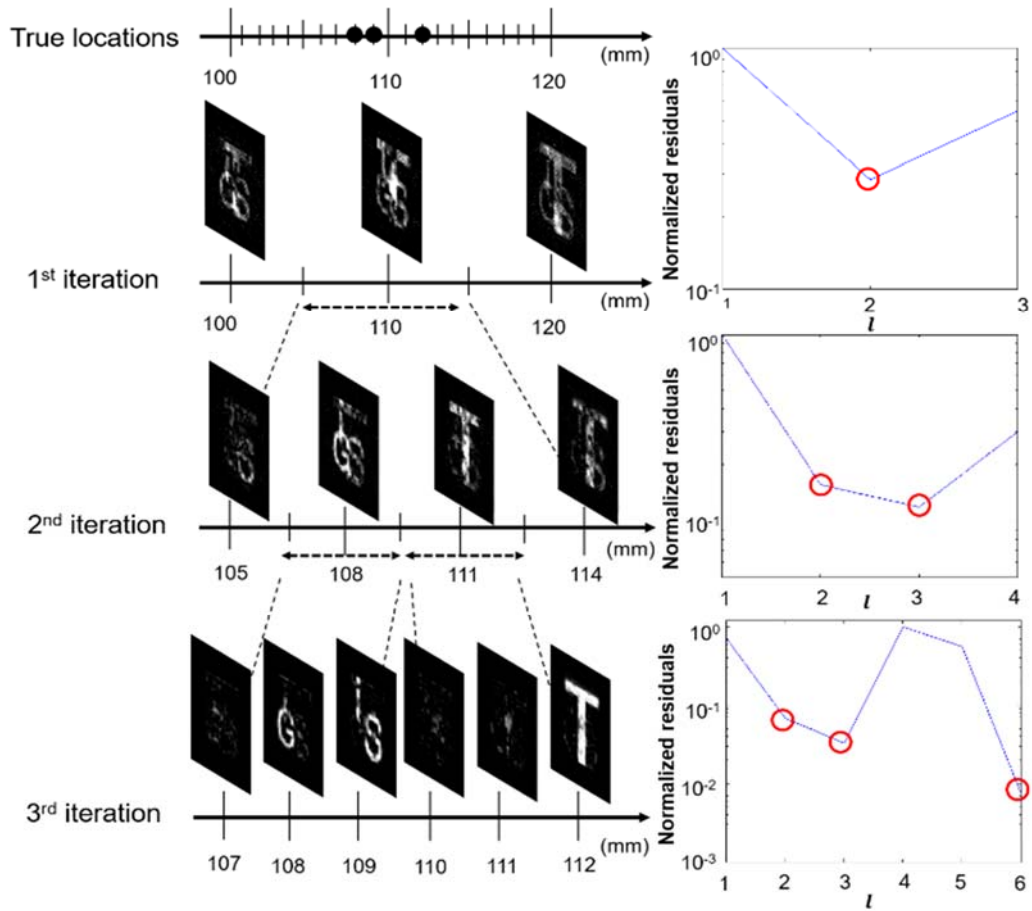


Figure 3.15 An example of the iterative depth estimation method.

Now, we aim to demonstrate depth estimation for an object with continuous depths. As a target, we consider a plane object that is slanted at 23° toward the compound eye and located 108 mm away from the compound eye. When the range of interest is from 108 mm to 111 mm, the object

distance can be uniformly sampled as $\mathbf{d} = \{108, 109, 110, 111\}$ in Figure 3.16 (b). The proposed depth estimation method provides a depth map of the object with 1-mm depth resolution, as shown in Figure 3.16 (d). Consequently, an object with continuous depths can be well reconstructed by using the estimated distances, as seen in Figure 3.16 (c). In this manner, continuous depths can be estimated. We note that if we densely sample the range of distance, the depth map will be more accurate; however, there is a limit to the depth resolution, as seen in Figure 3.12.

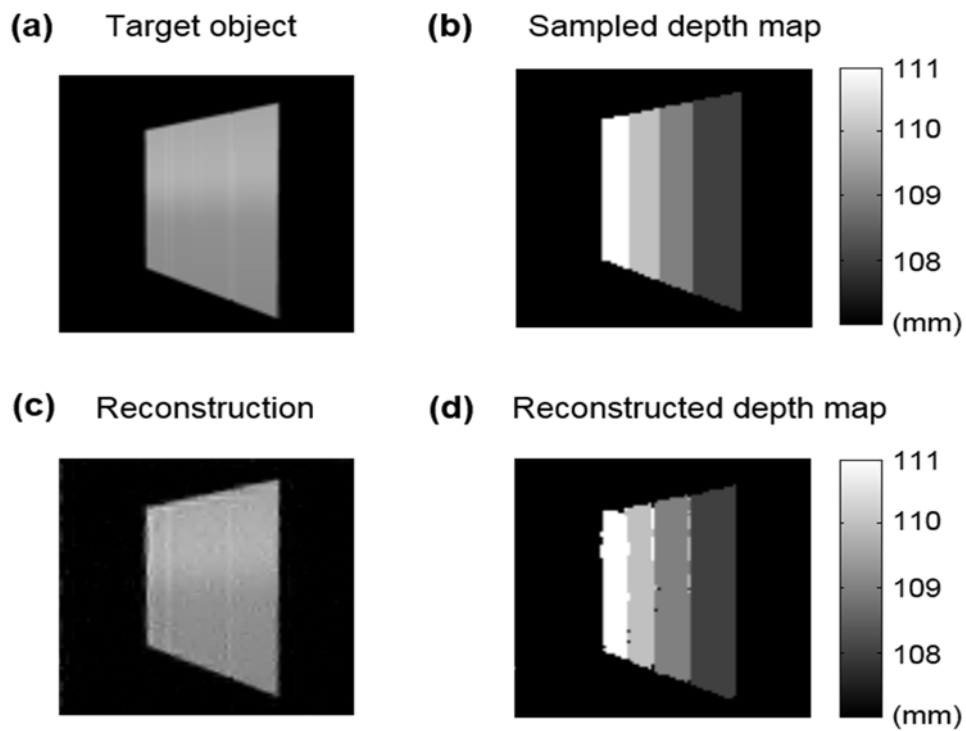


Figure 3.16 Depth estimation and object reconstruction for a slanted object.

3.6 Summary

We proposed the COMPU-EYE imaging system to improve the resolution of compound eyes. COMPU-EYE uses ommatidia with acceptance angles that are larger than the interommatidial angle as well as a DSP technique. By increasing the acceptance angles, each ommatidium covers wider areas, and each observation is different from the others because of its receptive field. Finer details can be resolved by the DSP technique. As a result, the proposed COMPU-EYE provides at least a four-fold improvement in resolution.

Natural compound eyes have the ability to detect high-speed motion owing to the simple ON/OFF detection structure of the ommatidium. In contrast, COMPU-EYE views the object only through computation and it necessarily requires certain computation time and cost for imaging. The computation requires solving a convex optimization problem; this problem can be solved in polynomial time by many state-of-the-art algorithms including YALL1 [75], FISTA [73], and CP [74]. Thus, the additional computation time required for the compound eyes is practically feasible with modern DSP devices. For example, when we measure the computation time using MATLAB with a 3.6-GHz Intel i7 processor, it takes 47 ms to recover $N = 256$ pixels from $M = 64$, as shown in Figure 3.10 (b). We note that the computation time can be reduced by using a multicore

processor or graphic processing unit because the algorithms [73-75] conduct matrix multiplications and additions, and these operations can be computed in parallel [86].

Generally, the acceptance angles are proportional to the light sensitivity of ommatidia. But, the large acceptance angles cause overlapping among neighboring ommatidia and necessarily result in low spatial resolution. By resolving the aliasing caused by the overlapping using a DSP technique, COMPU-EYE is expected to have high sensitivity with high resolution. Moreover, the technique for resolution improvements used in COMPU-EYE can be applied to other designs of artificial compound eyes. It would be interesting to compare resolution of Curvace design in [37] consisting of more ommatidia and the hemispherical compound eye in [27] consisting of less ommatidia but equipped with the DSP technique.

In this study, we have focused on the apposition compound eye. But, we note that the concept of COMPU-EYE can also be applied to other types of compound eyes, i.e., superposition compound eyes. For example, in the neural superposition compound eyes which are specialized for light sensitivity, each object point is imaged by multiple photoreceptors from different ommatidia and the related signals are combined to form an image with high sensitivity and high resolution [41]. By applying the design concept of larger acceptance angles and the DSP technique, the neural superposition compound eyes can improve the resolution and sensitivity.

In the real implementation of compound eye devices, COMPU-EYE is more efficient in terms of multiple observations. If some ommatidia are disjointed or damaged, the conventional compound eye could lose vision in the corresponding area. However, in COMPU-EYE, each area is observed by multiple ommatidia. Thus, even though some ommatidia are lost, they do not have a significant influence on the overall observation.

We have also proposed a depth estimation method based on the COMPU-EYE imaging system. Due to the large acceptance angles, the ommatidial receptive fields overlap, and the disparities between ommatidial observations vary with object distance. As a result, the uniqueness of the generated measurement matrix depends upon the object distance. In the proposed technique, the dependences of the disparities between the ommatidial observations and the measurement matrix uniqueness on object distance are used to estimate the depth. This work helps not only to estimate object distances but also to reconstruct objects with high resolution, and it is therefore essential for future development of the COMPU-EYE system.

Generally, disparity-based depth estimation methods have limitations for very distant objects because the disparities decrease [87]. By varying the acceptance angles of the ommatidia or arranging the ommatidia irregularly, the range of depth estimation can be extended adaptively, that is, large acceptance angles for small distances and small acceptance angles for large distances [88].

The analysis of the measurement matrix remains as an open problem. The measurement matrix depends on the acceptance angles of ommatidia, object distances, and structure of the compound eyes. From the analysis, we may answer those questions: ‘What is the achievable spatial or depth resolution given design parameters such as the acceptance angles and the structure of the compound eye?’, ‘What is the optimal design parameters in order to achieve certain spatial or depth resolution?’, ‘What is the relationship between the design parameters and the range of depth estimation?’, or ‘Is irregularity of acceptance angles or deployment of ommatidia helpful?’. For the analysis, techniques used in the analysis of the regular and irregular low-density parity check (LDPC) codes might be used. Furthermore, the l_0 -norm based minimization can be used to solve (7). This has been shown to provide better reconstruction performance than the l_1 -norm minimization [89].

4 COMPRESSIVE SPECTROMETERS

A spectrometer is an optical instrument that breaks light scattered from an object into various colors (wavelengths) and record them as a function of wavelength. Since the light from the object contains its spectral signature, the composition of the object can be figured out by the spectral analysis. The spectrometers, which are commonly huge and heavy, are miniaturized using nano optics/materials technology and are available for the commercial use but with a limited resolution. By employing the CS framework, we propose a compressive spectrometer integrated with analog compressive samplers and a DSP algorithm to improve spectral resolution. Conventional filter-based spectrometers uniformly sample the incoming light in the spectral domain by bandpass filters that only pass the light only within the designated spectral band. In contrast, the compressive spectrometer compressively samples the holistic information of the light. The design of analog samplers is based on the thin-film filter technology. Compressive sampling is achieved by making the transmittance of the filters as random. The resolution improvement is achieved by using the DSP algorithm developed for the spectrometers. Furthermore, in the compressive spectrometer, we propose an incident angle estimation algorithm to resolve the measurement matrix mismatch problem caused by the variation of the incident angle.

4.1 Introduction

Spectrometers are key instruments used to separate and measure spectral components of light reflected from or transmitted through the object. The spectrum is then analyzed to provide fine details about the objects. These instruments are usually huge, heavy in weight, expensive machines that are often owned by institutions and require training to use. But, thanks to the recent nano-optics technology, spectrometers are being miniaturized that brings portability and cost-effectiveness [90]. Miniature spectrometers are favored for everyday consumer applications such as bio-medical, chemical and environmental engineering [91, 92].

To find the spectrum of the light, the spectrometers break light into various colors (wavelengths) and record them. According to the underlying operation principle, spectrometers can be classified as grating-based, Fourier-transform-based, and filter-based spectrometers [90]. The splitting is typically done by diffraction gratings in Figure 4.1 (a). While grating-based spectrometers offer high resolution capability, they require not only complex and precise optical arrangements to focus and process the light, but also long focal length for high resolution. When one tries to downsize the spectrometer for portability, the resolution is remarkably decreased. Despite these demerits, grating-based spectrometers remain popular for laboratory and research purposes. Recently, a lot of attempts is to use an optical filter array instead of gratings in Figure 4.1 (b).

Each filter in the array is carefully designed to transmit only a certain color and block the other colors, a typical brick-wall design. With the introduction of filters, the optical focusing units are eliminated and the challenge moves to a mini filter design via optical-nano materials and fabrication technology.

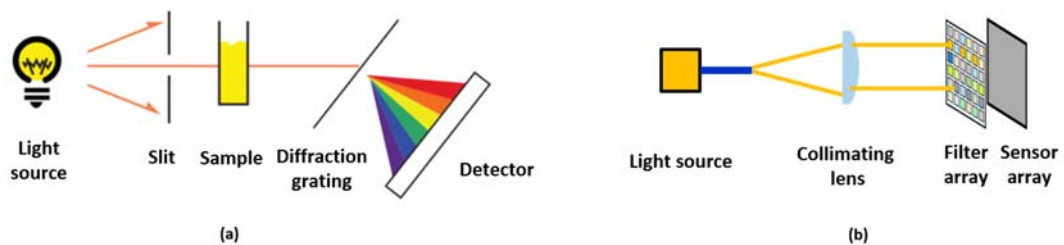


Figure 4.1 (a) Grating-based spectrometer, (b) filter-array-based spectrometer.

4.1.1 Resolution limits of the filter-based miniature spectrometers

In the filter-array-based spectrometers, resolution which represents the ability how closely resolve two neighboring spectra, is determined by the number of filters and their transmittance functions [6].

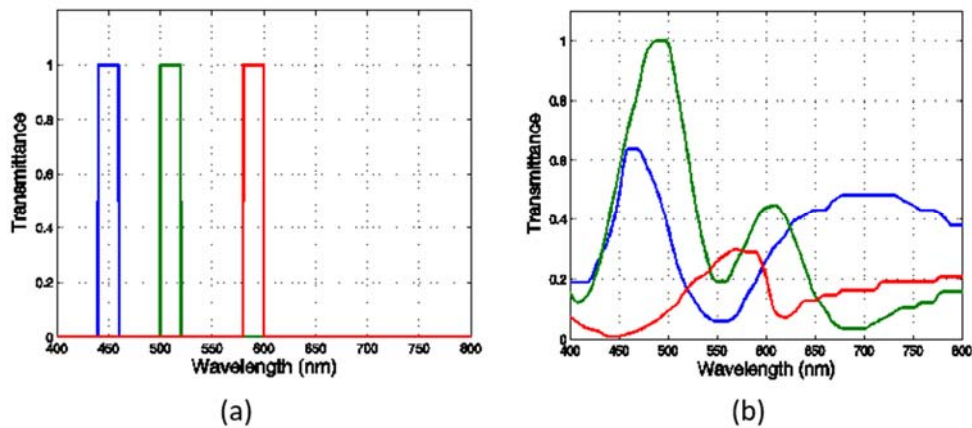


Figure 4.2 Transmittance functions of (a) ideal filters and (b) non-ideal filters.

The transmittance function (TF) of an optical filter represents a function of the fraction of input light that the filter transmits with respect to wavelengths. For conventional bandpass filters, the TFs are designed to have an ideal shape, i.e., a sharp brick wall as shown in Figure 4.2 (a). The ideal filters allow the input light to be transmitted only for desired wavelengths, called the passband, and completely stop the remaining wavelengths, called the stopband.

For the filter-based spectrometers, each filter is desired to have an ideal bandpass TF for a passband, and the passbands of the filters do not overlap with each other. Each sample is obtained by a projection of the input signal spectrum for the passband. Then, the raw spectrum is formed by a collection of samples from the filter-array. The raw spectrum can be used as a direct estimate of the signal spectrum. In the ideal filter array, any two spectral components of the input signal spectrum that are more than one passband spacing apart are distinguishable in the raw spectrum.

But, any two spectral components separated by less than one passband cannot be resolved. In order to resolve such spectral components, the passband width of each filter should be decreased and inevitably the number of filters increases to cover the entire bandwidth. Thus, the resolution of the filter-array-based spectrometers with ideal TFs is limited by the number of filters.

However, filters with ideal TFs are not easy to realize in practice, especially in a small size [6, 93]. Therefore, non-ideal TF are inevitable in miniature spectrometers. The shapes of the practical non-ideal TFs employed in a typical filter-array spectrometer are shown in Figure 4.2 (b). These TFs are not purposely designed in such shapes but are instead accidentally obtained in the microlevel processing of implementing the ideal filters. Unlike the ideal TFs, the shapes of non-ideal TFs are smooth, and the passband of each filter overlap with each other. Each sample of the raw spectrum now contains information about the spectral components not only from its own band but also from the neighboring filters' bands, viz. interferences. These interferences cause severe distortion in the raw spectrum. Therefore, for the spectrometers with non-ideal TFs, post-processing of the raw spectrum using DSP algorithms is required.

As a development of modern DSP, the state-of-the-art filter-array based spectrometers are equipped with DSP algorithms not only to alleviate distortions due to unexpected noise or interferences among filters but also accurately reconstruct the original signal spectrum [93, 94].

4.1.2 Incident angle mismatch

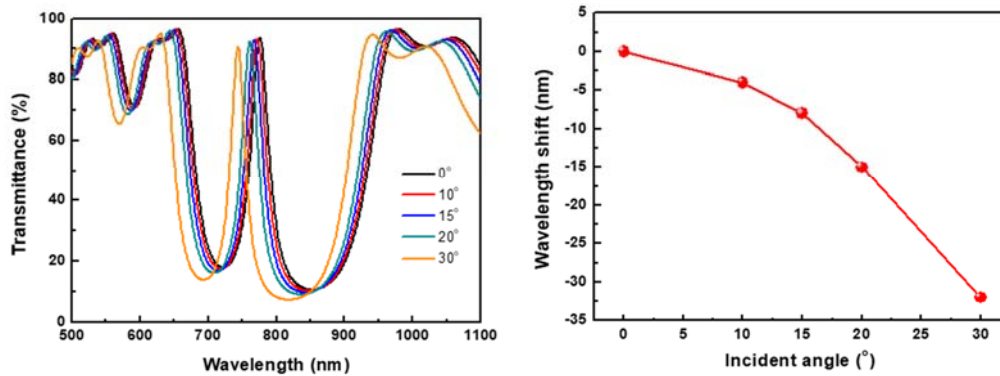


Figure 4.3 TFs with various incident angles, (b) the amount of wavelength-shift with respect to the incident angle.

In the filter-based spectrometers, the incident angle can be varied according to environments and applications. The TFs of filters depend on the incident angle because the optical path difference depends on the incident angle of light. Figure 4.3 (a) shows an example of TFs of a filter with respect to the incident angles where the filter consists of multiple layers of SiO_2 and SiN_x with different thicknesses. As the incident angle increases, the TFs tend to shift from long wavelength to short wavelength. We note that the amount of the wavelength-shift is non-linear as seen in Figure 4.3 (b).

In the proposed compressive spectrometers using DSP, the reconstruction is based on the exact knowledge on the TFs of the filters with respect to the incoming light. If incorrect TFs are used

in the DSP, the reconstructed results will be highly distorted. Thus, it is essential to estimate the incident angle and to use correct TFs in the DSP for accurate spectrum reconstruction.

In the hardware perspective, a collimator can be used [95], which makes the incoming light perpendicular to the filter-array, but in a miniature spectrometer, it is difficult to include a collimator of good performance due to the size and cost. Thus, we propose an incident angle estimation method to solve the mismatch problem between the real TFs and predetermined TFs.

4.1.3 Related works

In [6], we proposed to improve resolution of the spectrometer in the CS framework, where non-ideal TFs in Figure 4.2 (b) were used and high-resolution spectrum reconstruction was achieved than the conventional resolution limit determined by the number of filters. Since then, many researchers have studied implementations of the CS-based spectrometers [95-99]. In the CS-based applications, the sensing of signals and their subsequent recovery is accomplished with a measurement matrix. The measurement matrix is usually designed in the digital domain with coefficients of Fourier, Walsh-Hadamard, or noiselet transform matrix [2]. In [98], a grating-based spectrometer with a DMD and a single pixel detector was proposed, which is similar to the

single pixel camera [2]. A Hadamard matrix is used as the measurement matrix. But, such devices require additional space and cost.

Rather than designing the measurement matrix in the digital domain by DMD or SLM, there has been much interest in designing the inherent analog device that is efficient for the CS-based signal acquisition and reconstruction [7, 95-97, 99]. In [7], we proposed to design optical multilayered filters with *random transmittances* by varying thicknesses of layers of filters. In [96], the random linear projection was realized by liquid crystal. Different spectral responses are obtained by changing the electrical potential over the liquid crystal cell. In [97], different nanophotonic structures such as photonic crystal slabs were proposed. An etalon array reconstructive spectrometer was proposed in [95], where different transmission functions with multiple peaks are obtained by varying the thickness of cavity between two reflectors. Similarly, Fabry-Perot resonator is proposed in [99], where different transmission functions are obtained by controlling the distance between Fabry-Perot mirrors.

4.1.4 Contributions of this chapter

We propose a compressive spectrometer where the holistic spectral information is compressively sampled by optical filters with random transmittance functions and high-resolution

spectral signal is reconstructed from the compressively sampled measurements by the proposed DSP algorithm. Based on the thin-film technology, the optical filter is designed to have random TFs and the filter-array is implemented in two ways: one-by-one fabrication and 2D array fabrication. In the experiments, we demonstrate that the proposed compressive spectrometer can achieve the resolution improvements. In addition, we also propose a method for the incident angle estimation in the compressive spectrometer. We perform a numerical experiment to verify the effectiveness of the proposed method. In our experiment, we demonstrate that the proposed incident angle estimation method can not only estimate the incident angle of incoming light but also reconstruct the spectrum with high resolution.

4.2 System model of filter-based spectrometers

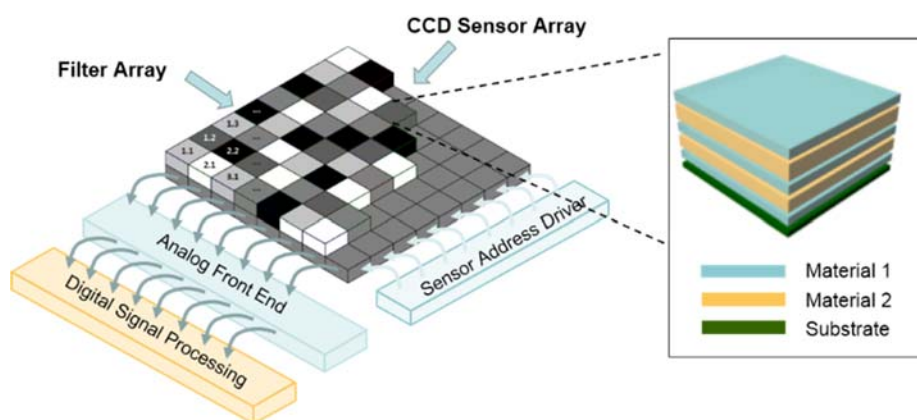


Figure 4.4 Schematic of the filter-array based spectrometer with DSP.

We consider a filter-array-based spectrometer in Figure 4.4. The filter-array consists of M filters each of which is fabricated by depositing multiple layers of dielectric materials on a substrate. According to the refractive indices of the materials and thicknesses of the layers, each filter has a specific TF, which represents the amount of light that the filter allows to be transmitted at a given wavelength λ . Let $f_i(\lambda)$ denotes the TF of i^{th} filter for $i=1,2,\dots,M$. Each filter is attached to one or multiple CCD (or CMOS) elements, and a set of a filter and its corresponding CCD (or CMOS) elements forms a spectral detector. The output of the i^{th} spectral detector is then given by

$$y_i = \int_a^b f_i(\lambda)x(\lambda)d\lambda + n_i, \quad (18)$$

where $x(\lambda)$ is an object signal spectrum and n_i is the observation noise. Then, the output of the spectral detector is sampled in analog-to-digital converter and fed into a DSP unit to estimate the spectrum.

By collecting M samples, the data model for the output measurements, $\mathbf{y} \in \mathbb{R}^{M \times 1}$ can be represented as a system of linear equations:

$$\mathbf{y} = \mathbf{F}\mathbf{x} + \mathbf{n} \quad (19)$$

where \mathbf{x} contains an $N \times 1$ vector of input spectrum sampled at wavelengths $\lambda_1, \lambda_2, \dots, \lambda_N$ and \mathbf{n} is an $M \times 1$ noise vector. Let \mathbf{F} denote an $M \times N$ filter transmission function matrix, which is obtained by uniformly sampling the TFs, $f_i(\lambda)$, at wavelengths $\lambda_1, \lambda_2, \dots, \lambda_N$. Each row of \mathbf{F} represents a sampled TF of a filter.

We note that the number of spectral components of \mathbf{x} is generally greater than the number of filters, i.e., $N > M$. Then, (19) becomes underdetermined and thus has infinite many solutions. If the input spectrum is represented by a sparse signal which contains a small number of non-zero components, the underdetermined system of (19) can be solved uniquely by modern DSP algorithms [11, 14]. For a sparse representation of the input spectrum, we model the input spectrum \mathbf{x} in (19) as a linear combination of basis functions, i.e., $\mathbf{x} = \mathbf{G}\mathbf{s}$ where $\mathbf{s} \in \mathbb{R}^{N \times 1}$ is a K -sparse spectrum with $K \ll N$ non-zero components.

In this work, we choose Gaussian kernels as basis functions since the Gaussian shape can preserve the smooth features of the spectra and requires only two parameters: the central location and width [6, 93]. In Figure 4.5 (a), a Gaussian curve is shown with the central location of 800 nm and the full-width at half-maximum (FWHM) of 40 nm. In Figure 4.5 (b), a smooth spectrum can be expressed as a linear combination of three Gaussian curves with FWHM of 40 nm and central locations of 800, 860 and 900 nm. The kernel matrix $\mathbf{G} \in \mathbb{R}^{N \times N}$ is a set of the Gaussian curves each of which forms a column of \mathbf{G} . According to the nature of TFs of the filter-array and the

nature of the object spectrum for a particular application, the number, locations, and FWHMs of Gaussian curves can be determined. For example, Gaussian curves with large FWHM can be used for broadband signal, Gaussian curves with small FWHM for narrowband signal, or Gaussian curves with a composite of large and small FWHMs for complex signal.

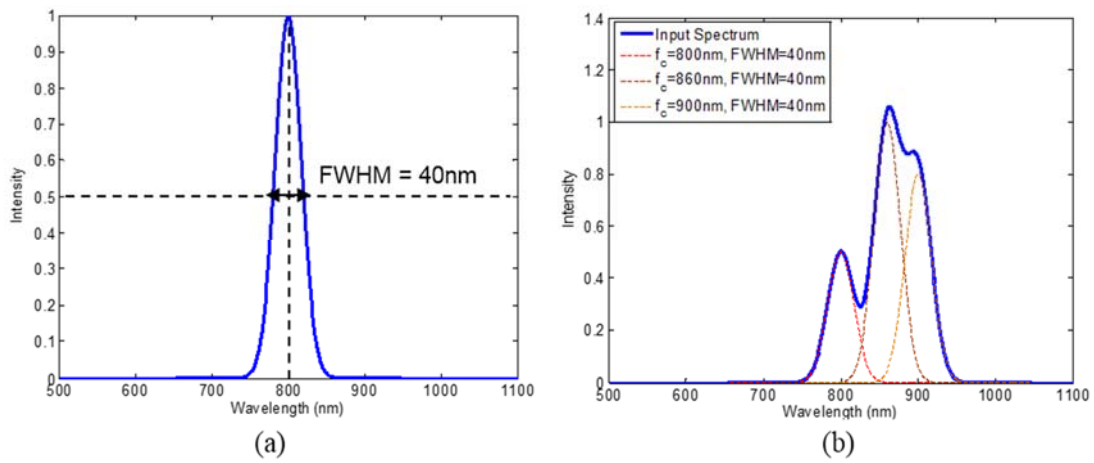


Figure 4.5 (a) A Gaussian kernel with FWHM of 40 nm and center location of 800 nm (b) an example of sparse representation of object spectrum with $K = 3$.

Now, using the sparse representation of the input spectrum, $\mathbf{x} = \mathbf{G}\mathbf{s}$, (19) can be rewritten as

$$\begin{aligned} \mathbf{y} &= \mathbf{F}\mathbf{x} + \mathbf{n} = \mathbf{F}\mathbf{G}\mathbf{s} + \mathbf{n} \\ &= \mathbf{A}\mathbf{s} + \mathbf{n} \end{aligned} \quad (20)$$

where $\mathbf{A} = \mathbf{F}\mathbf{G}$ represents an $M \times N$ matrix. The undetermined linear system of (20) can be solved by l_1 norm minimization. Since the spectrum always has non-negative values, we use l_1 norm minimization algorithm with a non-negative constraint:

$$\hat{\mathbf{s}} = \min_s \|\mathbf{s}\|_1 \quad \text{subject to} \quad \|\mathbf{A}\mathbf{s} - \mathbf{y}\|_2 \leq \varepsilon, \mathbf{s} \geq \mathbf{0} \quad (21)$$

where ε is a small positive constant. From the estimate of the sparse spectrum $\hat{\mathbf{s}}$, the input spectrum can be reconstructed by $\hat{\mathbf{x}} = \mathbf{G}\hat{\mathbf{s}}$. If the input spectrum is reliably reconstructed with $P > M$, the spectrometer can achieve resolution improvements.

4.3 Compressive spectrometers

In this chapter, we propose a compressive spectrometer. For the compressive spectrometer, we first propose a nonnegative l_1 norm minimization (NNLM) algorithm to solve (21). Then, we propose how to design TFs of filter-array for efficient signal acquisition and reconstruction. Last, we explain how to implement the proposed filters.

4.3.1 Nonnegative l_1 norm minimization (NNLM) algorithm

By exploiting the nonnegativity of the spectral signal, the l_1 minimization problem in (21) can be recast as

$$\hat{\mathbf{x}} = \min_x \mathbf{1}^T \mathbf{x} \quad \text{such that} \quad \|\Phi\mathbf{x} - \mathbf{y}\|_2^2 \leq \varepsilon, \mathbf{x} \geq \mathbf{0} \quad (22)$$

In order to solve (22), we employ Primal-Dual Interior Point Method. The Primal-Dual Method is to seek the point (x,s) which satisfies Karush-Kuhn-Tucker (KKT) conditions by root finding method.

The Primal-Dual Interior Point Method Algorithm is to find

$$\text{Minimize } c^T x \text{ subject to } \|Ax-b\|_2^2 \leq \varepsilon, x \geq 0$$

$$A \in \mathbb{R}^{M \times N}, x \in \mathbb{R}^N, b \in \mathbb{R}^M, s \in \mathbb{R}^N$$

Lagrangian function can be defined as below

$$L(x, \lambda, s) := c^T x + \frac{\lambda}{2} \|Ax-b\|_2^2 - s^T x \quad (23)$$

Let x^* be a solution of (2) with the fixed nonnegative lambda λ . Then, the minimizer x^* can be obtained by solving the following differential equations. They are

$$\nabla_{x_\lambda} L_\lambda(x_\lambda, s) = 0 \quad (24)$$

and

$$\nabla_s L_\lambda(x_\lambda, s) = 0. \quad (25)$$

Solving,

$$\begin{aligned}
\|Ax-b\|_2^2 &= (Ax-b)^T (Ax-b) \\
&= \left((Ax)^T - b^T \right) (Ax-b) \\
&= (Ax)^T Ax - (Ax)^T b - b^T Ax + b^T b \\
&= x^T A^T Ax - 2b^T (Ax) + b^T b \\
\frac{\partial}{\partial x} \|Ax-b\|_2^2 &= A^T Ax + A^T Ax - 2A^T b \\
&= 2A^T (Ax-b)
\end{aligned}$$

can be rewritten as

$$\nabla_x L(x, \lambda, s) = c + \lambda A^T (Ax-b) - s$$

It can be interpreted as finding the Karush-Kuhn-Tucker (KKT) conditions of $L_\lambda(x_\lambda, s)$. The

KKT conditions of $L_\lambda(x_\lambda, s)$ are

$$\begin{aligned}
c + \lambda A^T (Ax-b) - s &= 0 \\
\|Ax-b\|_2^2 &\leq \varepsilon, x \geq 0 \\
s^T x &= 0, s \geq 0
\end{aligned}$$

From the KKT conditions, I can define a mapping $F_\lambda(x, s): \mathbb{R}^{2n} \rightarrow \mathbb{R}^{2n}$

$$F_\lambda(x, s) = \begin{bmatrix} \lambda A^T (Ax-b) - s + c \\ XSe \end{bmatrix} = 0, (x, s) \geq 0,$$

where $X = \text{diag}(x_1, x_2, \dots, x_n) \in \mathbb{R}^{N \times N}$, $S = \text{diag}(s_1, s_2, \dots, s_n) \in \mathbb{R}^{N \times N}$, $e = (1, 1, \dots, 1)^T \in \mathbb{R}^N$

Primal-Dual method is seeking $F_\lambda(x, s) = 0$ by Newton's method to find the root of the equation. Newton's method uses the first order approximation of $F_\lambda(x, s)$. Taylor expansion around the point (x_λ, s) gives

$$F_\lambda(x_\lambda + \Delta x_\lambda, s + \Delta s) \approx F_\lambda(x_\lambda, s) + J_\lambda(x_\lambda, s) \begin{bmatrix} \Delta x_\lambda \\ \Delta s \end{bmatrix} \quad (26)$$

where $J_\lambda(x_\lambda, s)$ is the Jacobian of $F_\lambda(x, s)$, and $[\Delta x_\lambda \quad \Delta s]^T$ is the direction vector. By letting

$F_\lambda(x_\lambda + \Delta x_\lambda, s + \Delta s)$ in (26) be zero,

$$J(x_\lambda, s)[\Delta x_\lambda \quad \Delta s]^T = -F_\lambda(x_\lambda, s)$$

where $J(x_\lambda, s) = \begin{bmatrix} \lambda A^T A & -I \\ S & X \end{bmatrix}$

We can obtain the direction vector to solve below equation.

$$\begin{bmatrix} \lambda A^T A & -I \\ S & X \end{bmatrix} \begin{bmatrix} \Delta x_\lambda \\ \Delta s \end{bmatrix} = \begin{bmatrix} -\lambda A^T (Ax_\lambda - b) + s - c \\ -XSe \end{bmatrix}$$

In order to find a step length, I used backtracking search which does not violate $(x, s) \geq 0$

$$step_length = step_length \times step_ratio$$

At the end of each iteration, (x_{k+1}, s_{k+1}) is updated by

$$(x_{k+1}, s_{k+1}) = (x_k, s_k) + \alpha(\Delta x, \Delta s)$$

Table 3. Nonnegative l_1 norm minimization (NNLM) algorithm

-
- Step 1:** Choose $\beta \in (0,1)$ and $\lambda > 0$; Set $k=0$, $\mathbf{s}^{(0)} = \mathbf{1}_N$, $\mathbf{x}^{(0)} = r \times \mathbf{1}_N$, $\alpha > 0$, $\rho > 0$, and $r > 0$, where r is a large integer
- Step 2:** Compute $\Delta \mathbf{x}^{(k)} = \left[\left(\mathbf{X}^{(k)} \right)^{-1} \mathbf{S}^{(k)} + \lambda \mathbf{A}^T \mathbf{A} \right]^{-1} \left[\lambda \mathbf{c}_\lambda^{(k)} - \mathbf{1}_N \right]$ and $\Delta \mathbf{s}^{(k)} = \lambda \left(\mathbf{A}^T \mathbf{A} \Delta \mathbf{x}^{(k)} - \mathbf{c}_\lambda^{(k)} \right) - \mathbf{s}^{(k)} + \mathbf{1}_N$.
- Step 3:** Compute $\alpha_1 = \min_{i \in \{i: \Delta x_i^{(k)} < 0\}} \left| x_i^{(k)} / \Delta x_i^{(k)} \right|$ and $\alpha_2 = \min_{i \in \{i: \Delta s_i^{(k)} < 0\}} \left| s_i^{(k)} / \Delta s_i^{(k)} \right|$.
- Step 4:** Set the step size $\alpha^{(k)}$ to be the first number in the sequence $\alpha_0^{(k)}, \alpha_0^{(k)} \beta, \dots$ that satisfies $\left\| \mathbf{F} \left(\mathbf{x}^{(k)}, \mathbf{s}^{(k)} \right) \right\|_2^2 > \left\| \mathbf{F} \left(\mathbf{x}^{(k)} + \alpha^{(k)} \Delta \mathbf{x}^{(k)}, \mathbf{s}^{(k)} + \alpha^{(k)} \Delta \mathbf{s}^{(k)} \right) \right\|_2^2$ with $\mathbf{x}^{(k)} + \alpha^{(k)} \Delta \mathbf{x}^{(k)} \geq 0$ and $\mathbf{s}^{(k)} + \alpha^{(k)} \Delta \mathbf{s}^{(k)} \geq 0$, where $\alpha_0^{(k)} = 0.99 \times \min(\alpha_1, \alpha_2)$.
- Step 5:** Update both the primal and dual variables as $\mathbf{x}_\lambda^{(k+1)} = \mathbf{x}_\lambda^{(k)} + \alpha^{(k)} \Delta \mathbf{x}_\lambda^{(k)}$ and $\mathbf{s}^{(k+1)} = \mathbf{s}^{(k)} + \alpha^{(k)} \Delta \mathbf{s}^{(k)}$, and set $\lambda = \lambda \rho$
- Step 6:** If the duality gap is small, i.e., $\left| \mathbf{s}^T (-\mathbf{x}) \right| \leq \varepsilon$, then terminate. Otherwise, update $k = k + 1$ and go to Step 2
-

4.3.2 Design of TFs of filter-array

In this work, we aim to present a new approach to further enhance the resolution of the spectrometers by designing TFs. We note that in the filter-based spectrometer, we acquire the spectral data or signal spectrum using spectral filters. That is, the measurement of the signal spectrum is performed via linear projection in (20) by the optical filters. In Chapter 2.3, it is noted that the additional information helps in signal reconstruction in CS. In the filter-based spectrometer, the amount of additional information acquired in each sample of the raw spectrum

is solely proportional to the shape of the TFs. By shaping the TFs through a proposer design procedure, it is possible to extract much information about the input signal spectrum. Therefore, the TF matrix \mathbf{F} in (20) that senses the maximum amount of information about the signal spectrum appears to be the best choice for the spectrometer case, and hence, it is our design goal.

It is well known in CS that measurement matrix \mathbf{F} , the entries of which are drawn from i.i.d. samples of a random variable, exhibit low coherence in (5). We call such matrices as random measurement matrices. These matrices are capable of capturing enough information about the signal s to perform reconstruction from a small number of samples of \mathbf{y} . Therefore, random measurement matrices are widely employed in CS-based applications.

It appears that the goal of designing a measurement matrix in CS resembles that of TF matrix design. That is, both the TF and the measurement matrix should be designed to capture sufficient information to permit the faithful reconstruction of the signal. Since both of these goals are met by random matrices, in this work, we consider a random matrix as the TF matrix rather than using the non-ideal TF matrix as in [100]. Since each row of the TF matrix denotes a transmittance function of a filter, a row of the random TF matrix is termed a random transmittance function. That is, a filter with a transmittance that exhibits random fluctuations as opposed to possessing a pre-designed transmittance shape is termed a *random transmittance function*. Thus, our goal of improving resolution reduces to the design of a set of M filters with random TFs. A set of TFs is

$T_i(\lambda)$ is referred to as random when holistic sampling in the entire range of interest, low correlation among wavelengths, and low coherence among each filter. The filters with random transmittances can be implemented by thin-film technology.

4.3.2.1 *Transmission of multiple layers of thin-film filters*

In this chapter, we first briefly discuss the generic design of thin-film filters to generate band-pass-like transmittances. We then motivate and show how to design random transmissions using the same thin-film structure by varying only the thicknesses of the layers. Let us consider a thin-film filter with m dielectric layers between the input medium (air) and the output medium (substrate).

The transmittance T of a single thin-film layer (a dielectric medium) can be obtained by calculating its reflectance R and its absorption A which obeys the following relations:

$$T + R + A = 1. \quad (27)$$

For a lossless dielectric film, $A = 0$ and hence, $T = 1 - R$. Reflectance of a thin-film layer depends on the polarization of the light. For unpolarized light, the reflectance is the average of the transverse-magnetic (TM) and transverse-electric (TE) polarized waves given by

$$R = \frac{1}{2}(R_{\text{TE}} + R_{\text{TM}}). \quad (28)$$

Then, the transmittance is

$$T = 1 - \frac{1}{2}(R_{\text{TE}} + R_{\text{TM}}). \quad (29)$$

We now aim to calculate the reflectance for both polarization assuming oblique incidence with is occurs in practical cases. Reflectance is the magnitude square of complex reflection coefficient.

If ρ is the reflection coefficient, then $R = \rho\rho^*$. The amplitude reflection coefficient is related to the (oblique) optical admittance N_{medium} of a thin-film layer as the light travels from medium

1 to medium 2, as $\rho = \frac{N_{\text{medium1}} - N_{\text{medium2}}}{N_{\text{medium1}} + N_{\text{medium2}}}$, where

$$N_{\text{medium}} = \begin{cases} n_{\text{medium}} \mathcal{Y} \cos \theta_r & \text{for TE or s-polarization} \\ \frac{n_{\text{medium}} \mathcal{Y}}{\cos \theta_r} & \text{for TM or p-polarization} \end{cases} \quad (30)$$

where $\mathcal{Y} = \sqrt{\frac{\epsilon_0}{\mu_0}} = 2.654 \times 10^{-3} \text{ S}$ is the admittance of free space and θ_r is the angle of refraction of wave from medium 1 to medium 2. The angle of refraction can be calculated using the Snell's law, that is

$$\theta_r = \sin^{-1} \left(\frac{n_i}{n_r} \sin \theta_i \right) \quad (31)$$

When we have multiple-layers, the reflectance and transmittance occur due to the constructive and destructive interference of light. To calculate the reflectance in that case, it is necessary to calculate the admittance of each film. The admittance can be easily calculated via the transfer

matrix analysis. Transfer matrix relates the net electric and magnetic fields at one boundary, say a , with those at the boundary, say b as

$$\begin{bmatrix} E_a \\ B_a \end{bmatrix} = \begin{bmatrix} \cos \delta_1 & \frac{i \sin \delta_1}{N_{\text{medium}1}} \\ iN_{\text{medium}1} \sin \delta_1 & \cos \delta_1 \end{bmatrix} \begin{bmatrix} E_b \\ B_b \end{bmatrix} \quad (32)$$

where the transfer matrix of a single film is

$$M_1 = \begin{bmatrix} \cos \delta_1 & \frac{i \sin \delta_1}{N_{\text{medium}1}} \\ iN_{\text{medium}1} \sin \delta_1 & \cos \delta_1 \end{bmatrix} \quad (33)$$

where δ_1 represents the phase difference between the fields that travel through the film and is given by

$$\delta_1 = \left(\frac{2\pi}{\lambda_0} \right) n_1 d_1 \cos(\theta_{r1}) \quad (34)$$

where n_1 is the refractive index of the film, d_1 is the thickness of the film, λ_0 is the wavelength of light at the incident medium, and θ_{r1} is the angle of refraction at the medium.

The oblique optical admittance of a thin-film layer is then

$$N = \frac{B_a}{E_a} \quad (35)$$

For P numbers of such layers, the net electric and magnetic fields at the boundaries are related as

$$\begin{bmatrix} E_a \\ B_a \end{bmatrix} = M_1 M_2 \cdots M_P \begin{bmatrix} 1 \\ N_{\text{substrate}} \end{bmatrix} = \left\{ \prod_{p=1}^P \begin{bmatrix} \cos \delta_p & \frac{i \sin \delta_p}{N_{\text{medium}p}} \\ iN_{\text{medium}p} \sin \delta_p & \cos \delta_p \end{bmatrix} \right\} \begin{bmatrix} 1 \\ N_{\text{substrate}} \end{bmatrix} \quad (36)$$

The overall transfer matrix, $M_T = M_1 M_2 \cdots M_P$, should be in the order in which the light encounters them with M_1 represents the matrix associated with matrix 1, and so on. The total admittance of P such layers is then given by

$$N_{tot} = \frac{B_a}{E_a} \quad (37)$$

That is, we replace the multilayer assembly with a single layer which presents an admittance of

$$N_{tot}.$$

From the total admittance, the reflectance R of the assembly of thin-film layers is

$$R = \rho\rho^* = \left(\frac{N_{air} - N_{tot}}{N_{air} + N_{tot}} \right) \left(\frac{N_{air} - N_{tot}}{N_{air} + N_{tot}} \right)^* \quad (38)$$

from which the corresponding transmittance can be calculated. We summarize the procedure in

Table 4.

Table 4. Transmittance of multi-layer thin film

1. Number of thin-film layers, excluding the incident air and the final substrate, is P .
2. The transmittance at the output is $T = 1 - \frac{1}{2}(R_{TE} + R_{TM})$, where $R_{TE} = \rho_{TE}\rho_{TE}^*$ and $R_{TM} = \rho_{TM}\rho_{TM}^*$.
3. Now, $\rho = \frac{N_{air} - N_{tot}}{N_{air} + N_{tot}}$, where N_{tot} is the admittance of a layer that represents the layers from 1 to P (excluding the substrate). Thus, we are calculating the transmittance into the substrate and not through the substrate.
4. Starting from the layer on the top of the substrate, layer P , we can calculate the representative admittance as follows:

$$Y_p = \frac{N_{p+1} \cos \delta_p + iN_p \sin \delta_p}{\cos \delta_p + i \left(\frac{N_{p+1}}{N_p} \right) \sin \delta_p} \quad p = 2, \dots, P$$

where $\delta_p = \left(\frac{2\pi}{\lambda_0} \right) n_p d_p \cos(\theta_p)$ and $\theta_p = \sin^{-1} \left(\frac{n_{p-1}}{n_p} \sin \theta_{p-1} \right)$. The admittance of the p^{th} thin-film layer is

$$N_p = \begin{cases} n_p \mathcal{Y} \cos \theta_p & \text{for TE or s-polarization} \\ \frac{n_p \mathcal{Y}}{\cos \theta_p} & \text{for TM or p-polarization} \end{cases}$$

4.3.2.2 Design of the random transmittance

A thin film is a layer of dielectric material with thickness in the micrometer to nanometer range.

Light strike at the surface of a film is either transmitted (transmission film) or reflected (reflection films). We use transmission films in the proposed spectrometer as we use the films as a light filtering device at the front end of the spectrometer. Stacking many film layers creates a multilayer thin-film assembly, which can be designed as filters with desired transmittance characteristics.

The transmittance of the filters depends on the thickness of each layer and the refractive index of

the materials used. In the conventional brick-wall design, the thicknesses of the layers are fixed to quarter-wavelength to create constructive interference and hence the ideal brick-wall filters. In the proposed design, we use arbitrary thickness to generate filters with randomized transmittance patterns. Armed with the thin-film theory, we design filters in various operational mode of light such as TE/TM and oblique/normal incidence of light on the thin-film assembly.

A thin-film optical filter consists of multiple layers of high- and low-refractive index materials (dielectrics) deposited on a substrate [101]. Each layer has thickness usually of one quarter-wavelength for bandpass filtering. Thin-film filters work based on the interference of light transmitted or reflected at the boundaries between the layers. This interference is wavelength-dependent; that is, depending on the number of layers, the index of refraction, and the thicknesses of the layers, the transmission (or reflection) of light through the filter changes with wavelength, and hence the overall transmittance changes. By controlling the thickness of each layer and the number of layers, optical engineers design various filter transmittances such as band-pass filters. In this chapter, we show how varying the thickness of each layer generates random transmittances using the design methodology in [102].

In the framework of spectrum reconstruction in (20), it is important to design a good TF matrix \mathbf{F} for the reconstruction of the sparse spectrum with high accuracy. Designing a good TF matrix \mathbf{F} resembles designing a good measurement matrix in compressed sensing (CS). The mutual

coherence, μ in (5) represents the maximum possible correlation of among pairs of columns of \mathbf{A} . The smaller μ means the smaller the correlation among the columns of \mathbf{A} is. The smaller the correlation is, the better reconstruction accuracy of s from \mathbf{y} . In CS, it is desirable to design the TF matrix \mathbf{F} , such that the matrix $\mathbf{A} = \mathbf{F}\mathbf{G}$ has low coherence.

It is well known in CS that measurement matrices \mathbf{A} , the entries of which are drawn from i.i.d. samples of a random variable, exhibit low coherence. Such matrices are called random measurement matrices. These matrices are capable of capturing enough information about the signal \mathbf{s} to perform reconstruction from a small number of samples of \mathbf{y} . Therefore, random measurement matrices are widely employed in CS-based applications. In [7], random TF filters were introduced in order to enhance the resolution of the spectrometers. In the deposition of the optical thin-film, however, the thickness and the refractive index of each filter are limited in practice, and thus such random TF filters are impractical and non-reproducible due to large tolerance of fabrication. We, thus, propose a realistically implementable design of filters which have a low coherence for resolution improvements.

4.3.3 Implementation of thin-film filters

We propose a design of a thin-film optical filter consisting of multiple layers of high- and low-refractive index materials deposited on a substrate. The transmittance spectra of multilayered dielectric filters were calculated by transfer matrix method [103]. For achieving incoherence among columns of \mathbf{A} , the difference between the high- and low-refractive indices should be high and the number of pairs should be large.

4.3.3.1 *One by one fabrication*

In this work, SiN_x is used for a high-refractive index material and SiO_2 for a low-refractive index material. As shown in Figure 4.6 (a) $M = 64$ filters are considered, each of which is composed of eight pairs of SiN_x and SiO_2 . Note that increasing the number of pairs of layers leads to broadening the range of transmission of the filter. In order to reduce coherence among columns of \mathbf{A} , each filter is designed to have different thicknesses of layers and the concept of the Fabry-Perot filter is applied by changing the order of materials as shown in Figure 4.6 (a). The resultant thicknesses of layers in each filter are given in Table 5. An example of the transmittance spectra designed by the proposed method is shown in Figure 4.6 (b). Filter 4 and filter 36 have the same thicknesses of layers, but the filter 36 is the Fabry-Perot filter of the filter 4. Thus, they have a completely different transmission rate and highly uncorrelated at 700 nm.

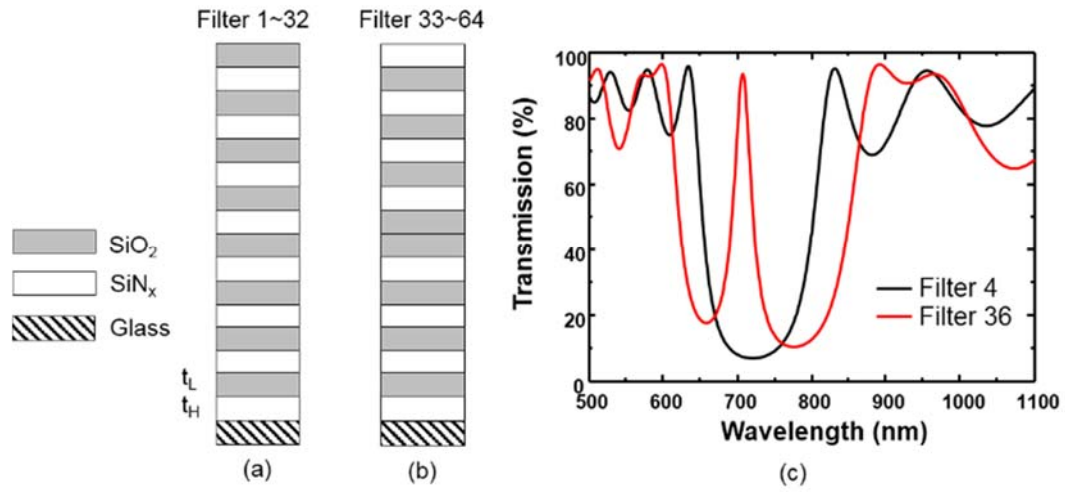


Figure 4.6 (a) Design structures of dielectric filters, (b) transmission spectra of filter 5 and 24.

Table 5. Thicknesses of dielectric filters

Filter index	1, 33	2, 34	3, 35	4, 36	...	32, 64
t _L (mm)	80	90	180	100	...	520
t _H (mm)	80	180	540	100	...	130



Figure 4.7 Implemented a 4 × 16 filter array.

4.3.3.2 2D filter-array fabrication

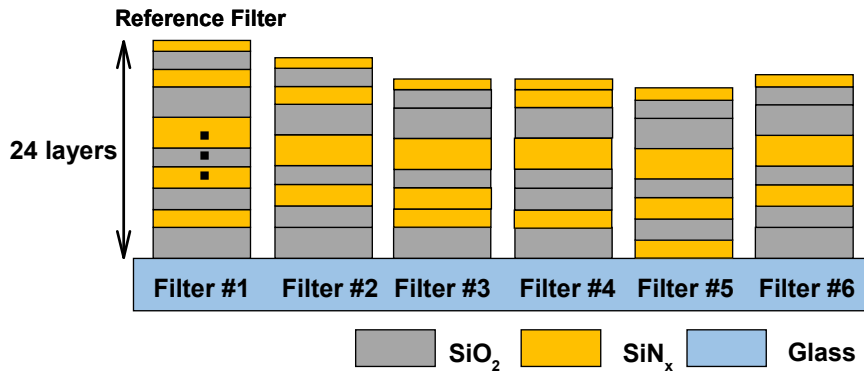


Figure 4.8 Design structures of dielectric filters.

Figure 4.9 shows the process in which a thin-film filter-array is fabricated. This comprises two main parts: one is SiO₂ film deposition and the other is SiN_x film deposition according to the specified thicknesses determined in Chapter 4.3.3. Prior to depositing an SiO₂ film, a 6 x 6 germanium (Ge) grid with elements of size 300 μm and spacing 100 μm was formed on the glass using an e-beam evaporator to separate the filters. Then, selective deposition is done as follows: An intentionally thick SiO₂ film is deposited on the glass patterned with the Ge grid using plasma-enhanced chemical vapor deposition (PECVD). The regions where the film should not be deposited were then removed by conventional photolithography, namely CF₄/O₂ reactive ion etching. The process pressure and radio-frequency power were maintained at 50 mTorr and 50 W,

respectively. The SiN_x film deposition process was performed in the same manner as for SiO_2 . Finally, these two main steps, SiO_2 and SiN_x film deposition, were repeated 12 times each to lay down 24 layers. Figure 4.9 (b) and (c) show a photograph of a fabricated thin-film filter-array and a monochrome image of the filter-array, respectively. Each filter is composed of a different number of layers each with different thicknesses; therefore, each one has unique color due to its different TF, as shown in Figure 4.9 (b).

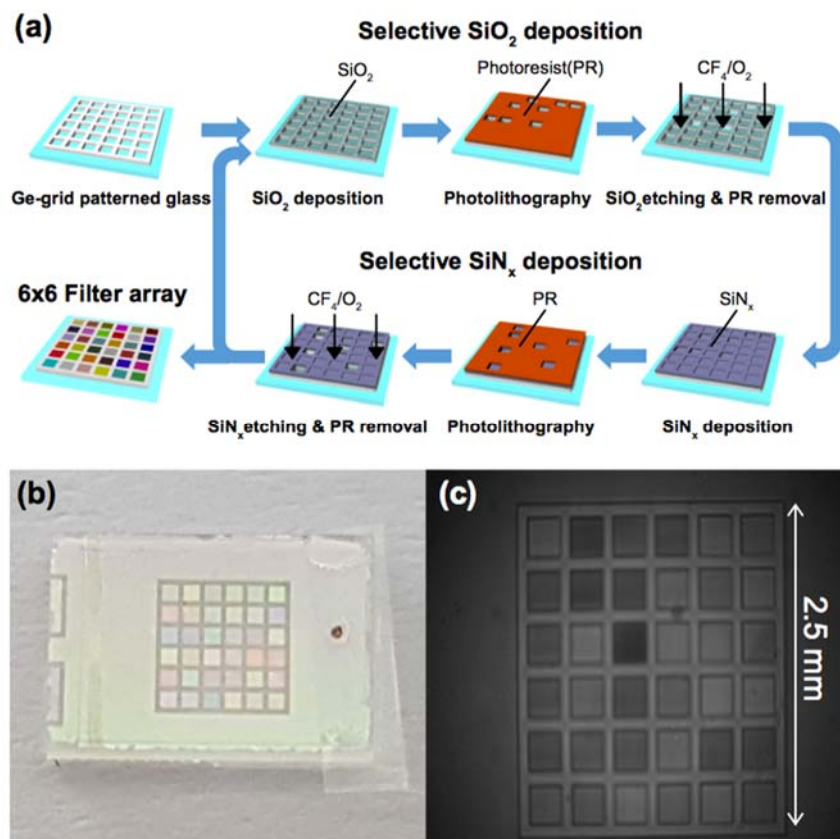


Figure 4.9 (a) Filter-array fabrication procedure, (b) a fabricated thin-film filter-array, (c) Monochrome image of the thin-film filter-array at a wavelength of 700 nm.

4.4 Incident angle estimation of filter-based spectrometers

Estimation algorithm runs with a DSP algorithm that aims to reproduce a high-resolution signal spectrum from the raw spectrum obtained from the spectrometer. The DSP algorithm is performed with previously known measurement matrix \mathbf{F} in (20). In the filter-based spectrometers, \mathbf{F} depends on the incident angle in (34). The incident angle is used to be assumed to be fixed. But, if the incident angle of incoming light does not match the predetermined measurement matrix, it may cause the severe performance degradation. Without DSP, it may occur minor distortions.

4.4.1 System model for incident angle estimation

We consider a spectrometer system with maximum incident angle of θ_{\max} and the range of incident angle is $[0, \theta_{\max}]$. For DSP, we assume that the incident angle can be sampled as a set of discrete angles $\boldsymbol{\theta} = \{\theta_1, \theta_2, \dots, \theta_L\}$ within the range of interest, where L is the number of incident angle elements. In this work, we consider uniform incident angles within the range of interest, i.e., $\Delta\theta = \theta_{\max} / L$.

According to the possible incident angle set $\boldsymbol{\theta}$, a measurement matrix \mathbf{F}_{θ_l} for $l \in \{1, 2, \dots, L\}$ can be obtained from the thin-film theory in Table 4. By concatenating L

measurement matrices, a dictionary matrix $\mathbf{D} \in \mathbb{R}^{M \times (L \cdot N)}$ can be formed as $\mathbf{D} = [\mathbf{F}_{\theta_1} \ \mathbf{F}_{\theta_2} \ \cdots \ \mathbf{F}_{\theta_L}]$.

Then, the linear representation of \mathbf{y} in (19) can be represented as

$$\mathbf{y} = \sum_{i=1}^L \mathbf{F}_{\theta_i} \mathbf{x}_i = \mathbf{D}\mathbf{u}, \quad (39)$$

where $\mathbf{u} = [\mathbf{x}_1^T, \cdots, \mathbf{x}_L^T]^T = [x_{1,1}, \cdots, x_{1,N}, \cdots, x_{L,1}, \cdots, x_{L,N}]^T \in \mathbb{R}^{(L \cdot N) \times 1}$. When incoming light is incident on the filter array with a certain angle in the set $\boldsymbol{\theta}$, a valid observation \mathbf{y} can be sufficiently represented by a linear combination of the columns from the corresponding measurement matrix. For example, when the incident angle of incoming light matches l^{th} measurement matrix, the linear equation becomes

$$\mathbf{y} = \mathbf{D}\mathbf{u}_0 \quad (40)$$

where $\mathbf{u}_0 = [0, \cdots, 0, x_{l,1}, \cdots, x_{l,N}, 0, \cdots, 0]^T$ is a sparse coefficient vector whose entries are zero except for those associated with the l^{th} measurement matrix. The vector, \mathbf{x} can be sparsely represented as $\mathbf{x} = \mathbf{G}\mathbf{s}$. Similarly, \mathbf{u} can be sparsely represented as $\mathbf{u} = \mathbf{B}\mathbf{v}$. Here, \mathbf{v} is an $L \cdot N \times 1$ sparse vector and \mathbf{B} is a block diagonal matrix containing L instances of \mathbf{G} , that is, $\mathbf{B} = \text{diag}(\underbrace{\mathbf{G}, \dots, \mathbf{G}}_L) \in \mathbb{R}^{(L \cdot N) \times (L \cdot N)}$, where $\text{diag}(\cdot)$ represents a diagonal matrix. By using \mathbf{v} , (39)

becomes

$$\mathbf{y} = \mathbf{D}\mathbf{B}\mathbf{v} \quad (41)$$

where $\mathbf{v} = [\mathbf{s}_1^T, \dots, \mathbf{s}_L^T]^T = [s_{1,1}, \dots, s_{1,N}, \dots, s_{L,1}, \dots, s_{L,N}]^T \in \mathbb{R}^{(L \cdot N) \times 1}$. As does (21), l_1 norm

minimization provides a sparse vector $\hat{\mathbf{v}}$:

$$\hat{\mathbf{v}} = \arg \min_{\mathbf{v}} \|\mathbf{v}\|_1 \quad \text{subject to} \quad \|\mathbf{y} - \mathbf{DBv}\| \leq \omega, \quad (42)$$

where ω is a small constant.

4.4.2 Incident angle estimation method

After $\hat{\mathbf{S}}$ has obtained from (42), the problem of estimating the incident angle can be reformulated as a classification problem whose objective is to find the angle at which the incoming light is incident with the highest probability. Because the light spectrum can be sparsely represented in (20) and the measurement matrices are uniquely generated with respect to the incident angles, sparse-representation-based classification (SRC) can be used to estimate the incident angle of incoming light.

We first specify a classification rule by using sparse signal reconstruction. As l_1 norm minimization provides a sparse solution to (42), most of nonzero components in $\hat{\mathbf{S}}$ reside in the class in which the incoming light exists with high probability. Similar to Chapter 3.4.2, we also use the residuals.

$$r_i := \|\mathbf{y} - \mathbf{DB}\delta_i(\hat{\mathbf{v}})\|^2 / \|\delta_i(\hat{\mathbf{v}})\|^2. \quad (43)$$

where $\delta(\hat{\mathbf{v}}) \in \mathbb{R}^{L \times N}$ is obtained by including the elements corresponding to the l^{th} class and nulling all elements of $\hat{\mathbf{v}}$ from other classes. We denote I_e as a set of the indices of estimated distances at which the objects are expected to be located. With r_l for $l=1, \dots, L$, the classification rule is given by

$$I_e = \arg \min_l \{ r_l \} \quad (44)$$

where α is an arbitrary constant. A set of distances $\hat{\theta}$ where the object is expected to be located can be determined by

$$\hat{\theta} = \theta_{I_e} \quad (45)$$

Then, the spectrum that only corresponds to the estimated incident angle is reconstructed by solving $\hat{\mathbf{x}}_{I_e} = \mathbf{G}\hat{\mathbf{s}}_{I_e}$. The SRC-based incident angle estimation is summarized in Table 6.

Table 6 SRC-based incident angle estimation algorithm

Initialization: $\mathbf{y}, \boldsymbol{\theta} = \{\theta_1, \theta_2, \dots, \theta_L\}, \mathbf{G}, \omega, \alpha$

Step 1: Set $\mathbf{D} = [\mathbf{A}_{d_1} \ \mathbf{A}_{d_2} \ \dots \ \mathbf{A}_{d_L}]$ and $\mathbf{B} = \text{diag}(\underbrace{\mathbf{G}, \dots, \mathbf{G}}_L)$.

Step 2: Solve (7) from \mathbf{y} given \mathbf{D} and \mathbf{B} , and obtain $\hat{\mathbf{v}}$.

Step 3: Calculate the regularized residuals:

$$r_l := \|\mathbf{y} - \mathbf{D}\mathbf{B}\delta_l(\hat{\mathbf{v}})\|^2 / \|\delta_l(\hat{\mathbf{v}})\|^2 \text{ for } l=1, \dots, L.$$

Step 4: Obtain the class of existence $I_e = \arg \min_l \{ r_l \}$ and the estimated incident angle of incoming light $\hat{\theta} = \theta_{I_e}$.

4.5 Results and discussions

4.5.1 Measure transmittance functions

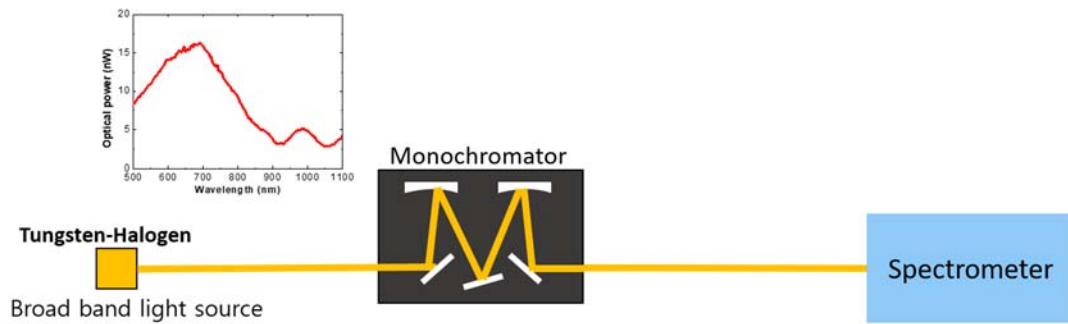


Figure 4.10 Setup for measuring the TFs

The filter-arrays introduced in Chapter 4.3.3, are placed onto a CMOS image camera (E0-1312, Edmund Optics). Because the CMOS array has quantum efficiency which represents the sensitivity with respect to the wavelengths, it is essential to measure the transmittance functions of the spectral detectors (an element consisting of a filter and detector).

For a wavelength of λ , the transmittance function of m^{th} spectral detector is obtained by

$$TF(m, \lambda) = \frac{T_F(m, \lambda) - T_D(m, \lambda)}{T_{NF}(m, \lambda) - T_D(m, \lambda)} \quad (46)$$

where T_F , T_{NF} , and T_D represent transmittances with filter-array, without filter-array, and without source light, respectively. As seen in Figure 4.10, to generate a monochromatic light source that has large intensity only at a specific wavelength, we use a halogen lamp (KLS-150H-LS-150D, Kwangwoo) as a broadband light source and a monochromator (Mmac-200, Mi Optics). The monochromator can transmit the incoming light at a wavelength with FWHM of 1 nm and stop the rest of wavelengths. Then, we perform this procedure repeatedly from 500 to 1000 nm with 1 nm apart. In Figure 4.11, the measured TFs are shown.

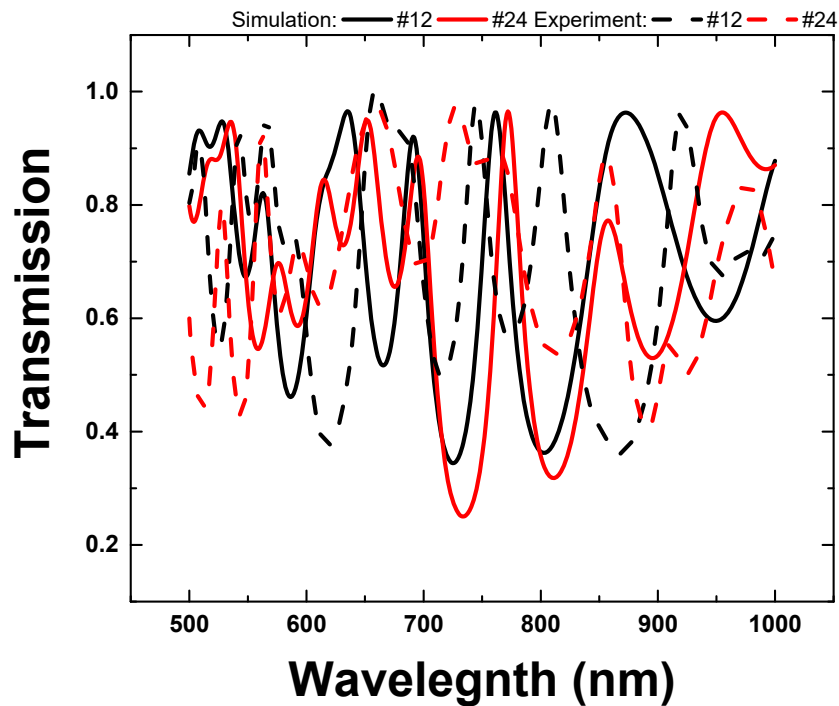


Figure 4.11 Measured transmittance functions.

4.5.2 Results of resolution improvements

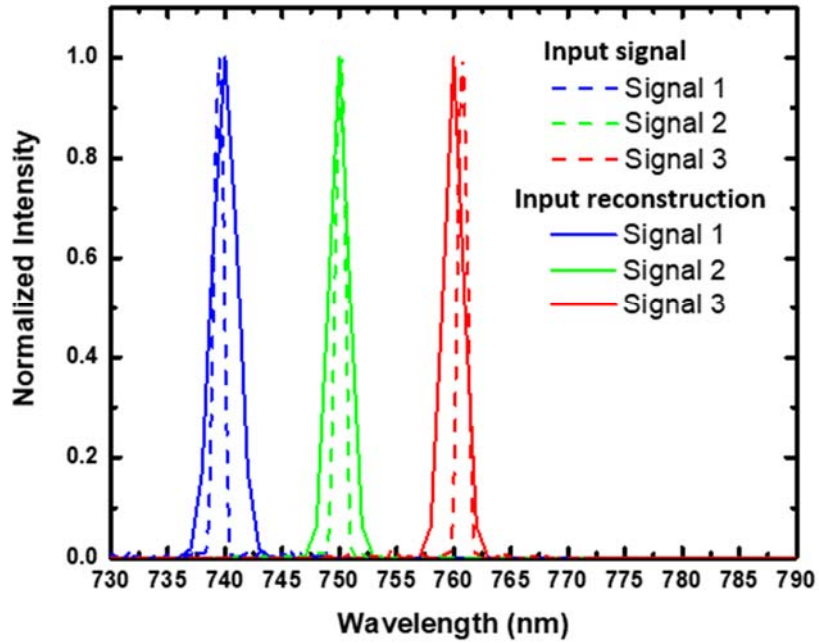


Figure 4.12 Spectral reconstructions of monochromatic light sources.

The experimental results for monochromatic lights are shown in Figure 4.12. In our experiment, we use four different monochromatic spectra, with spectral peaks located at 745, 750, and 900 nm, respectively. The reference spectra are measured using an optical spectrum analyzer (AQ-6315B, Ando) which indicate actual spectral peak locations at 739.5, 750.2, and 760.8 nm, respectively. Using the 2D filter-array compressive spectrometer with the DSP algorithm, the

spectral peak locations are reconstructed at 740, 750, and 760 nm, respectively. The mean FWHM of the reference spectra is approximately 1 nm, and the mean FWHM for the reconstructed spectra is approximately 1.4 nm. Figure 4.13 shows the spectral resolution of green (527 nm) and red (635 nm) LEDs. For reference spectra, we measure the LEDs using a grating spectrometer (QE65000, Ocean Optics). The spectral peak locations for the reference LEDs are 527.6 nm (green LED) and 634.9 nm (red LED), and 633 nm (red LED). The peak signal-to-noise ratios are 28.3 dB (green LED) and 31.7 dB (red LED). The reconstruction results for the proposed compressive spectrometers are similar to those of the grating spectrometer, but the number of modulated signals is significantly small ($M = 36$) and the size of the proposed spectrometer is very small.

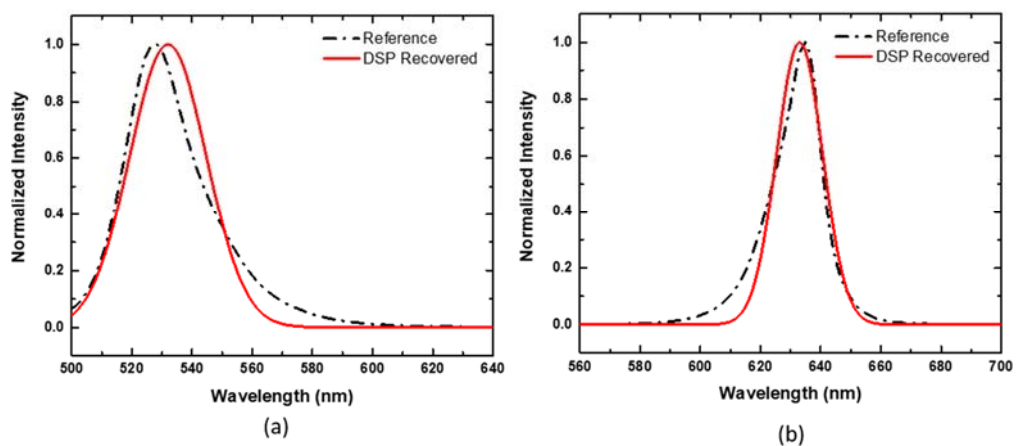


Figure 4.13 Spectral reconstructions of (a) green LED and (b) red LED sources.

4.5.3 Results of incident angle estimation

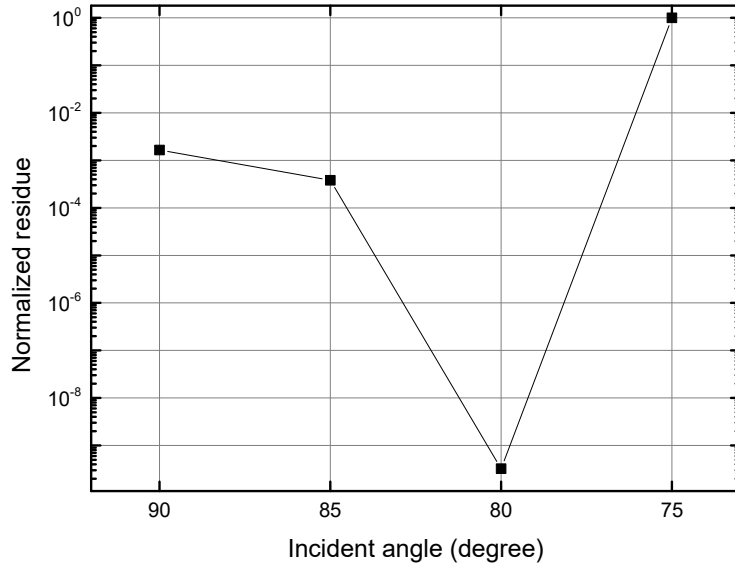


Figure 4.14 Residuals at different incident angles.

We now illustrate the performance of the proposed incident angle estimation via simulation.

We consider a filter array of $M = 64$ in Table 5, each of which consists of 16 layers of alternate SiO_2 and SiN_x with different thicknesses. The range of interest is from 500 nm to 1000 nm with 1 nm step. The TFs of the filters are calculated by Table 4. For the incident angle estimation, we consider 4 possible incident angles of light such as 90° , 85° , 80° , and 75° . Then, the dictionary matrix is formed by $\mathbf{D} = [\mathbf{F}_{90} \ \mathbf{F}_{85} \ \mathbf{F}_{80} \ \mathbf{F}_{75}]$. As an input light source, a synthetic spectrum having

two neighboring peaks at 600 nm and 605 nm is used to evaluate the reconstruction performance.

The Gaussian kernels with FWHM of 2.5 nm are used as a sparsifying basis. When the input light is incident on the filter-array with 80° . The measurements (\mathbf{y}) are acquired by (19).

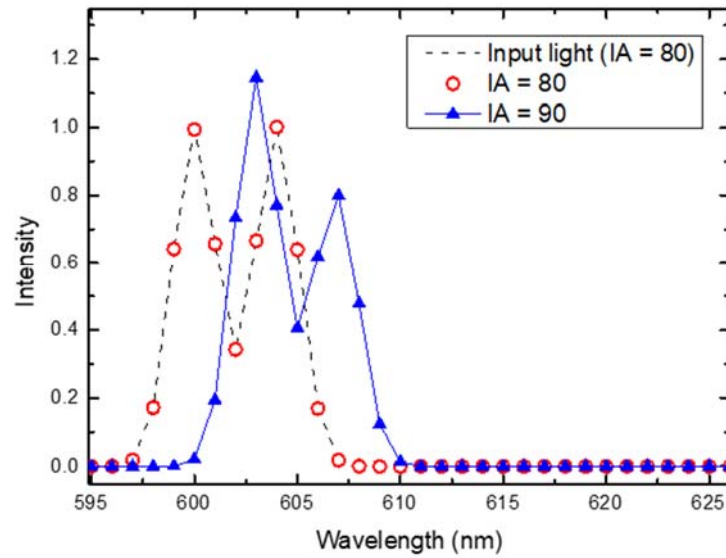


Figure 4.15 Reconstruction performance when (a) incident angle is 10 degree and (b) 30 degree.

Given \mathbf{D} and \mathbf{y} , the incident angle estimation algorithm in Table 6 is performed. The normalized residue with respect to the incident angle is shown in Figure 4.14. The normalized residue has the minimum when the incident angle is matched to the angle of $\theta=80^\circ$. By finding the minimum residue, we can estimate the incident angle as $\hat{\theta}=80^\circ$. From the estimated incident angle $\hat{\theta}$, we can choose the measurement matrix, \mathbf{F}_{80} . Then, DSP recovers the spectrum of input light source

$\hat{\mathbf{x}}$ using the measurement matrix, \mathbf{F}_{80} and the measurement vector \mathbf{y} . The reconstruction results are shown in Figure 4.15. While the resolution limit of 64 filters with the ideal TF is $500/64 = 7.8125$ nm, two neighboring peaks located in 5 nm apart are resolved by the DSP algorithm in Table 3. We note that if incorrect measurement matrix is used in the DSP, then the reconstruction is distorted.

4.6 Summary

We propose the compressive spectrometer by applying the CS framework into the filter-based spectrometer where the number of optical filters is limited. The compressive spectrometer is integrated with the compressive sampler and DSP algorithm. The compressive sampling is realized by the optical filters with random transmittances, which compressively sample the holistic spectral information. The optical filters are designed and implemented based on the thin-film technology. We experimentally show that the proposed compressive spectrometer incorporated with the DSP algorithm is able to improve resolutions. We also propose the incident angle estimation method, which provides a stable reconstruction performance regardless of incident angle mismatch.

The concept of the compressive spectrometer can be applied to the hyperspectral imaging (HSI) that has 2D spatial image with 1D spectrum for each pixel in the image of a scene. In HSI, only spectral sampling can be performed by the proposed filters with random transmittances or the spatial and spectral sampling can be performed sequentially by the integration with COMPU-EYE and compressive spectrometers. The shift of TFs occurs from the incident angle of light or from the temperature [104]. Thus, the proposed incident angle estimation method can be used for calibrations due to the incident angle and the temperature.

In order to find a minute incident angle, a dictionary need to have measurement matrices of finer incident angles. But, this detailed formulation increases the size of the dictionary and inevitably computation time and cost, which is inefficient. To resolve this, as the iterative depth estimation method in Table 2, the incident angle can be iteratively estimated by modifying the proposed incident angle estimation method. For example, the coarse incident angle is estimated first and then fine incident angle is searched around the coarsely estimated incident angle. Otherwise, a joint sparse recovery estimation [105] can be used for the fine estimation of incident angle. To apply the joint sparse recovery method, the measurement matrix mismatch needs to be modelled as a linear expression. For a small range of incident angle variation, the amount of wavelength shift can be regarded as a linear shift. Thus, the joint sparse recovery method can be used in the fine estimation of the incident angle after coarse estimation is performed.

5 CONCLUSIONS

In this dissertation, we have proposed to apply the CS framework to the compound eye imaging system and the miniature spectrometer for resolution improvements. By exploiting the reliable signal reconstruction from the distorted low-dimensional measurements, we focus on resolution improvements rather than compression. For the reliable signal reconstruction in the CS framework, sparse representation of the input signal and incoherence of the measurement matrix should be guaranteed. First, the image and spectrum signals can be sparsely represented by wavelet transforms and Gaussian kernels, respectively. Second, for incoherence of the measurement matrix, we propose to design ommatidia with larger acceptance angles than the interommatidial angle, and filters with random transmittance functions. The ommatidia with large acceptance angles can be implemented by increasing the refractive index of the lens or increasing the size of photodetector. The filters with random TFs can be implemented by multi-layered thin films, implemented by depositing high- and low- refractive indexed dielectric materials, alternatively. The l_1 -norm based DSP algorithms are used to reconstruct the input signal from the low dimensional measurements. As a result, we have achieved significant resolution improvements in both systems. In order to resolve the measurement matrix mismatch due to various object distances in COMPU-EYE and incident angle of the incoming light in compressive spectrometer, we propose depth estimation method in COMPU-EYE and incident angle

estimation method in compressive spectrometers. These mismatch calibration provides more stable signal reconstructions.

BIBLIOGRAPHY

- [1] Y. C. E. G. Kutyniok, Y. C. Eldar and G. Kutyniok, Eds. *Compressed Sensing: Theory and Applications*. Cambridge: Cambridge University Press, 2012.
- [2] M. F. Duarte *et al.*, "Single-pixel imaging via compressive sampling," *IEEE Signal Processing Magazine*, vol. 25, no. 2, pp. 83-91, 2008.
- [3] M. A. Petrovici, C. Damian, C. Udrea, F. Garoi, and D. Coltuc, "Single Pixel Camera with Compressive Sensing by non-uniform sampling," in *2016 International Conference on Communications (COMM)*, 2016, pp. 443-448.
- [4] W.-B. Lee, H. Jang, S. Park, Y. M. Song, and H.-N. Lee, "COMPU-EYE: a high resolution computational compound eye," *Optics Express*, vol. 24, no. 3, pp. 2013-2026, 2016/02/08 2016.
- [5] W.-B. Lee and H.-N. Lee, *Depth-estimation-enabled compound eyes*. 2018, pp. 178-185.
- [6] J. Oliver, W. Lee, S. Park, and H.-N. Lee, "Improving resolution of miniature spectrometers by exploiting sparse nature of signals," *Optics Express*, vol. 20, no. 3, pp. 2613-2625, 2012/01/30 2012.
- [7] J. Oliver, W.-B. Lee, and H.-N. Lee, "Filters with random transmittance for improving resolution in filter-array-based spectrometers," *Optics Express*, vol. 21, no. 4, pp. 3969-3989, 2013/02/25 2013.
- [8] W.-B. Lee, O. James, S.-C. Kim, and H.-N. Lee, "Random optical scatter filters for spectrometers: Implementation and Estimation," in *Imaging and Applied Optics*, Arlington, Virginia, 2013, p. JTU4A.33: Optical Society of America.
- [9] W.-B. Lee, C. Kim, G. W. Ju, Y. T. Lee, and H.-N. Lee, "Design of thin-film filters for resolution improvements in filter-array based spectrometers using DSP," in *SPIE Commercial + Scientific Sensing and Imaging*, 2016, vol. 9855, p. 6: SPIE.
- [10] C. Kim *et al.*, "A method of incident angle estimation for high resolution spectral recovery in filter-array-based spectrometers," in *SPIE OPTO*, 2017, vol. 10117, p. 6: SPIE.
- [11] D. L. Donoho, "Compressed sensing," *IEEE Transactions on Information Theory*, vol. 52, no. 4, pp. 1289-1306, 2006.
- [12] E. J. Candes and T. Tao, "Near-Optimal Signal Recovery From Random Projections: Universal Encoding Strategies?," *IEEE Transactions on Information Theory*, vol. 52, no. 12, pp. 5406-5425, 2006.

- [13] E. J. Candes and M. B. Wakin, "An Introduction To Compressive Sampling," *IEEE Signal Processing Magazine*, vol. 25, no. 2, pp. 21-30, 2008.
- [14] R. G. Baraniuk, "Compressive Sensing," *IEEE Signal Processing Magazine*, vol. 24, no. 4, pp. 118-121, 2007.
- [15] E. J. Candès, Y. C. Eldar, D. Needell, and P. Randall, "Compressed sensing with coherent and redundant dictionaries," *Applied and Computational Harmonic Analysis*, vol. 31, no. 1, pp. 59-73, 2011/07/01/ 2011.
- [16] C. Emmanuel and R. Justin, "Sparsity and incoherence in compressive sampling," *Inverse Problems*, vol. 23, no. 3, p. 969, 2007.
- [17] M. F. Duarte and Y. C. Eldar, "Structured Compressed Sensing: From Theory to Applications," *IEEE Transactions on Signal Processing*, vol. 59, no. 9, pp. 4053-4085, 2011.
- [18] V. Tiwari, P. P. Bansod, and A. Kumar, "Designing sparse sensing matrix for compressive sensing to reconstruct high resolution medical images," *Cogent Engineering*, vol. 2, no. 1, p. 1017244, 2015/12/31 2015.
- [19] D. Takhar *et al.*, "A new compressive imaging camera architecture using optical-domain compression," in *Electronic Imaging 2006*, 2006, vol. 6065, p. 10: SPIE.
- [20] E. Warrant and D.-E. Nilsson, *Invertebrate Vision*. Cambridge University Press, 2006.
- [21] R. Dudley, *The Biomechanics of Insect Flight: Form, Function, Evolution*. 2000.
- [22] D. Floreano, J.-C. Zufferey, M. Srinivasan, and C. Ellington, *Flying Insects and Robots*, 1 ed. Springer-Verlag Berlin Heidelberg, 2010.
- [23] M. F. Land and D.-E. Nilsson, *Animal Eyes*. Oxford University, 2012.
- [24] M. F. Land, "The optics of animal eyes," *Contemporary Physics*, vol. 29, no. 5, pp. 435-455, 1988/09/01 1988.
- [25] D.-E. Nilsson, "Vision Optics and Evolution: Nature's engineering has produced astonishing diversity in eye design," *BioScience*, vol. 39, no. 5, pp. 298-307, 1989.
- [26] A. Borst and J. Plett, "Optical devices: Seeing the world through an insect's eyes," *Nature*, vol. 497, p. 47, 05/01/online 2013.
- [27] Y. M. Song *et al.*, "Digital cameras with designs inspired by the arthropod eye," *Nature*, vol. 497, p. 95, 05/01/online 2013.
- [28] A. Brückner, J. Duparré, A. Bräuer, and A. Tünnermann, "Artificial compound eye applying hyperacuity," *Optics Express*, vol. 14, no. 25, pp. 12076-12084, 2006/12/11 2006.
- [29] D. Jacques, W. Frank, D. Peter, and B. Andreas, "Artificial compound eye zoom camera," *Bioinspiration & Biomimetics*, vol. 3, no. 4, p. 046008, 2008.
- [30] Y. Kitamura *et al.*, "Reconstruction of a high-resolution image on a compound-eye image-capturingsystem," *Applied Optics*, vol. 43, no. 8, pp. 1719-1727, 2004/03/10 2004.

- [31] K.-H. Jeong, J. Kim, and L. P. Lee, "Biologically Inspired Artificial Compound Eyes," *Science*, 10.1126/science.1123053 vol. 312, no. 5773, p. 557, 2006.
- [32] P. Drew Patrick, L. Akhlesh, M.-P. Raúl José, and G. P. Carlo, "Mass fabrication technique for polymeric replicas of arrays of insect corneas," *Bioinspiration & Biomimetics*, vol. 5, no. 3, p. 036001, 2010.
- [33] P. Qu *et al.*, "A simple route to fabricate artificial compound eye structures," *Optics Express*, vol. 20, no. 5, pp. 5775-5782, 2012/02/27 2012.
- [34] L. Li and A. Y. Yi, "Design and fabrication of a freeform microlens array for a compact large-field-of-view compound-eye camera," *Applied Optics*, vol. 51, no. 12, pp. 1843-1852, 2012/04/20 2012.
- [35] R. Hornsey, P. Thomas, W. Wong, S. Pepic, K. Yip, and R. Krishnasamy, "Electronic compound-eye image sensor: construction and calibration," in *Electronic Imaging 2004*, 2004, vol. 5301, p. 12: SPIE.
- [36] H. Zhang *et al.*, "Development of a low cost high precision three-layer 3D artificial compound eye," *Optics Express*, vol. 21, no. 19, pp. 22232-22245, 2013/09/23 2013.
- [37] D. Floreano *et al.*, "Miniature curved artificial compound eyes," *Proceedings of the National Academy of Sciences*, 10.1073/pnas.1219068110 vol. 110, no. 23, p. 9267, 2013.
- [38] T. Someya, *Stretchable Electronics*. Wiley-VCH Verlag GmbH & Co. KGaA, 2013.
- [39] F. Marefat, A. Partovi, and A. Mousavinia, "A hemispherical omni-directional bio inspired optical sensor," in *20th Iranian Conference on Electrical Engineering (ICEE2012)*, 2012, pp. 668-672.
- [40] O. Cogal and Y. Leblebici, "An Insect Eye Inspired Miniaturized Multi-Camera System for Endoscopic Imaging," *IEEE Transactions on Biomedical Circuits and Systems*, vol. 11, no. 1, pp. 212-224, 2017.
- [41] M. F. Land, "VISUAL ACUITY IN INSECTS," *Annual Review of Entomology*, vol. 42, no. 1, pp. 147-177, 1997/01/01 1997.
- [42] H. B. Barlow, "The Size of Ommatidia in Apposition Eyes," *Journal of Experimental Biology*, vol. 29, no. 4, p. 667, 1952.
- [43] K. Kirschfeld, *The Resolution of Lens and Compound Eyes*. 1976, pp. 354-370.
- [44] G. Cristobal, L. Perrinet, and M. Keil, *Biologically Inspired Computer Vision: Fundamentals and Applications*. 2015.
- [45] P. T. Gonzalez-Bellido, T. J. Wardill, and M. Juusola, "Compound eyes and retinal information processing in miniature dipteran species match their specific ecological demands," *Proceedings of the National Academy of Sciences*, 10.1073/pnas.1014438108 vol. 108, no. 10, p. 4224, 2011.

- [46] H. C. Ko *et al.*, "A hemispherical electronic eye camera based on compressible silicon optoelectronics," *Nature*, vol. 454, p. 748, 08/07/online 2008.
- [47] J. Tanida *et al.*, "Thin observation module by bound optics (TOMBO): concept and experimental verification," *Applied Optics*, vol. 40, no. 11, pp. 1806-1813, 2001/04/10 2001.
- [48] E. A. Watson, R. A. Muse, and F. P. Blommel, "Aliasing and blurring in microscanned imagery," in *Aerospace Sensing*, 1992, vol. 1689, p. 9: SPIE.
- [49] H. Jang, C. Yoon, E. Chung, W. Choi, and H.-N. Lee, "Holistic random encoding for imaging through multimode fibers," *Optics Express*, vol. 23, no. 5, pp. 6705-6721, 2015/03/09 2015.
- [50] J. Fang, J. Li, Y. Shen, H. Li, and S. Li, "Super-Resolution Compressed Sensing: An Iterative Reweighted Algorithm for Joint Parameter Learning and Sparse Signal Recovery," *IEEE Signal Processing Letters*, vol. 21, no. 6, pp. 761-765, 2014.
- [51] M. Sarker, "Bioinspired Optical Imaging," in *Biologically Inspired Computer Vision*: Wiley-VCH Verlag GmbH & Co. KGaA, 2015, pp. 109-142.
- [52] M. F. Land, L. Chittka, and R. F. Chapman, "Vision," *Structure and Function*, no. 22, pp. 708-737 Available: <http://ebooks.cambridge.org/ref/id/CBO9781139035460A037>
- [53] *Binocular vision in insects: How mantids solve the correspondence problem*, 1996.
- [54] M. F. Land, "Visual acuity in insects," in *Annual review of entomology. Vol. 42* vol. 42, ed, 1997, pp. 147-177.
- [55] K. Kral, "Behavioural-analytical studies of the role of head movements in depth perception in insects, birds and mammals," in *Behavioural Processes* vol. 64, ed, 2003, pp. 1-12.
- [56] F. van Breugel, K. Morgansen, and M. H. Dickinson, "Monocular distance estimation from optic flow during active landing maneuvers," in *Bioinspir. Biomim.* vol. 9, ed, 2014, pp. 025002-10.
- [57] H. E. Esch and J. E. Burns, "Honeybees Use Optic Flow to Measure the Distance of a Food Source," in *Naturwissenschaften* vol. 82, ed, 1995, pp. 38-40.
- [58] D. Floreano *et al.*, "Miniature curved artificial compound eyes," *Proceedings of the National Academy of Sciences*, vol. 110, no. 23, pp. 9267-9272, June 4 2013.
- [59] Y. M. Song *et al.*, "Digital cameras with designs inspired by the arthropod eye," *Nature*, vol. 497, no. 7447, pp. 95-9, May 2 2013.
- [60] X. Xiao, B. Javidi, M. Martinez-Corral, and A. Stern, "Advances in three-dimensional integral imaging: sensing, display, and applications [Invited]," *Applied Optics*, vol. 52, no. 4, pp. 546-560, 2013/02/01 2013.
- [61] A. Stern and B. Javidi, "Three-Dimensional Image Sensing, Visualization, and Processing Using Integral Imaging," *Proceedings of the IEEE*, vol. 94, no. 3, pp. 591-607, 2006.

- [62] L. Cao and J. Peter, "Iterative reconstruction of projection images from a microlens-based optical detector," *Optics Express*, vol. 19, no. 13, pp. 11932-11943, 2011/06/20 2011.
- [63] K. Kagawa, K. Yamada, E. Tanaka, and J. Tanida, "A three-dimensional multifunctional compound-eye endoscopic system with extended depth of field," in *Electron. Comm. Jpn.* vol. 95, ed, 2012, pp. 14-27.
- [64] *Depth estimation based on adaptive support weight and SIFT for multi-lenslet cameras*, 2012.
- [65] Y. Yuan, X. Wang, X. Wu, J. Zhang, and Y. Zhang, "Improved resolution integral imaging using random aperture coding based on compressive sensing," *Optik - International Journal for Light and Electron Optics*, vol. 130, pp. 413-421, 2017/02/01/ 2017.
- [66] W. B. Lee, H. Jang, S. Park, Y. M. Song, and H. N. Lee, "COMPU-EYE: a high resolution computational compound eye," *Opt Express*, vol. 24, no. 3, pp. 2013-26, Feb 8 2016.
- [67] M. Elad, *Sparse and Redundant Representations - From Theory to Applications in Signal and Image Processing*. 2010.
- [68] E. J. Candes, J. Romberg, and T. Tao, "Robust uncertainty principles: exact signal reconstruction from highly incomplete frequency information," *IEEE Transactions on Information Theory*, vol. 52, no. 2, pp. 489-509, 2006.
- [69] M. Aharon, M. Elad, and A. Bruckstein, "K-SVD: An Algorithm for Designing Overcomplete Dictionaries for Sparse Representation," *IEEE Transactions on Signal Processing*, vol. 54, no. 11, pp. 4311-4322, 2006.
- [70] E. J. Candès, J. K. Romberg, and T. Tao, "Stable signal recovery from incomplete and inaccurate measurements," *Communications on Pure and Applied Mathematics*, vol. 59, no. 8, pp. 1207-1223, 2006.
- [71] D. L. Donoho, M. Elad, and V. N. Temlyakov, "Stable recovery of sparse overcomplete representations in the presence of noise," *IEEE Transactions on Information Theory*, vol. 52, no. 1, pp. 6-18, 2006.
- [72] A. Tavakoli and A. Pourmohammad, "Image Denoising Based on Compressed Sensing," *International Journal of Computer Theory and Engineering*, vol. 4, no. 2, pp. 266-269, 2012.
- [73] A. Beck and M. Teboulle, "A Fast Iterative Shrinkage-Thresholding Algorithm for Linear Inverse Problems," *SIAM Journal on Imaging Sciences*, vol. 2, no. 1, pp. 183-202, 2009.
- [74] A. Chambolle and T. Pock, "A first-order primal-dual algorithm for convex problems with applications to imaging," 2010-06-09, 2010.
- [75] J. Yang and Y. Zhang, "Alternating Direction Algorithms for ℓ_1 -Problems in Compressive Sensing," *SIAM Journal on Scientific Computing*, vol. 33, no. 1, pp. 250-278, 2011.

- [76] W. Wang, M. J. Wainwright, and K. Ramchandran, "Information-Theoretic Limits on Sparse Signal Recovery: Dense versus Sparse Measurement Matrices," *IEEE Transactions on Information Theory*, vol. 56, no. 6, pp. 2967-2979, 2010.
- [77] H. Rauhut, *Compressive sensing and structured random matrices*. 2010.
- [78] K. W. Seo, D.-w. Lee, and B. R. Min, "A 3-D Information Acquisition Algorithm for Close Range Endoscopy," in *World Congress on Medical Physics and Biomedical Engineering 2006: August 27 – September 1, 2006 COEX Seoul, Korea "Imaging the Future Medicine"*, R. Magjarevic and J. H. Nagel, Eds. Berlin, Heidelberg: Springer Berlin Heidelberg, 2007, pp. 2612-2615.
- [79] J. Wright, A. Y. Yang, A. Ganesh, S. S. Sastry, and Y. Ma, "Robust Face Recognition via Sparse Representation," *IEEE Transactions on Pattern Analysis and Machine Intelligence*, vol. 31, no. 2, pp. 210-227, 2009.
- [80] S. Younghak, L. Seungchan, L. Junho, and L. Heung-No, "Sparse representation-based classification scheme for motor imagery-based brain-computer interface systems," *Journal of Neural Engineering*, vol. 9, no. 5, p. 056002, 2012.
- [81] X. Song, Z. Liu, X. Yang, and S. Gao, "A new sparse representation-based classification algorithm using iterative class elimination," *Neural Computing and Applications*, journal article vol. 24, no. 7, pp. 1627-1637, June 01 2014.
- [82] D. L. Donoho, M. Elad, and V. N. Temlyakov, "Stable recovery of sparse overcomplete representations in the presence of noise," in *IEEE Transactions on Information Theory* vol. 52, ed, 2005, pp. 6-18.
- [83] D. Malioutov, M. Cetin, and A. S. Willsky, "A sparse signal reconstruction perspective for source localization with sensor arrays," *IEEE Transactions on Signal Processing*, vol. 53, no. 8, pp. 3010-3022, 2005.
- [84] J. F. Yang and Y. Zhang, "Alternating direction algorithms for l_1 problems in compressive sensing. SIAMJ," ed: Sci. Comput, 2011.
- [85] R. Chartrand, "Fast algorithms for nonconvex compressive sensing: MRI reconstruction from very few data," in *2009 IEEE International Symposium on Biomedical Imaging: From Nano to Macro*, 2009, pp. 262-265.
- [86] S. Boyd, N. Parikh, E. Chu, B. Peleato, and J. Eckstein, "Distributed Optimization and Statistical Learning via the Alternating Direction Method of Multipliers," *Found. Trends Mach. Learn.*, vol. 3, no. 1, pp. 1-122, 2011.
- [87] R. Horisaki, S. Irie, Y. Ogura, and J. Tanida, "Three-Dimensional Information Acquisition Using a Compound Imaging System," *Optical Review*, journal article vol. 14, no. 5, pp. 347-350, September 01 2007.

- [88] H. Ryoichi, K. Keiichiro, N. Yoshizumi, T. Takashi, M. Yasuo, and T. Jun, "Irregular Lens Arrangement Design to Improve Imaging Performance of Compound-Eye Imaging Systems," *Applied Physics Express*, vol. 3, no. 2, p. 022501, 2010.
- [89] Y. Esmaili Salehani, S. Gazor, I.-M. Kim, and S. Yousefi, " ℓ_0 -Norm Sparse Hyperspectral Unmixing Using Arctan Smoothing," *Remote Sensing*, vol. 8, no. 3, p. 187, 2016.
- [90] S.-W. Wang *et al.*, "Concept of a high-resolution miniature spectrometer using an integrated filter array," *Optics Letters*, vol. 32, no. 6, pp. 632-634, 2007/03/15 2007.
- [91] D. J. Brady, *Optical Imaging and Spectroscopy*. John Wiley & Sons, Inc., 2008.
- [92] P. Parrein, A. Landragin-Frassati, and J.-M. Dinten, "Reconstruction Method and Optimal Design of an Interferometric Spectrometer," *Applied Spectroscopy*, vol. 63, no. 7, pp. 786-790, 2009.
- [93] U. Kurokawa, B. I. Choi, and C. C. Chang, "Filter-Based Miniature Spectrometers: Spectrum Reconstruction Using Adaptive Regularization," *IEEE Sensors Journal*, vol. 11, no. 7, pp. 1556-1563, 2011.
- [94] C.-C. Chang, N.-T. Lin, U. Kurokawa, and B. I. Choi, "Spectrum reconstruction for filter-array spectrum sensor from sparse template selection," 2011, vol. 50, p. 8: SPIE.
- [95] E. Huang, Q. Ma, and Z. Liu, "Etalon Array Reconstructive Spectrometry," *Scientific Reports*, Article vol. 7, p. 40693, 01/11/online 2017.
- [96] Y. August and A. Stern, "Compressive sensing spectrometry based on liquid crystal devices," *Optics Letters*, vol. 38, no. 23, pp. 4996-4999, 2013/12/01 2013.
- [97] Z. Wang and Z. Yu, "Spectral analysis based on compressive sensing in nanophotonic structures," *Optics Express*, vol. 22, no. 21, pp. 25608-25614, 2014/10/20 2014.
- [98] D. J. Starling, I. Storer, and G. A. Howland, "Compressive sensing spectroscopy with a single pixel camera," *Applied Optics*, vol. 55, no. 19, pp. 5198-5202, 2016/07/01 2016.
- [99] Y. Oiknine, I. August, D. G. Blumberg, and A. Stern, "Compressive sensing resonator spectroscopy," *Optics Letters*, vol. 42, no. 1, pp. 25-28, 2017/01/01 2017.
- [100] C.-C. Chang and H.-N. Lee, "On the estimation of target spectrum for filter-array based spectrometers," *Optics Express*, vol. 16, no. 2, pp. 1056-1061, 2008/01/21 2008.
- [101] H. A. Macleod, *Thin-Film Optical Filters, Fourth Edition*. CRC Press, 2010.
- [102] J. R. Barry and J. M. Kahn, "Link design for nondirected wireless infrared communications," *Applied Optics*, vol. 34, no. 19, pp. 3764-3776, 1995/07/01 1995.
- [103] F. L. Pedrotti and L. S. Pedrotti, *Introduction to Optics*. Prentice Hall, 1993.
- [104] Available: <https://www.andovercopr.com/technical/bandpass-filter-fundamentals/>

- [105] Z. Tan, P. Yang, and A. Nehorai, "Joint Sparse Recovery Method for Compressed Sensing With Structured Dictionary Mismatches," *IEEE Transactions on Signal Processing*, vol. 62, no. 19, pp. 4997-5008, 2014.